AD-A060 611 ARMY ARMAMENT RESEARCH AND DEVELOPMENT COMMAND ABERD--ETC F/G 19/4
ONE, TWO, AND THREE-DIMENSIONAL IMPACT COMPUTATIONS.(U)
AUG 78 V KUCHER

UNCLASSIFIED ARBRL-TR-02099 SBIE-AD-E430 115 NL

1 OF 1
AD A060611

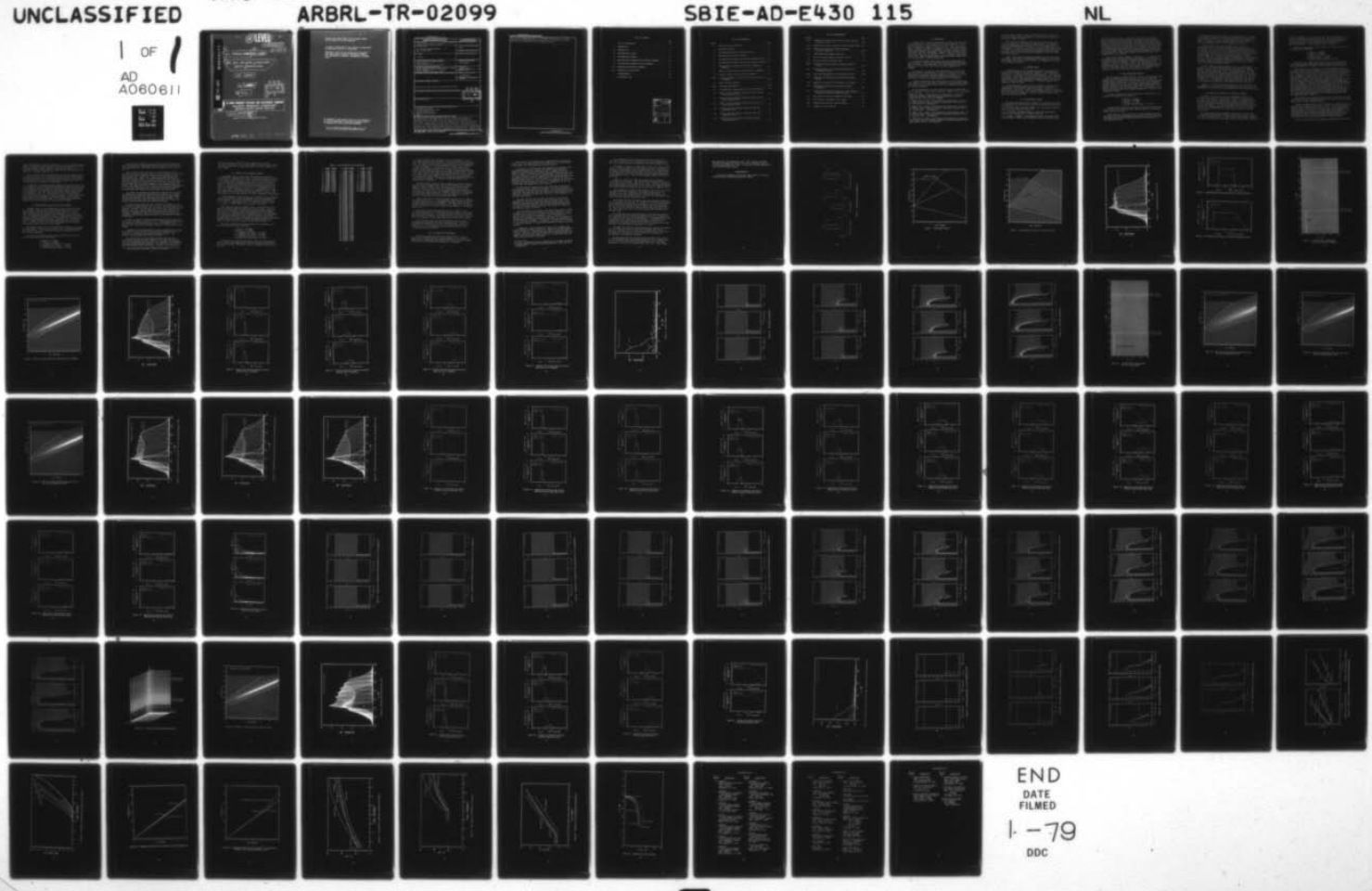

END
DATE FILMED
1-79
DDC

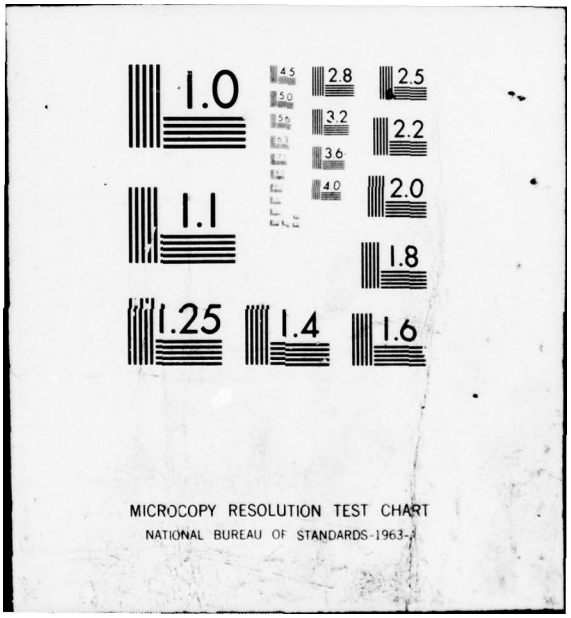
1.0
1.1
1.25
1.4
1.6
1.8
2.0
2.2
2.5
2.8
3.2
3.6
4.0
4.5
5.0
5.6
MICROCOPY RESOLUTION TEST CHART
NATIONAL BUREAU OF STANDARDS-1963-A

AD A060611
DDC FILE COPY

(12) LEVEL II

(19) AD-E430 115

(18) SBIE

(9) Final TECHNICAL REPORT (14) ARBRL-TR-02099

(6)

ONE, TWO, AND THREE-DIMENSIONAL IMPACT COMPUTATIONS.

(10) V. Kucher

(11) Aug 78

(12) 92 p.

DDC
RECEIVED
NOV 1 1978
B

US ARMY ARMAMENT RESEARCH AND DEVELOPMENT COMMAND
BALLISTIC RESEARCH LABORATORY
ABERDEEN PROVING GROUND, MARYLAND

(16) 1L161102AH43

Approved for public release; distribution unlimited.

393 471 78 10 10 040

Destroy this report when it is no longer needed.
Do not return it to the originator.

Secondary distribution of this report by originating or sponsoring activity is prohibited.

Additional copies of this report may be obtained from the National Technical Information Service, U.S. Department of Commerce, Springfield, Virginia 22161.

The findings in this report are not to be construed as an official Department of the Army position, unless so designated by other authorized documents.

The use of trade names or manufacturers' names in this report does not constitute indorsement of any commercial product.

UNCLASSIFIED

SECURITY CLASSIFICATION OF THIS PAGE *(When Data Entered)*

REPORT DOCUMENTATION PAGE		READ INSTRUCTIONS BEFORE COMPLETING FORM
1. REPORT NUMBER TECHNICAL REPORT ARBRL-TR-02099	2. GOVT ACCESSION NO.	3. RECIPIENT'S CATALOG NUMBER
4. TITLE *(and Subtitle)* ONE, TWO, AND THREE-DIMENSIONAL IMPACT COMPUTATIONS		5. TYPE OF REPORT & PERIOD COVERED FINAL 6. PERFORMING ORG. REPORT NUMBER
7. AUTHOR(s) V. Kucher		8. CONTRACT OR GRANT NUMBER(s)
9. PERFORMING ORGANIZATION NAME AND ADDRESS US Army Ballistic Research Laboratory (ATTN: DRDAR-BLT) Aberdeen Proving Ground, MD 21005		10. PROGRAM ELEMENT, PROJECT, TASK AREA & WORK UNIT NUMBERS 1L161102AH43
11. CONTROLLING OFFICE NAME AND ADDRESS US Army Armament Research and Development Command US Army Ballistic Research Laboratory (ATTN: DRDAR-BL) Aberdeen Proving Ground, MD 21005		12. REPORT DATE AUGUST 1978 13. NUMBER OF PAGES 91
14. MONITORING AGENCY NAME & ADDRESS*(if different from Controlling Office)*		15. SECURITY CLASS. *(of this report)* UNCLASSIFIED 15a. DECLASSIFICATION/DOWNGRADING SCHEDULE

16. DISTRIBUTION STATEMENT *(of this Report)*

Approved for public release; distribution unlimited.

17. DISTRIBUTION STATEMENT *(of the abstract entered in Block 20, if different from Report)*

DDC
RECEIVED
NOV 1 1978
B

18. SUPPLEMENTARY NOTES

19. KEY WORDS *(Continue on reverse side if necessary and identify by block number)*

Penetration mechanics
Two-dimensional computer code
Eulerian computer code
Shaped-charge penetration
Impact

20. ABSTRACT *(Continue on reverse side if necessary and identify by block number)*

A one-dimensional impact problem was run on a computer to determine the characteristics of the DORF-9 code. This code, in a two-dimensional, axisymmetric mode, was used to study the penetration of a 25.5-mm steel plate by a copper, shaped-charge jet, which was simulated by a 6-mm, semi-infinite, copper rod impacting normally on the plate at 7.5 km/s. This problem was also simulated by a plate-on-plate impact with the code operating in a two-dimensional, Cartesian mode. The thickness of the penetrator plate was varied. Penetration, hole growth and shape, shock-wave propagation, and spallation were compared →

next page

DD FORM 1 JAN 73 1473 EDITION OF 1 NOV 65 IS OBSOLETE

UNCLASSIFIED

SECURITY CLASSIFICATION OF THIS PAGE *(When Data Entered)*

for the rod and penetrator plates. The TRIDORF code was used in a three-dimensional, Cartesian mode to run a problem of a bar impacting on a plate. Comparisons were made between the rod and bar impacts.

TABLE OF CONTENTS

		Page
	LIST OF ILLUSTRATIONS	5
I.	INTRODUCTION	7
II.	COMPUTER CODE	8
III.	ONE-DIMENSIONAL THEORY	8
IV.	ONE-DIMENSIONAL PROBLEM	9
V.	TWO-DIMENSIONAL PROBLEM WITH CYLINDRICAL GEOMETRY	10
VI.	TWO-DIMENSIONAL PROBLEM WITH SLAB GEOMETRY	12
VII.	PROBLEM WITH RECTANGULAR GEOMETRY	14
VIII.	DISCUSSION AND CONCLUSIONS	16
	ACKNOWLEDGMENTS	19
	DISTRIBUTION LIST	89

ACCESSION for
NTIS White Section
DDC Buff Section
UNANNOUNCED
JUSTIFICATION
BY
DISTRIBUTION/AVAILABILITY CODES
Dist. Avail. and/or SPECIAL
A

78 10 10 040

LIST OF ILLUSTRATIONS

Figure		Page
1.	Penetrator-Target Geometries	20
2.	Shock-Wave Diagram	21
3.	One-Dimensional Motion of Tracer Particles	22
4.	One-Dimensional Pressure Profiles.	23
5.	One-Dimensional Pressure and Particle Velocity Profiles.	24
6.	One-Dimensional Pressure and Particle Velocity Profiles.	24
7.	Two-Dimensional Computational Grid for Cylindrical Geometry.	25
8.	Motion of Tracer Particles along the Axis of Symmetry.	26
9.	Pressure Profiles along the Axis of Symmetry	27
10-13.	Pressure and Particle Velocity Profiles along the Axis of Symmetry	28-31
14.	Radial Pressure Profiles	32
15-18.	Rod-Target Deformation	33-36
19.	Two-Dimensional Computational Grid for Slab Geometry	37
20.	Motion of Tracer Particles along the Y-Axis for the 6-mm Penetrator Plate	38
21.	Motion of Tracer Particles along the Y-Axis for the 4-mm Penetrator Plate	39
22.	Motion of Tracer Particles along the Y-Axis for the 3-mm Penetrator Plate	40
23.	Pressure Profiles along the Y-Axis for the 6-mm Penetrator Plate.	41
24.	Pressure Profiles along the Y-Axis for the 4-mm Penetrator Plate.	42
25.	Pressure Profiles along the Y-Axis for the 3-mm Penetrator Plate.	43

LIST OF ILLUSTRATIONS

Figure		Page
26-37.	Comparison of Pressure and Particle Velocity Profiles along the Y-Axis.	44-55
38.	Comparison of Pressure Profiles in the 15.25-mm Y-Plane.	56
39-50.	Comparison of Penetrator-Target Deformation for Slab Geometries	57-68
51.	Three-Dimensional Computational Grid	69
52.	Motion of Tracer Particles along the Y-Axis.	70
53.	Pressure Profiles along the Y-Axis	71
54-57.	Pressure and Particle Velocity Profiles along the Y-Axis.	72-75
58.	Pressure Profiles in the 15.25-mm Y-Plane and the Z-Coordinate Plane.	76
59-62.	Bar-Target Deformation in the Z-Coordinate Plane	77-80
63.	Comparison of Transmitted and Reflected Shock-Wave Motion.	81
64.	Comparison of the Motion of the Back of the Target	82
65.	Penetration Histories for Cylindrical and Slab Geometries.	83
66.	Penetration Histories for Cylindrical and Rectangular Geometries and the One-Dimensional Case	84
67.	Hole Growth at the Front Surface of the Target	85
68.	Hole Growth at the Middle of the Target.	86
69.	Comparison of Transverse Pressure Motion	87
70.	Comparison of Hole Profiles.	88

I. INTRODUCTION

Two-dimensional, Eulerian, hydrodynamic, computer codes have been used for many years to solve hypervelocity impact problems. To deal with the problem of a normal impact of a rod on a plate, these codes employ cylindrically symmetric coordinates (r,z). Since more and more impact problems of interest are asymmetric in nature (such as oblique impacts) and computers have become faster and larger in memory, three-dimensional, Eulerian, hydrodynamic, computer codes have been pressed into service over the past few years.[1,2,3,4,5] Compared to two-dimensional codes, these three-dimensional codes require more computational cells and, therefore, longer running times.

As a means of reducing the running time for a three-dimensional impact problem or because a three-dimensional hydrodynamic code might not be available, a two-dimensional (x,y) simulation of the problem is employed. In this study, the validity of these computations is examined.

The problem to be studied is the penetration of a 25.5-mm steel plate by a copper, shaped-charge jet, which is simulated by a 6-mm, semi-infinite, copper rod impacting normally on the plate at 7.5 km/s. Penetration, hole growth and shape, shock-wave propagation, and spallation are some of the impact phenomena that are examined.

In order to determine some characteristics of the two-dimensional code, which is used in this study, a problem of a semi-infinite, copper mass impacting on an infinite steel plate (a one-dimensional problem) was run on the computer.

The one-dimensional case was followed by several two-dimensional cases. The first of these used cylindrically symmetric (r,z) coordinates

---

[1] *Wallace E. Johnson, "Three-Dimensional Computations on Penetrator-Target Interactions," Ballistic Research Laboratory Contractor Report No. 338, April 1977. (AD #A041058)*

[2] *W. Johnson and V. Kucher, "Three-Dimensional Computations, Volume I: 30° Oblique Impact," Ballistic Research Laboratory Contractor Report No. 344, July 1977. (AD #A043295)*

[3] *W. Johnson and V. Kucher, "Three-Dimensional Computations, Volume II: 45° Oblique Impact," Ballistic Research Laboratory Contractor Report No. 354, Nov 1977.* (AD #A051296)

[4] *W. Johnson and V. Kucher, "Three-Dimensional Computations, Volume III: 60° Oblique Impact," Ballistic Research Laboratory Contractor Report No. 355, Dec 1977.* (AD #A051350)

[5] *W. Johnson and V. Kucher, "Three-Dimensional Computations, Volume IV: 77.5° Oblique Impact," Ballistic Research Laboratory Contractor Report ARBRL-CR-356, Dec 1977.* (AD #A051092)

to provide what we shall call the true finite-difference solution to the impact problem under consideration. The cylindrical geometry for this case is shown in Figure 1.

Three other two-dimensional cases were run; however, in these cases, a Cartesian (x,y) coordinate system was used. In these cases the impact problem was simulated by a semi-infinite copper plate impacting the target plate. See Figure 1 for a pictorial view of the slab geometry. In these cases, there is no material flow normal to the x,y plane. In each case a different copper plate thickness was used, and the results of the computations were compared to the true finite-difference solution.

Figure 1 also shows the rectangular geometry for the final case, that being a semi-infinite, square, copper bar impacting on an infinite steel plate. The results of this run were also compared to the true finite-difference solution.

II. COMPUTER CODES

The DORF-9 code[6] was used to generate data for the one and two-dimensional treatments of the problem. DORF-9 is a two-dimensional, multimaterial, continuous, Eulerian, hydrodynamic code. An option of Cartesian (x,y) coordinates or cylindrically symmetric (r,z) coordinates is provided. Also, tracer particles, which play a passive role in the computations, can be used to provide a Lagrangian look to the plotted output of penetrator-target deformation. Tillotson's form of the equation of state was used.[7]

A three-dimensional solution to the problem was obtained by the TRIDORF code[8] with Tillotson's equation of state. It also is a multimaterial, continuous, Eulerian, hydrodynamic code with an option for using tracer particles. This code uses Cartesian (x,y,z) coordinates. Both codes were run on BRLESC-2, a digital computer located at the Ballistic Research Laboratory.

III. ONE-DIMENSIONAL THEORY

The shock wave diagram shown in Figure 2 was constructed by using one-dimensional shock-wave theory coupled with Tillotson's equations of

---

[6] *W. E. Johnson, "Code Correlation Study," Air Force Weapons Laboratory Report No. AFWL-TR-70-144, April 1971.*

[7] *J. H. Tillotson, "Metallic Equations of State for Hypervelocity Impact," Gulf General Atomic, GA-3216, July 1962.*

[8] *W. E. Johnson, "TRIDORF - A Two-Material Version of the TRIOIL Code with Strength," Computer Code Consultants, CCC-976, September 1976.*

state[7] for copper and iron. Initially the interface of the copper projectile and the steel target plate is located at 15.0 mm with the target extending from 15.0 to 40.5 mm. The motion of the semi-infinite projectile is in the positive direction at 7.5 km/s. Upon impact (t=0), a transmitted shock wave, U, propagates into the target at 9.76 km/s until it reaches the back of the target where it is reflected into the target as a centered rarefaction wave, with a leading edge, R, traveling at a speed of 5.07 km/s. When the leading edge passes through the interface, I, the sound speed of the copper changes the speed of the wave, now designated as S, to 4.88 km/s.

Also, at the instant of impact, a shock wave, V, is reflected into the projectile at 1.93 km/s without any disturbance to the wave over the time period of the diagram. The material between U and V moves with a particle velocity of 3.92 km/s. This is also the speed of the interface, I, until its encounter with R. The interface motion was not calculated past this point. The shock pressure of the material between U and V is 3.01 Mbar. The back of the target is accelerated by the reflection of U to 7.84 km/s (twice the particle velocity).

IV. ONE-DIMENSIONAL PROBLEM

The two-dimensional DORF-9 code was used in a one-dimensional mode in order to establish some characteristics of the code. Uniform computational cell widths of 0.5 mm were setup over a distance of 50 mm. The steel target extended from 15.0 to 40.5 mm; the copper penetrator extended from 0.0 to 15.0 mm. To simulate a semi-infinite penetrator, boundary conditions were specified to feed penetrator material, in the positive direction, into the computational cells. The boundary at the 50-mm position was transmittive, permitting material to flow out of the computational region.

The cells, occupying the initial position of the penetrator, were given the following initial conditions:

1. Density = 8.9 Mg/m^3.
2. Pressure = 0.0 Mbar.
3. Velocity = 7.5 km/s.
4. Specific internal energy = 0.0 J/g.

The same initial conditions were given to the cells occupying the initial position of the target except that the density was 7.86 Mg/m^3 and the velocity was zero.

Tracer particles were positioned at 0.5-mm increments along the penetrator and target; furthermore, tracer particles were fed into the computational cells with the penetrator material being supplied into the computational grid.

The motion of the tracer particles is shown in Figure 3. A change in the direction of the tracer particle path indicates the location of a shock wave or rarefaction. By transferring the shock diagram in Figure 2 to Figure 3, a good agreement between the exact solution and the finite-difference solution to the problem is indicated.

Pressure profiles are shown in Figure 4 for the first 17 computational cycles. Since the pressures are plotted at the centers of each cell, the initial rise of the pressure can be observed at y = 15.25 mm. In 7 cycles (0.16 μs) the pressure peaks after overshooting the theoretical shock pressure of 3.01 Mbar; then, the transmitted and reflected shock fronts can be seen to move away from the initial point of impact (y = 15.0 mm) as indicated previously in Figure 3. By cycle 17 (0.30 μs) the pressure plateau is established in the neighborhood of 3 Mbar. Note that instead of the theoretical pressure step wave, each of the shock-wave fronts is smeared over 4 or 5 cells. This is typical of Eulerian hydrodynamic codes.

Figure 5 shows the pressure profile at 1.5 μs. The pressure plateau is at 3.01 Mbar with overshoots at each end of the plateau. The particle velocity in the region of the pressure plateau is 3.92 km/s, agreeing with the theoretical value. The triangular symbol at 21 mm indicates the position of the penetrator-target interface. The general shape of the pressure and velocity profiles remains the same until the forward moving shock wave reaches the back of the target (y = 40.5 mm) at about 2.6 μs. The rarefaction wave, moving back into the target, is shown at 4.0 μs in Figure 6. Note that the material near the back of the target was accelerated by the reflection of the shock wave.

Figures 2 - 6 show some of the characteristics of an Eulerian code. The agreement of the one-dimensional computations with theory gives us confidence in the code when it is applied to this class of impact problems.

V. TWO-DIMENSIONAL PROBLEM WITH CYLINDRICAL GEOMETRY

The DORF-9 code was used to solve the following problem: The penetration of an infinite steel plate, 25.5-mm thick, impacted upon by a 6-mm, semi-infinite, copper rod at 7.5 km/s. A computational grid was laid out to cover the cross-sectional region of interest of the rod-target configuration with the rod's centerline coinciding with the z-axis. See Figure 7. The overall dimensions of the grid was 25 mm by 50 mm with a corresponding grid size of 50 by 100 cells. A uniform grid was used with each toroidal computational cell having a 0.5-mm cross section.

The target was initially bounded by the planes z = 15.0 mm and z = 40.5 mm, the former being the front surface of the target. The rod was initially bounded by the z = 0 and 15.0 mm planes and the cylinder, r = 3 mm. Since the rod's initial motion was in the positive z-direction,

the bottom boundary of the grid was specified to feed rod material into grid as a simulation of a semi-infinite rod. The right boundary of the grid was selected to be transmittive thus allowing the simulation of an infinite plate. The top boundary was also transmittive, permitting material to flow out of the region of interest.

The cells, occupying the initial volume of the rod, were given the following initial conditions:

1. Density = 8.9 Mg/m^3.
2. Pressure = 0.0 Mbar.
3. Radial velocity = 0.0 km/s.
4. Axial velocity = 7.5 km/s.
5. Specific internal energy = 0.0 J/g.

Similar initial conditions were given to the cells occupying the initial volume of the target except that the density was that of the steel target material, 7.86 Mg/m^3 , and the axial velocity was zero.

Tracer particles were positioned at 0.5-mm increments in the rod and target along the axis of symmetry. Also, tracer particles were fed into the grid with the rod material being supplied into the computational grid. Figure 8 shows the motion of these tracer particles along the axis of symmetry. A change in the direction of the tracer particle paths indicates the location of a shock wave. A transmitted wave and reflected wave emanate from the point of impact (z = 15.0 mm). Initially both of these waves have the speeds determined in the one-dimensional case. See Figure 3. However, after about 0.34 μs, the rarefaction wave from the cylindrical free suface of the rod reaches the axis of the rod and relieves the pressure in the shock wave moving into the rod. The reflected shock wave never traveled more than 2 mm from the point of impact before turning and traveling in the same direction as the rod. Note that the tracer particle on the back surface of the target moves at a lower speed after encountering the transmitted shock wave than one-dimensional theory suggests.

The pressure of the transmitted shock wave is relieved by the front surface of the target, thereby causing the wave to move at a lower speed than predicted by one-dimensional theory.

Pressure profiles along the axis of symmetry are shown in Figure 9 for the first 23 computational cycles (0.4 μs). Since the pressures are plotted at the centers of each cell, the initial rise in pressure is located around z = 15.25 mm. In 8 cycles (0.09 μs) the pressure peaks after overshooting the theoretical shock pressure of 3.01-Mbar. Thereafter, the transmitted and reflected shock fronts form and move away from each other. Unlike the constant pressure profile of the one-dimensional case, the pressure plateau in Figure 9 decays.

Pressure and particle velocity profiles along the axis of the rod-

target configuration are shown in Figures 10 - 13. The triangular symbol denotes the location of the interface on the axis of symmetry. The peak pressure of about 0.7 Mbar, shown at 2.0 μs, persists until it is affected by the pressure release wave coming off the back surface of the target (z = 40.5 mm) at about 4.2 μs.

Figure 14 shows radial pressure profiles at 0.5 μs intervals in the 15.25-mm z-plane, which is 0.25 mm from the front surface of the target. The radial pressure in the rod, having a radius of 3 mm, can be observed to be decreasing with time. Also, the radial propagation and decay of the shock wave in the target are illustrated.

In addition to the tracer particles which were positioned along the axis of symmetry, tracer particles were positioned along the free surfaces of the target and the rod. When the coordinates of these tracer particles are line-plotted, the deformation of the rod and target can be pictured as in Figures 15 - 18. Note that the back surface of the target starts to bulge between 4 and 5 μs. Tracer particles were also positioned within the rod and the target as shown in Figure 15. The tracer particles in the copper rod are depicted by triangular symbols; square symbols depict particles in the steel target. As time progresses, these tracer particles show the flow patterns in the rod and the target.

VI. TWO-DIMENSIONAL PROBLEMS WITH SLAB GEOMETRY

The DORF-9 code, in a two-dimensional x,y-mode, was used to solve the following: The penetration of an infinite steel plate, 25.5-mm thick, impacted upon by a semi-infinite, copper plate at 7.5 km/s. Three thicknesses of the penetrator were considered: 6 mm, 4 mm, and 3 mm. The computational grid was laid out to cover the cross-sectional region of interest of the penetrator-target configuration with the plane of symmetry passing through the y-axis. See Figure 19. The overall grid was 25 mm by 50 mm with the corresponding grid size of 50 by 100 cells. A uniform grid was used with each computational cell having a 0.5-mm square cross section and a unit length.

The boundary conditions for the grid and the location of the target were the same as in the cylindrical geometry case. The semi-thicknesses of the penetrators, 3 mm, 2 mm, and 1.5 mm, were represented by 6, 4, and 3 cells, respectively.

The cells, occupying the initial volume of the penetrator, were given the following initial conditions:

1. Density = 8.9 Mg/m^3.
2. Pressure = 0.0 Mbar.
3. X-component of velocity = 0.0 km/s.
4. Y-component of velocity = 7.5 km/s.
5. Specific internal energy = 0.0 J/g.

Similar initial conditions were given to the cells occupying the initial volume of the target except that the density was that of the steel target material, 7.86 Mg/m^3, and the y-component of the velocity was zero.

Tracer particles were positioned at 0.5-mm increments in the penetrator and target along the y-axis. Also, tracer particles were fed into the grid with the penetrator material being supplied into the computational grid. Figures 20 - 22 show the motion of these tracer particles along the y-axis. A transmitted shock wave and reflected shock wave, located by the change in the direction of the tracer particle paths, emanate from the point of impact (y = 15.0 mm). Initially both of these waves have the speeds determined in the one-dimensional case. However, after about 0.34, 0.23, or 0.17 μs for penetrator thicknesses of 6, 4, and 3 mm, respectively, the rarefaction wave from the sides of the penetrator plate reaches the center plane of the penetrator.

The effects of decreasing the penetrator thickness are to decrease the speed of the transmitted shock wave and to decrease the distance that the reflected shock wave travels from the point of impact before turning and traveling in the same direction as the penetrator. This distance never exceeded 2 mm. The speed attained by the back of the target decreases as the penetrator thickness decreases.

Pressure profiles along the y-axis are shown in Figures 23 - 25 for the first 23 computational cycles (0.4 μs). Since the pressures are plotted at the centers of each cell, the initial rise in pressure occurs around y = 15.25 mm. For all three cases, in 8 cycles (0.09 μs) the pressure peaks after overshooting the theoretical shock pressure of 3.01 Mbar. Comparing the 23rd cycle for each case, we see that the magnitude of the pressure profiles decreases as the penetrator thickness is decreased.

Pressure and particle velocity profiles along the y-axis, for the three cases, are shown in Figures 26 - 37. The triangular symbol denotes the location of the interface on the y-axis. The decrease in the pressure with a decrease in penetrator thickness is illustrated in these figures.

A comparison of pressure profiles at 0.5-μs intervals in the 15.25-mm y-plane are shown in Figure 38 for the three slab geometries. This y-plane is in the target, 0.25 mm from the front surface. Lower pressures are associated with thinner penetrators.

The positions of the tracer particles, which were initially positioned on the front and back surfaces of the target and the free side of the penetrator, were line-plotted to illustrate the deformation of the penetrator-target configuration. See Figures 39 - 50.* Several penetrator thickness effects are shown. The hole size is decreased

*Note: If the distance between two tracer particles becomes too great, the line plots do not give a true picture of the penetrator-target interface. See Figure 47 (3-mm penetrator).

and the bulge size on the back of the target decreases as the thickness is decreased. The triangular symbols in these figures depict the flow patterns for the copper penetrator; the square symbols, the steel target.

VII. PROBLEM WITH RECTANGULAR GEOMETRY

The TRIDORF code was used to solve the following problem: The penetration of an infinite steel plate, 25.5-mm thick, impacted upon by a semi-infinite, copper bar at 7.5 km/s. The cross section of the bar is a 5.317-mm square, approximately the same cross-sectional area as that of a 6-mm rod. The computational grid was laid out as shown in Figure 51. The overall size of the grid was 25 mm by 50 mm by 25 mm with a corresponding grid size of 15 by 49 by 15 computational cells in the x, y, and z directions, respectively. A non-uniform grid was used, resulting in a rectangular prism as a computational cell. Table I gives the grid coordinates and cell dimensions, dx, dy, and dz. The cell indices are I, J, and K in the x, y, and z directions, respectively.

From the geometry of the problem, the x-coordinate and z-coordinate planes were selected as planes of symmetry with the y-axis being the line of symmetry. Initially, one-fourth of the bar, bounded by the $x = 0.0$ and $x = 2.6585$ planes, the $y = 0.0$ and 15.0 planes, and the $z = 0.0$ and $z = 2.6585$ planes, was positioned in the grid.

The target was initially bounded by the $y = 15.0$ mm and 40.5 mm planes, the former being the front surface of the target. Since the bar's initial motion was in the positive y-direction, the boundary conditions at y-coordinate plane were specified to feed bar material into the grid as a simulation of a semi-infinite bar. The x-coordinate and z-coordinate planes were given reflective boundary conditions. The remainder of the planes, which bound the grid, were given transmittive boundary conditions in order to simulate an infinite target and to permit the flow of material out of the computational region.

The cells, occupying the initial volume of the penetrator, were given the following initial conditions:

1. Density = 8.9 Mg/m^3.
2. Pressure = 0.0 Mbar.
3. X-component of velocity = 0.0 km/s.
4. Y-component of velocity = 7.5 km/s.
5. Z-component of velocity = 0.0 km/s.
6. Specific internal energy = 0.0 J/g.

Similar initial conditions were given to the cells occupying the initial volume of the target except that the density was that of the steel target material, 7.86 Mg/m^3, and the y-component of the velocity was zero.

Table I. Grid Coordinates and Cell Dimensions

I	x (mm)	dx (mm)	J	y (mm)	dy (mm)	K	z (mm)	dz (mm)
1	0.5317	0.5317	1	6.2000	6.2000	1	0.5317	0.5317
2	1.0634	0.5317	2	8.9000	2.7000	2	1.0634	0.5317
3	1.5951	0.5317	3	10.0000	1.1000	3	1.5951	0.5317
4	2.1268	0.5317	4	10.5000	0.5000	4	2.1268	0.5317
5	2.6585	0.5317	5	11.0000	0.5000	5	2.6585	0.5317
6	3.3241	0.6656	6	11.5000	0.5000	6	3.3241	0.6656
7	4.1574	0.8333	7	12.0000	0.5000	7	4.1574	0.8333
8	5.2006	1.0432	8	12.5000	0.5000	8	5.2006	1.0432
9	6.5065	1.3059	9	13.0000	0.5000	9	6.5065	1.3059
10	8.1414	1.6349	10	13.5000	0.5000	10	8.1414	1.6349
11	10.1880	2.0466	11	14.0000	0.5000	11	10.1880	2.0466
12	12.7502	2.5622	12	14.5000	0.5000	12	12.7502	2.5622
13	15.9577	3.2075	13	15.0000	0.5000	13	15.9577	3.2075
14	19.9731	4.0154	14	15.5000	0.5000	14	19.9731	4.0154
15	25.0000	5.0269	15	16.0000	0.5000	15	25.0000	5.0269
			16	16.5000	0.5000			
			17	17.0000	0.5000			
			18	17.5000	0.5000			
			19	18.0000	0.5000			
			20	18.5000	0.5000			
			21	19.0000	0.5000			
			22	19.5000	0.5000			
			23	20.0000	0.5000			
			24	20.5300	0.5300			
			25	21.0900	0.5600			
			26	21.6800	0.5900			
			27	22.3000	0.6200			
			28	22.9600	0.6600			
			29	23.6600	0.7000			
			30	24.4000	0.7400			
			31	25.1800	0.7800			
			32	26.0100	0.8300			
			33	26.8800	0.8700			
			34	27.8000	0.9200			
			35	28.7800	0.9800			
			36	29.8100	1.0300			
			37	30.9000	1.0900			
			38	32.0500	1.1500			
			39	33.2700	1.2200			
			40	34.5600	1.2900			
			41	35.9200	1.3600			
			42	37.3600	1.4400			
			43	38.8000	1.5200			
			44	40.5000	1.6200			
			45	42.2100	1.7100			
			46	44.0100	1.8000			
			47	45.9000	1.8900			
			48	47.8900	1.9900			
			49	50.0000	2.1100			

Tracer particles were positioned at 0.5-mm increments in the bar and target along the line of symmetry. Also, tracer particles were fed into the grid with the bar material being supplied into the computational grid. The motion of these tracer particles along the line of symmetry is shown in Figure 52. A transmitted and a reflected shock wave, located by the change in the direction of the tracer particle paths, emanate from the point of impact (y = 15.0 mm). Initially both of these waves have the speeds determined with the one-dimensional case. However, after about 0.30 μs, the rarefaction wave from the free surfaces of the bar reaches the line of symmetry of the bar and relieves the pressure in the shock wave moving into the bar. Having traveled no more than 2 mm from the point of impact, the shock wave turns and travels in the same direction as the bar.

Pressure profiles along the line of symmetry are shown in Figure 53 for the first 81 computational cycles (0.4 μs); however, only the odd numbered cycles are shown. Since the pressures are plotted in the centers of each cell, the initial rise in pressure occurs around y = 15.25 mm. In 13 cycles (0.10 μs) the pressure peaks after overshooting the theoretical shock pressure of 3.01 Mbar. Thereafter, the magnitude of the pressure profile decreases as the transmitted and reflected shock wave fronts form and move away from each other.

Pressure and particle velocity profiles along the line of symmetry are shown in Figures 54 - 57. The triangular symbol locates the position of the interface on the line of symmetry. The peak pressure of about 0.7 Mbar, shown at 2.0 μs, persists until it is affected by the pressure release wave coming off the back surface of the target (y = 40.5 mm) at about 4.2 μs.

Figure 58 shows pressure profiles at 0.5 μs intervals in the 15.25-mm y-plane, which is 0.25 mm from the front surface of the target, and the z-coordinate plane. The "radial" pressure in the bar, having a semi-thickness of 2.6585 mm, can be observed to be decreasing with time. Also, the propagation of the shock front in the x-direction is shown.

Tracer particles were also positioned along the free surfaces of the bar-target configuration in the z-coordinate plane. When the coordinates of these tracer particles are line-plotted as shown in Figures 59 - 61, the deformation of the bar and the target in the z-coordinate plane are depicted.

VIII. DISCUSSION AND CONCLUSIONS

Although one-dimensional shock-wave theory cannot be used to predict two and three-dimensional impact phenomena, it is useful for estimating one component of the overall grid size and the real time for running two- or three-dimensional problems on the computer.

The results of the one-dimensional finite-difference computations showed some of the characteristics of the DORF-9 code and the agreement of the results with one-dimensional shock-wave theory.

The effects of cylindrical and slab geometries and cylindrical and rectangular geometries are compared for several impact phenomena. A comparison of the motions of the shock waves, transmitted into the target at impact and reflected into the penetrator along the center line, is shown in Figure 63. The left graph shows that, as the thickness of the penetrator plate decreases, the motion of the transmitted shock waves approaches that of the rod. However, there is a limit to how thin a penetrator plate can be, since at least 3 or 4 computational cells should represent the semi-thickness of the plate.[9] Furthermore, as the grid is made finer, the computational time increases.

The left graph in Figure 63 also shows the effect of penetrator plate thickness on the reflected shock wave: The thicker the plate is, the farther the reflected shock wave travels into the penetrator and the longer the time before the wave turns and moves in the direction of the penetrator. Note that the rod curve, after 2 μs, falls between the 3- and 4-mm plate curves.

The right side of Figure 63 shows the effects of rod and bar penetrators on the shock wave motion along the center lines. The transmitted wave motion is about the same for both penetrators; the reflected wave motion shows the effect of the rarefaction wave from the sides of the bar reaching the center line before the rarefaction wave from the surface of the rod.

The displacement of the center of the back of the target is shown in Figure 64. The bar and rod curves are in good agreement. As the penetrator plate thickness is decreased, the plate curves tend toward the rod curve; however, the agreement is poor. Furthermore, a comparison of the bulges on the back of the target at 5 μs (Figures 17 and 47) shows that the bulges are larger for the slab geometries than for the cylindrical geometry. Consequently, it would not be desirable, in spallation studies, to simulate three-dimensional impacts two-dimensionally.

A comparison of the penetration histories for cylindrical and slab geometries is shown in Figure 65. Initially, all the penetration motion is identical. Then the rod moves off at the greatest speed (slope). The curves for the 3- and 4-mm plates coincide and noticeably depart from the 6-mm plate after about 5 μs. At any given time, the curves are no more than 0.7 mm apart.

---

[9] V. Kucher, "Preliminary Computer Computations for Slender Rod Impact Problems," Ballistic Research Laboratory Report No. 1957, Feb 1977. (AD #A036995)

Good agreement between the penetration for the rod and bar is depicted in Figure 66. Also illustrated is the fact that penetration rate cannot be determined by a one-dimensional finite-difference code.

The diameter or width, D, of the holes at the front surface of the target is shown in Figure 67 as they change with time. Decreasing the thickness of the penetrator plates decreases the rate of hole growth. The diameter of the hole initially made by the rod is the same as that of the 6-mm plate; eventually, the curve for the rod falls between the 3- and 4-mm plate curves. There is good agreement between the rod and bar curves.

Figure 68 is similar to Figure 67 except that D is measured in the middle of the target. The effect of the thickness of the plates is the same as that at the surface of the target. The curve for the rod falls between the 3- and 4-mm plate curves. At any time being considered, the average difference between the rod and bar curves is about 0.7 mm.

The propagation of pressure peaks normal to the center lines of the penetrators is shown in Figure 69. This motion occurs in the z = 15.25-mm plane, just inside the front surface of the target. The penetrator plate curves differ mainly by constant time increments; this is also the case for the rod and bar curves.

Hole profiles for the cylindrical, slab, and retangular geometries at 5 μs are shown in Figure 70. The volume or size of the hole decreases as the penetrator plate thickness is decreased. The size of the hole made by the rod falls between the holes made by the 3- and 4-mm plates. The size of the hole made by the bar is smaller than that made by the rod. Note that at this time, the deepest penetration was made by the rod and the bar.

The comparisons that were made between the rod and the penetrator plates show how the results from slab geometry are to be interpreted if, for economical reasons or the unavailability of a three-dimensional code, the problem must be simulated by slab geometry. A penetrator plate, between 3- and 4-mm thick, could provide information on hole size, penetration, and reflected shock-wave motion, as a simulation of a 6-mm penetrator rod, that might be acceptable to the user.

The comparisons that were made between the rod and the bar indicate that, for the cross-sectional area being considered, the bar can be used to simulate a rod. It should be pointed out that, if the grid were made finer, the circular cross section of the rod could be approximated in rectangular coordinates.

The one-dimensional case required 50 computational cells; each of the two-dimensional cases, 5000 computational cells and a running time that was 20 times longer than the one-dimensional case. The three-dimensional case with 11,025 computational cells ran 2.5 times longer

than each of the two-dimensional cases. This running time would have been much longer if the grid size were of the same uniformity as for the two-dimensional cases. In this case, 250,000 computational cells would have been required.

ACKNOWLEDGMENTS

The author acknowledges Allen Delp, James Wallace, and Joseph Correri for their computer and graphical support.

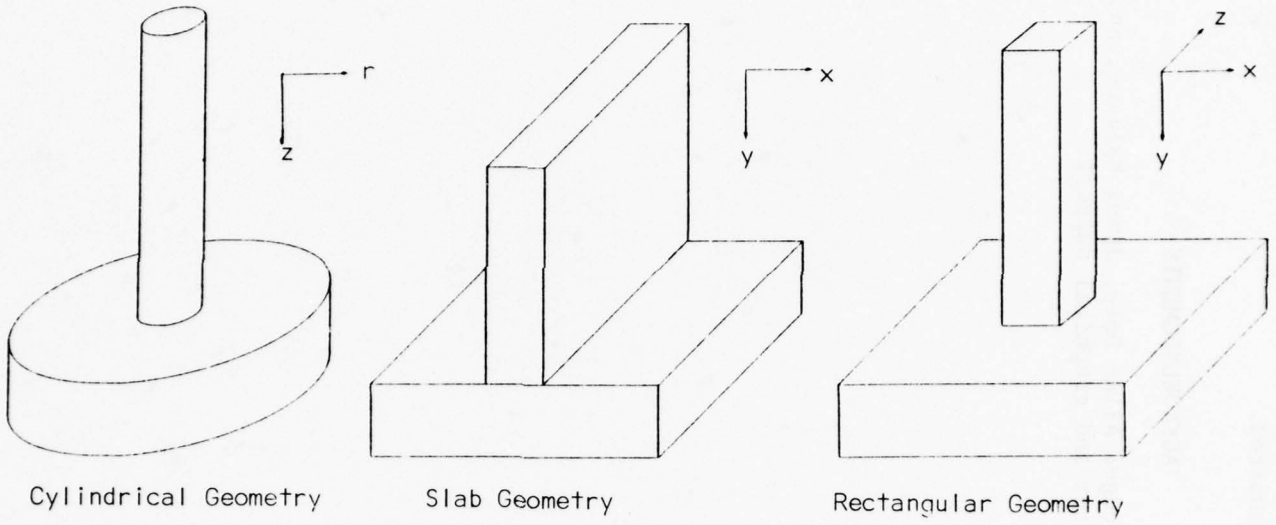

Figure 1. Penetrator-Target Geometries

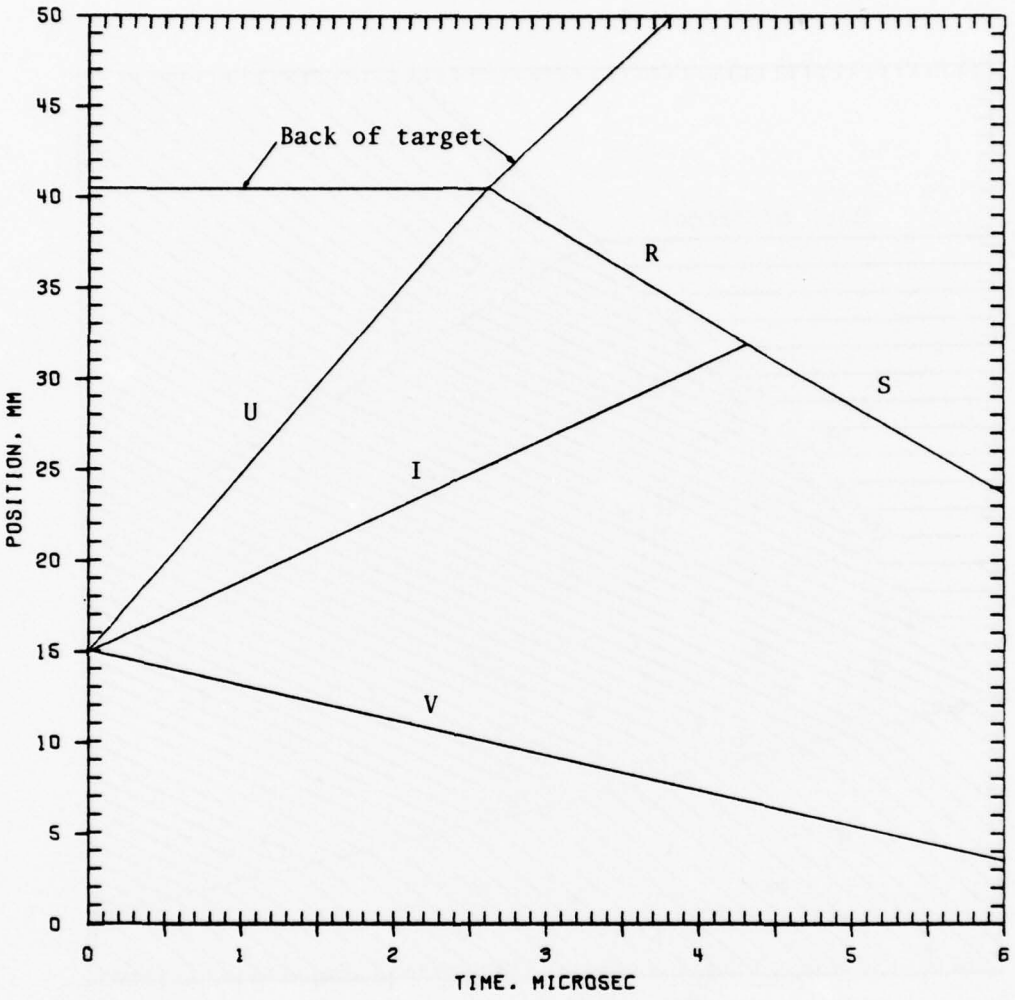

Figure 2. Shock-Wave Diagram

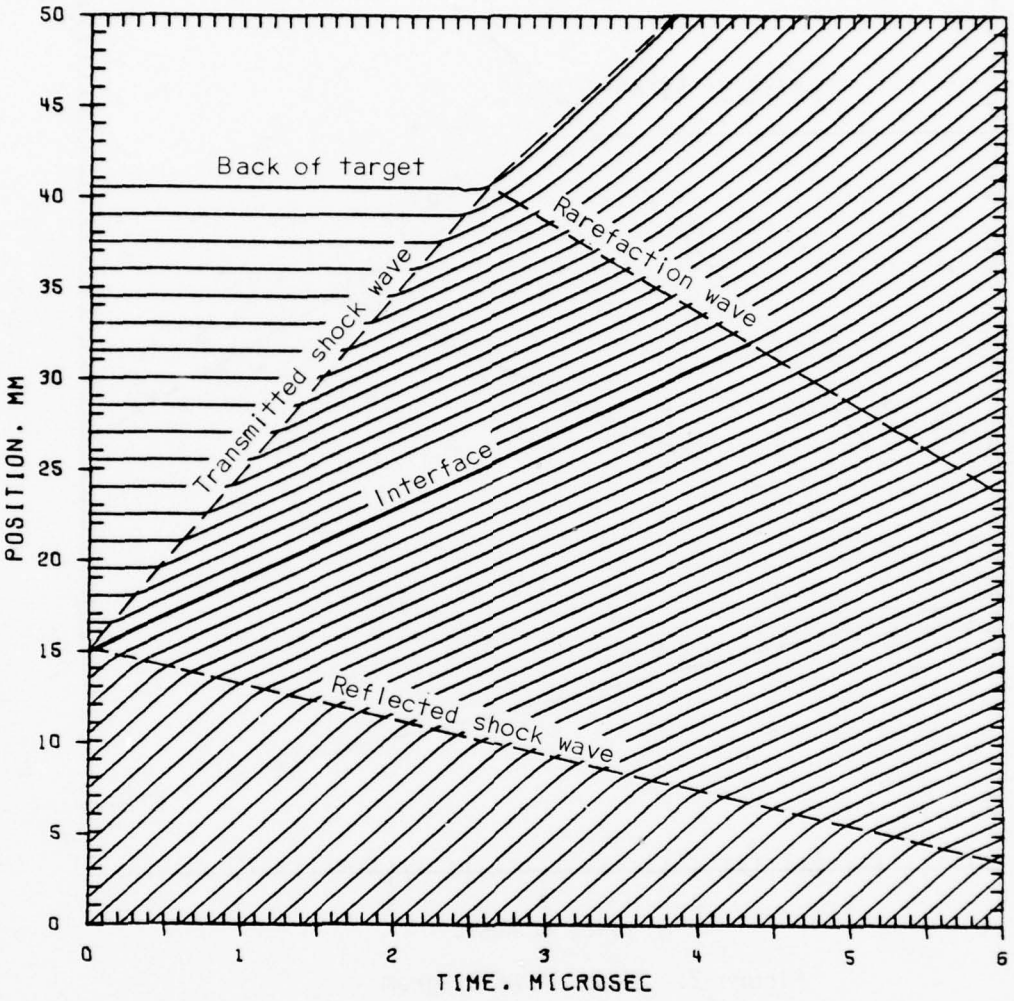

Figure 3. One-Dimensional Motion of Tracer Particles

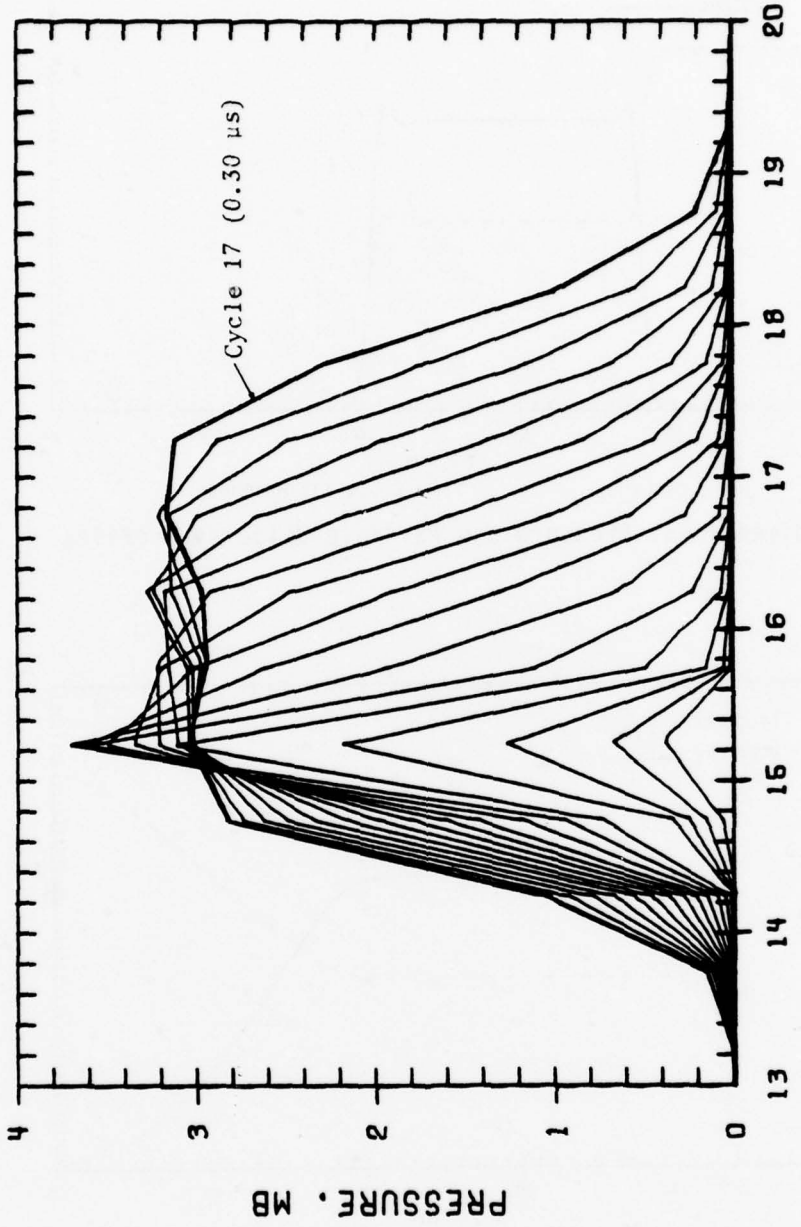

Figure 4. One-Dimensional Pressure Profiles

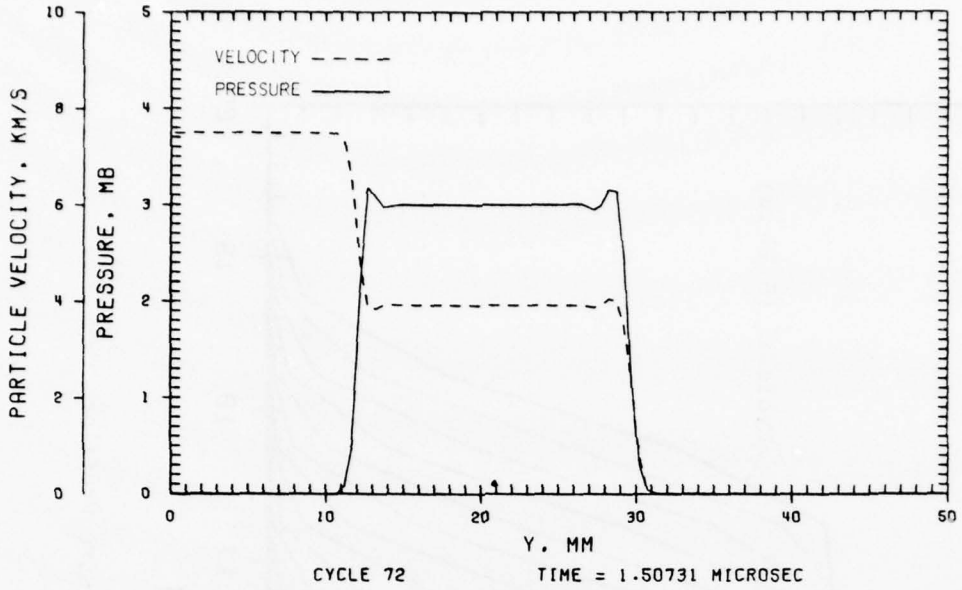

Figure 5. One-Dimensional Pressure and Particle Velocity Profiles

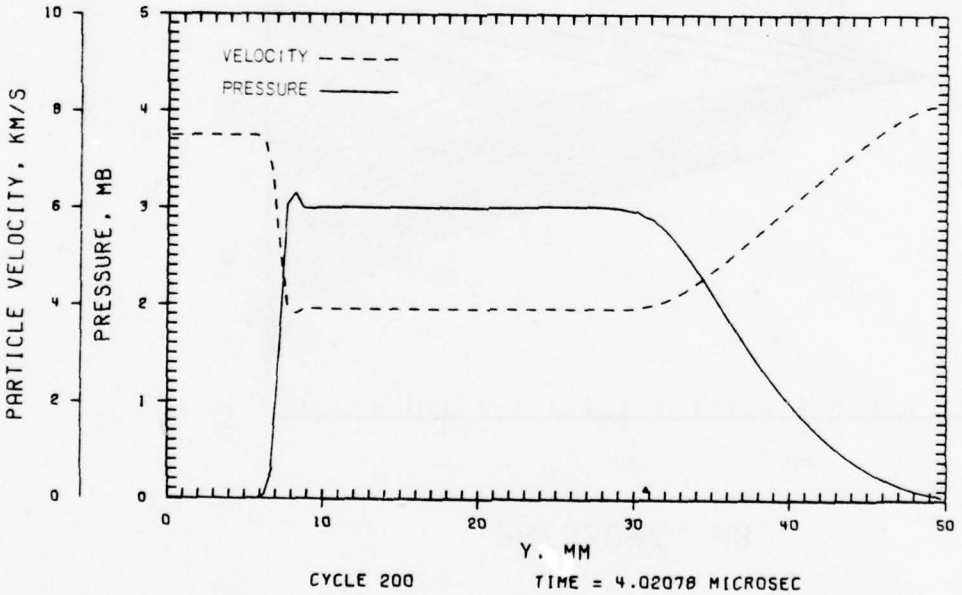

Figure 6. One-Dimensional Pressure and Particle Velocity Profiles

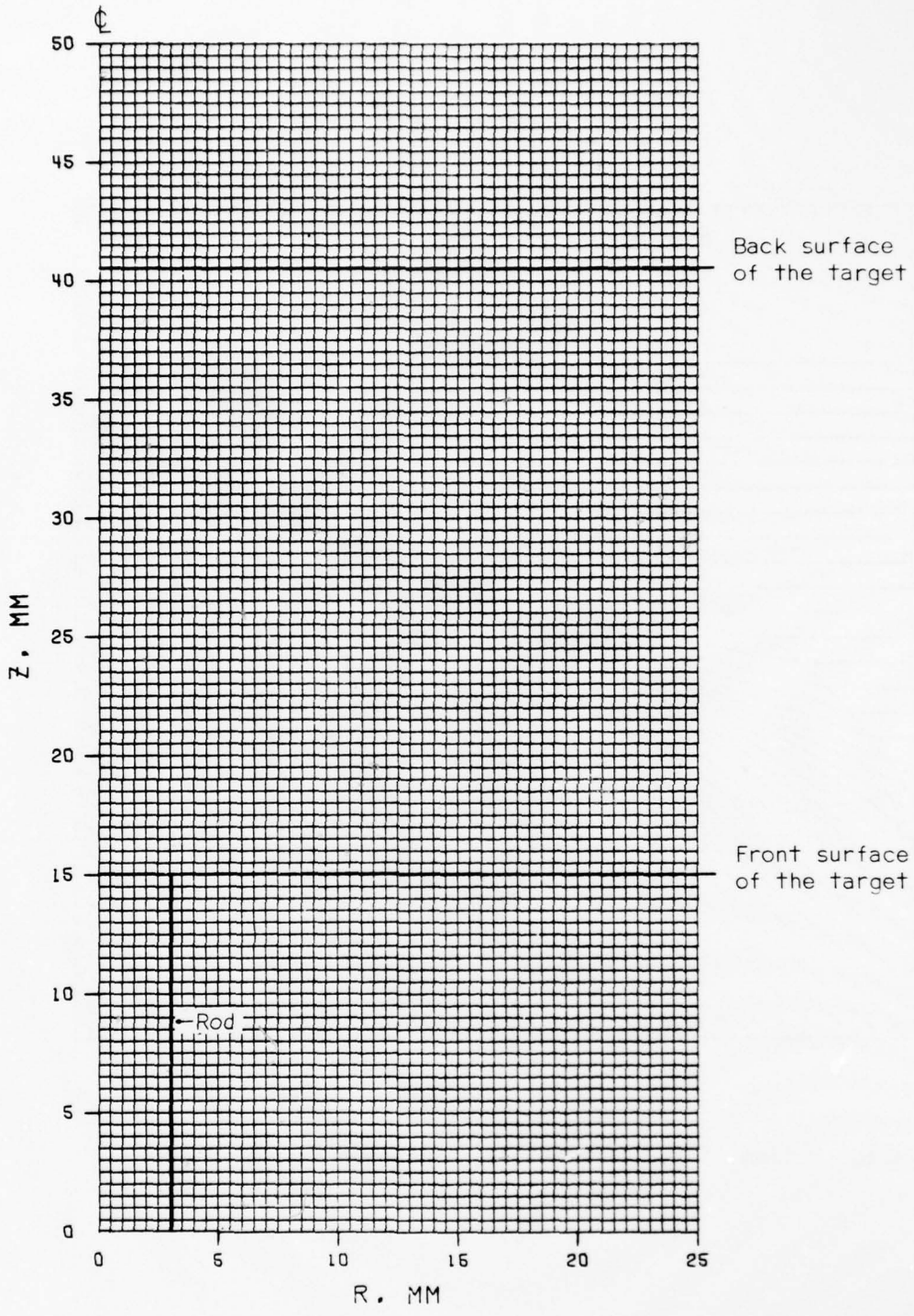

Figure 7. Two-Dimensional Computational Grid for Cylindrical Geometry

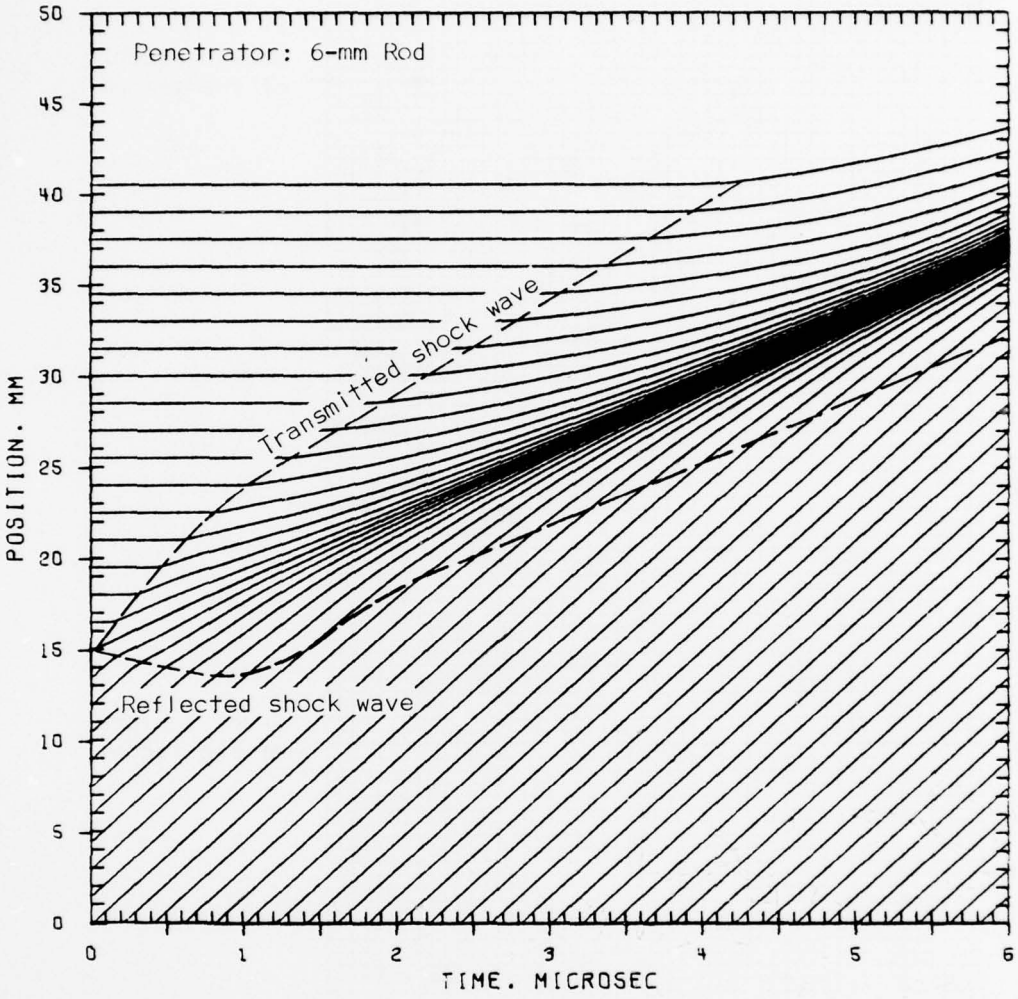

Figure 8. Motion of Tracer Particles along the Axis of Symmetry

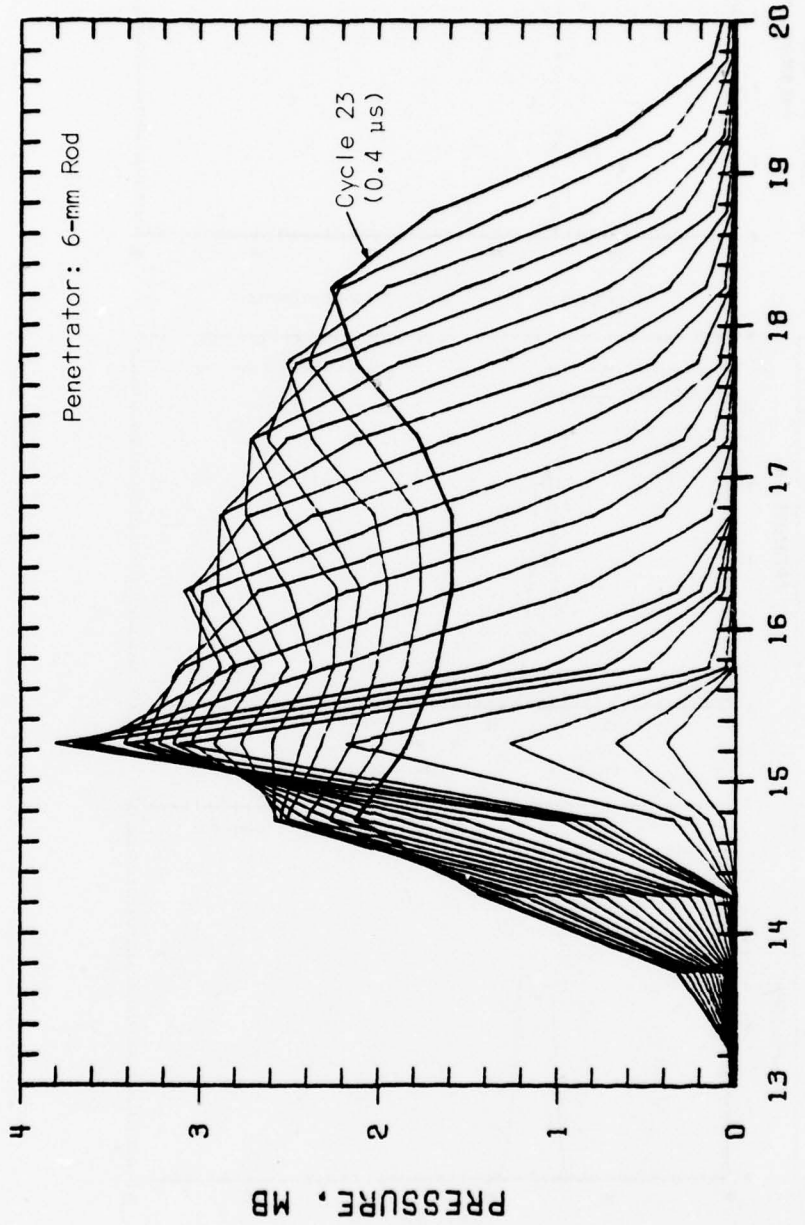

Figure 9. Pressure Profiles along the Axis of Symmetry

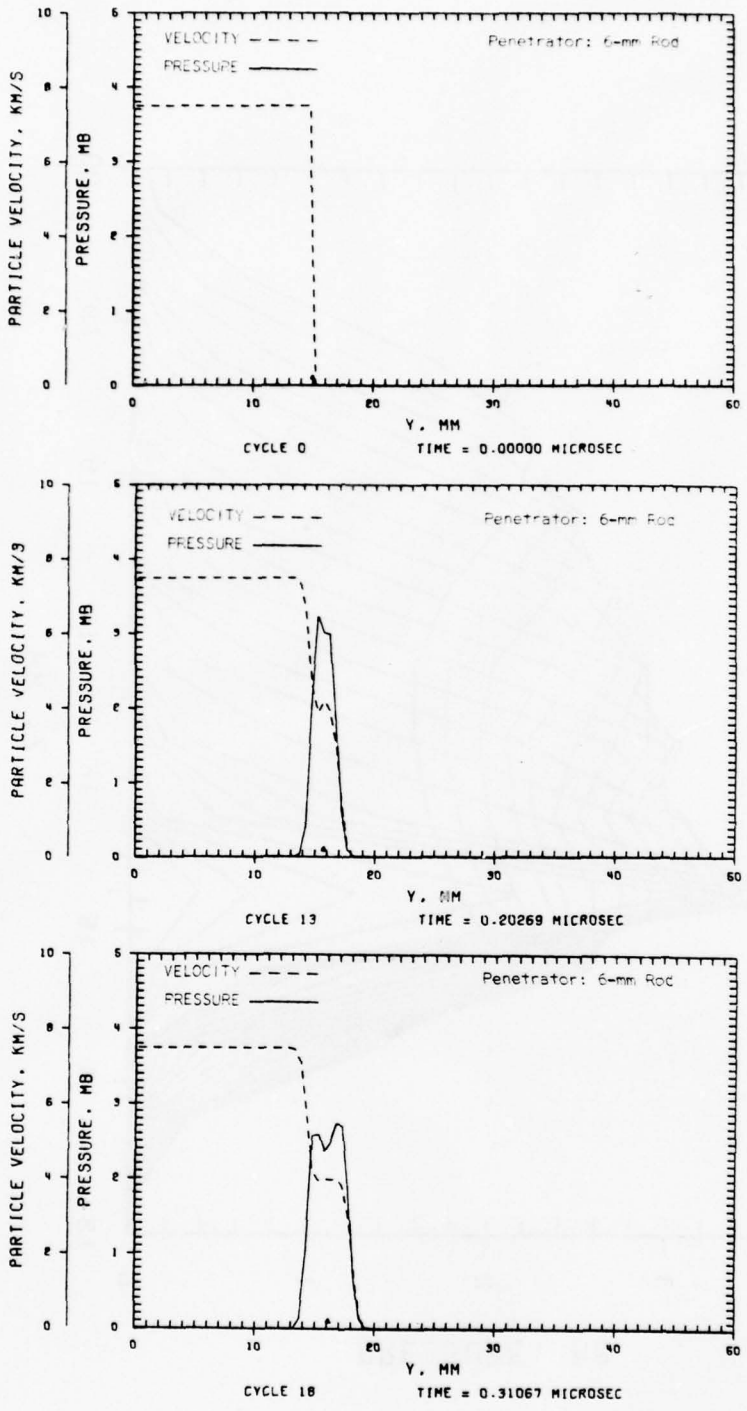

Figure 10. Pressure and Particle Velocity Profiles along the Axis of Symmetry

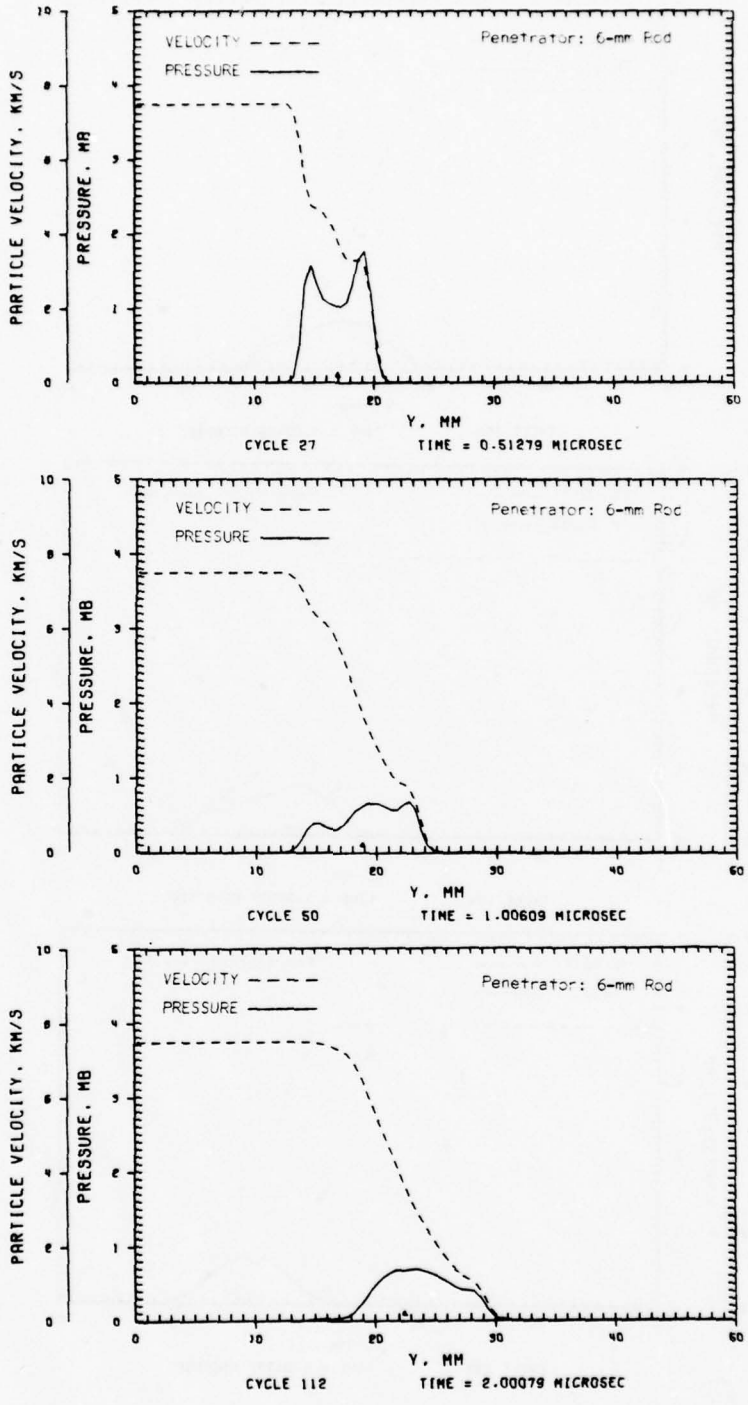

Figure 11. Pressure and Particle Velocity Profiles along the Axis of Symmetry

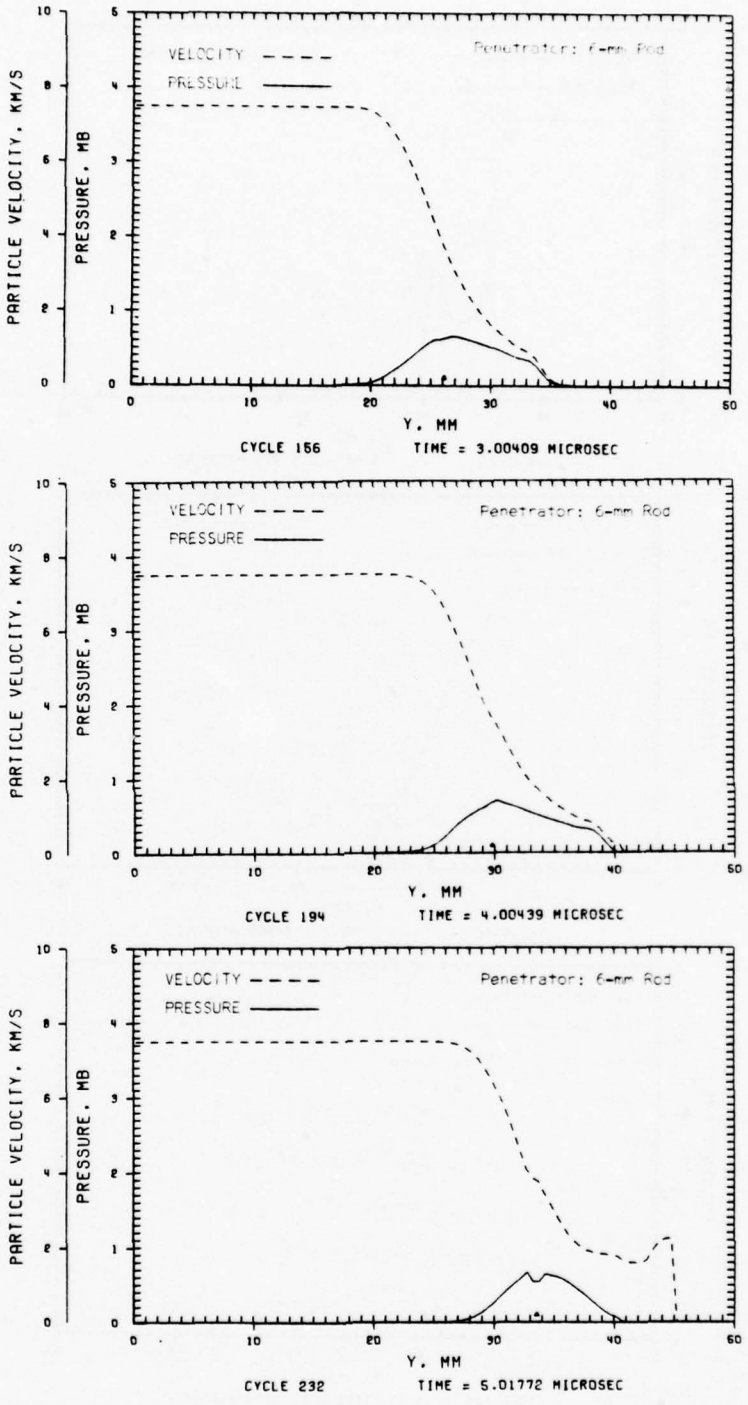

Figure 12. Pressure and Particle Velocity Profiles along the Axis of Symmetry

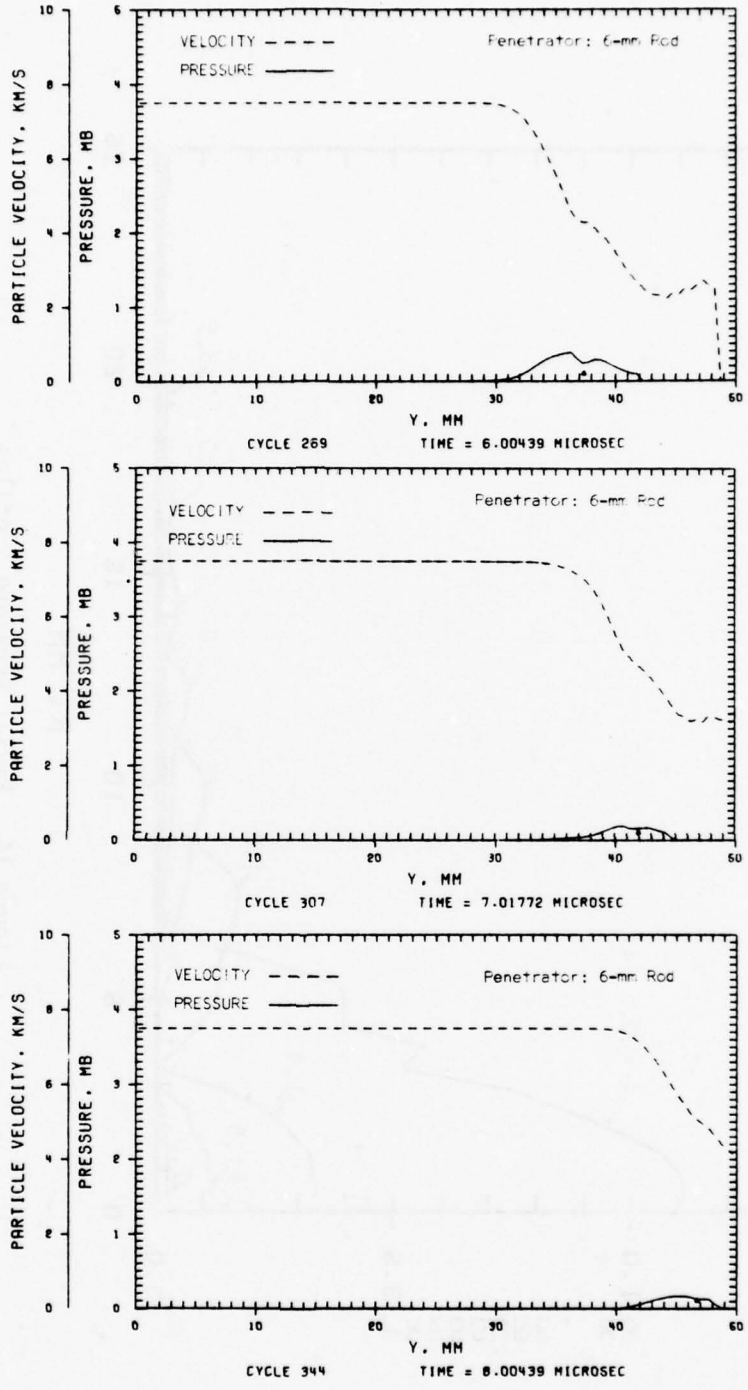

Figure 13. Pressure and Particle Velocity Profiles along the Axis of Symmetry

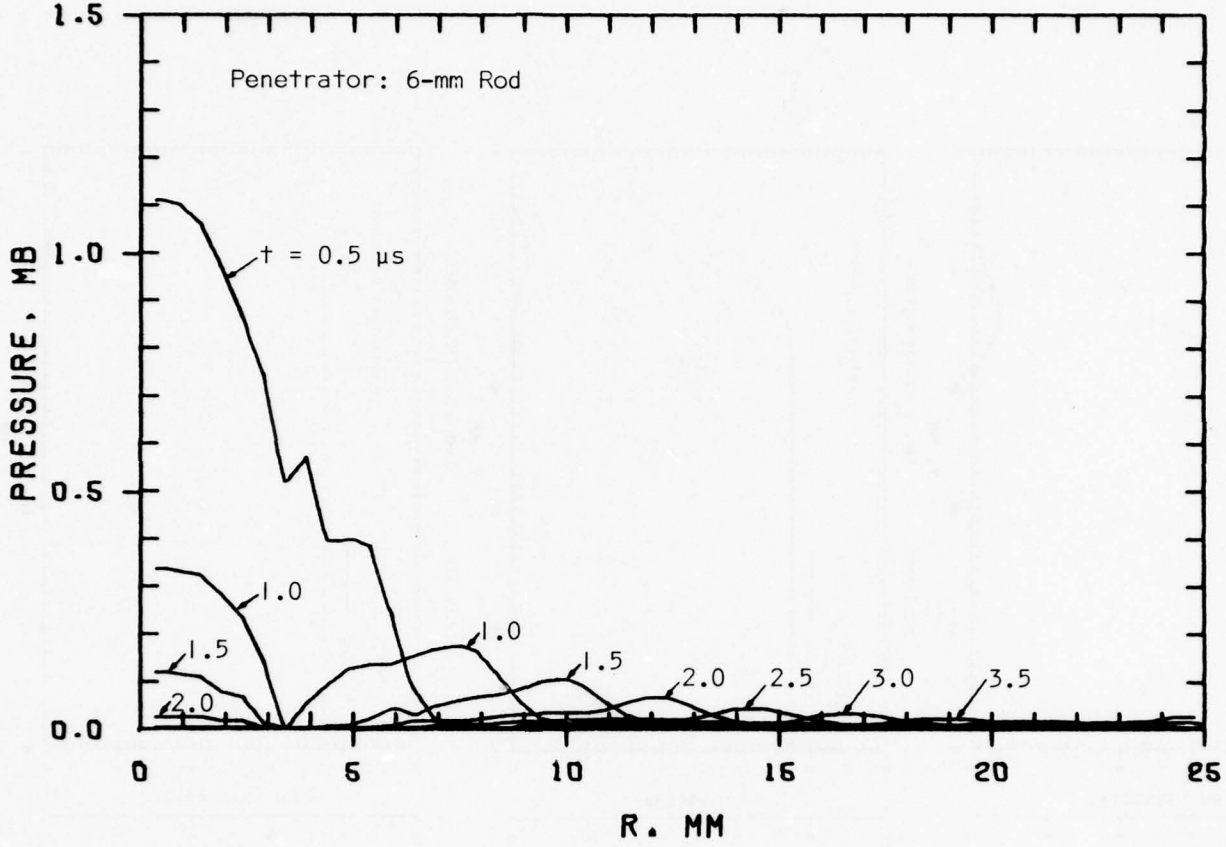

Figure 14. Radial Pressure Profiles

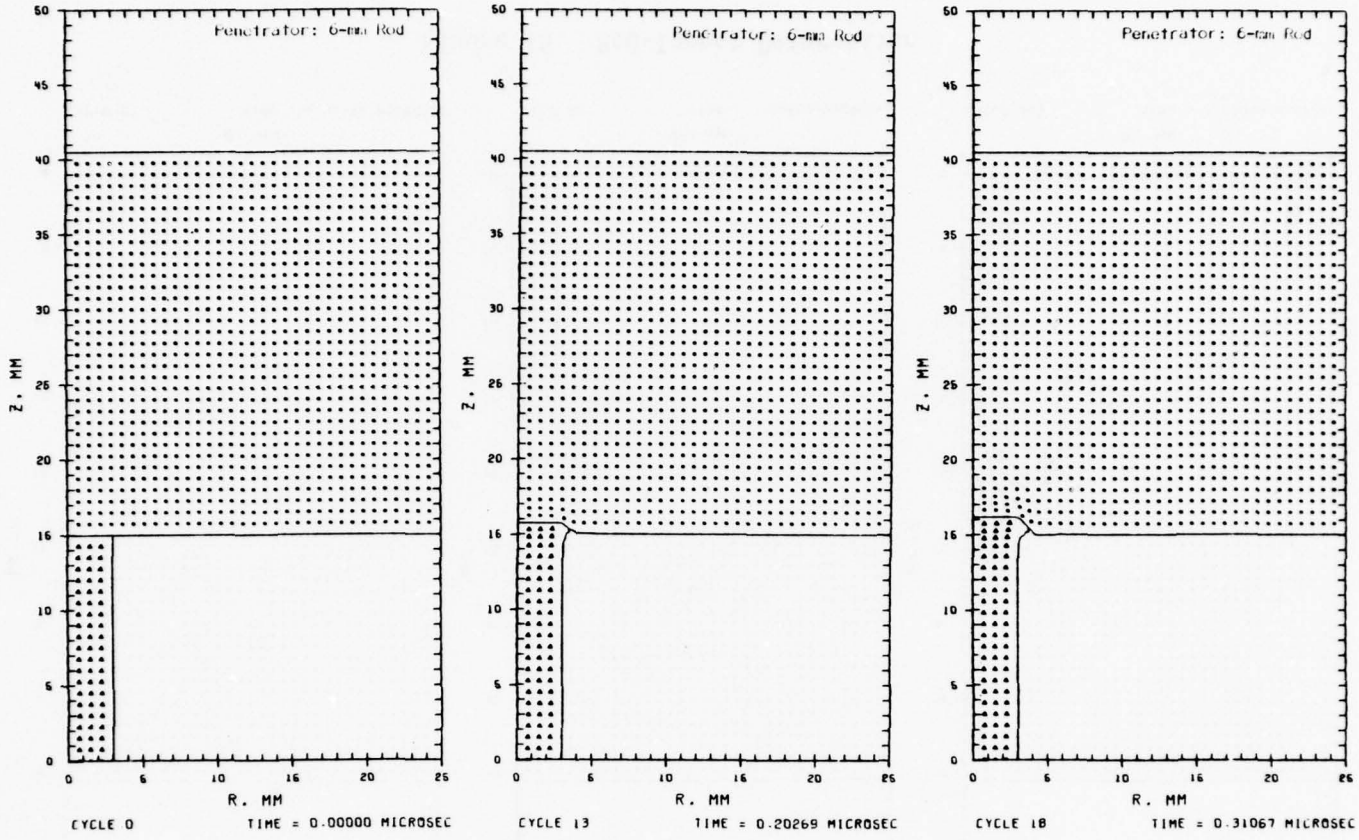

Figure 15. Rod-Target Deformation

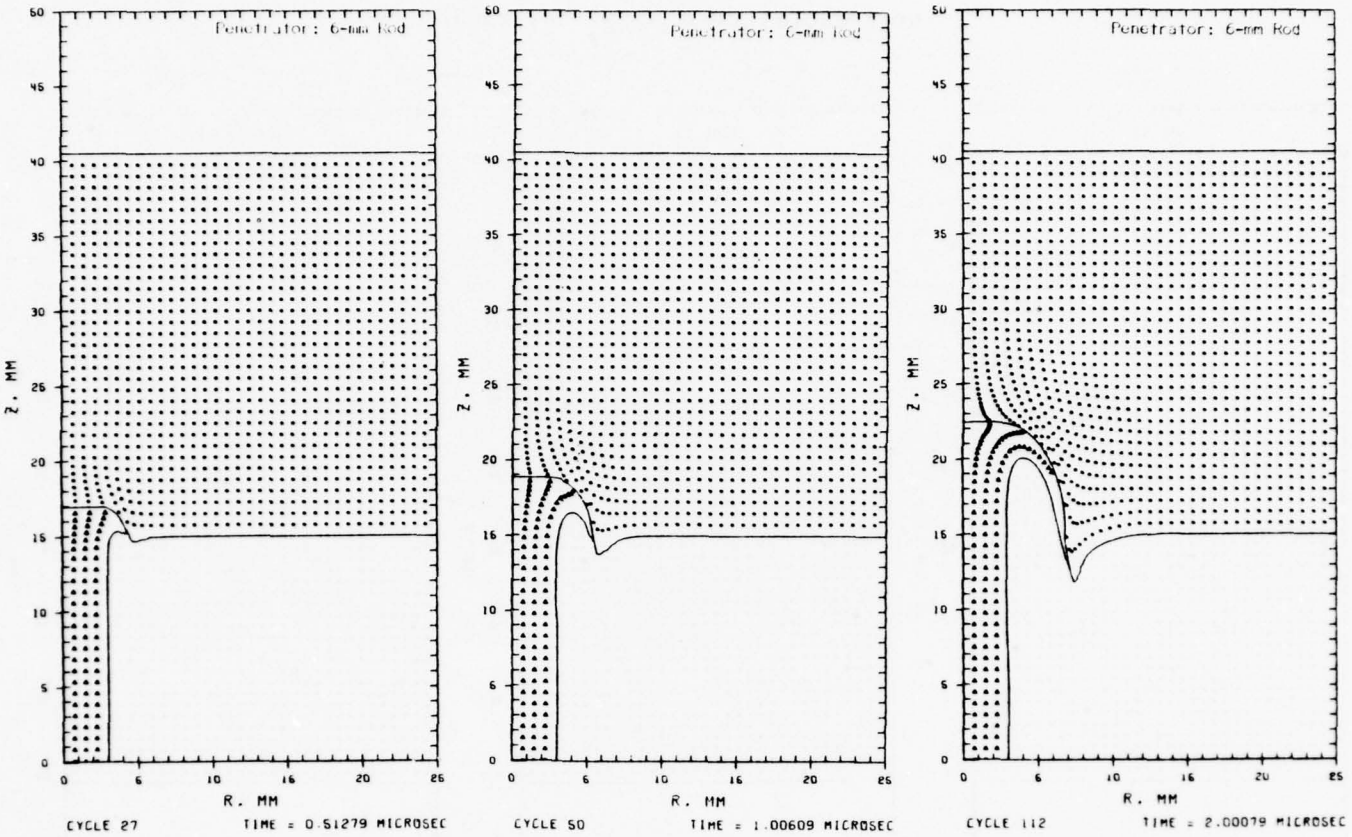

Figure 16. Rod-Target Deformation

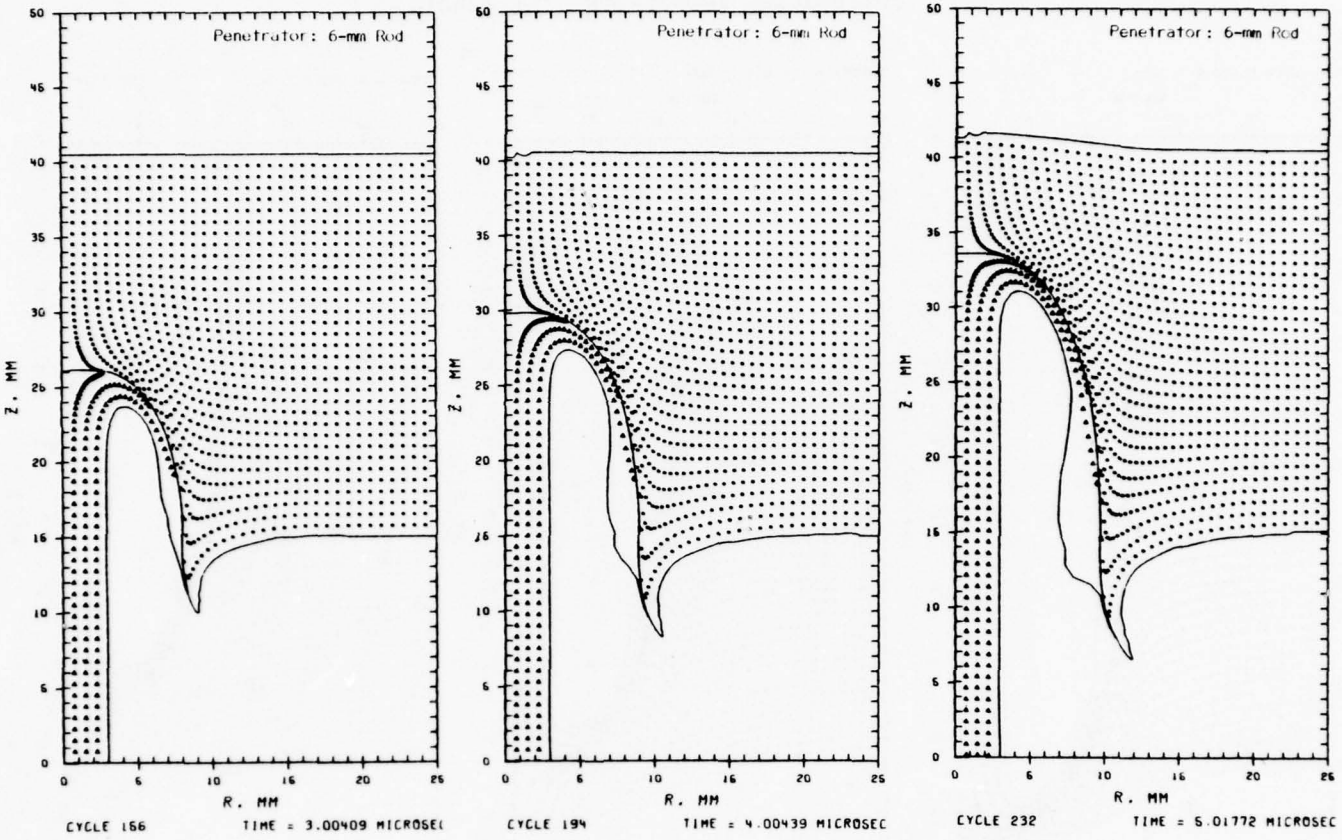

Figure 17. Rod-Target Deformation

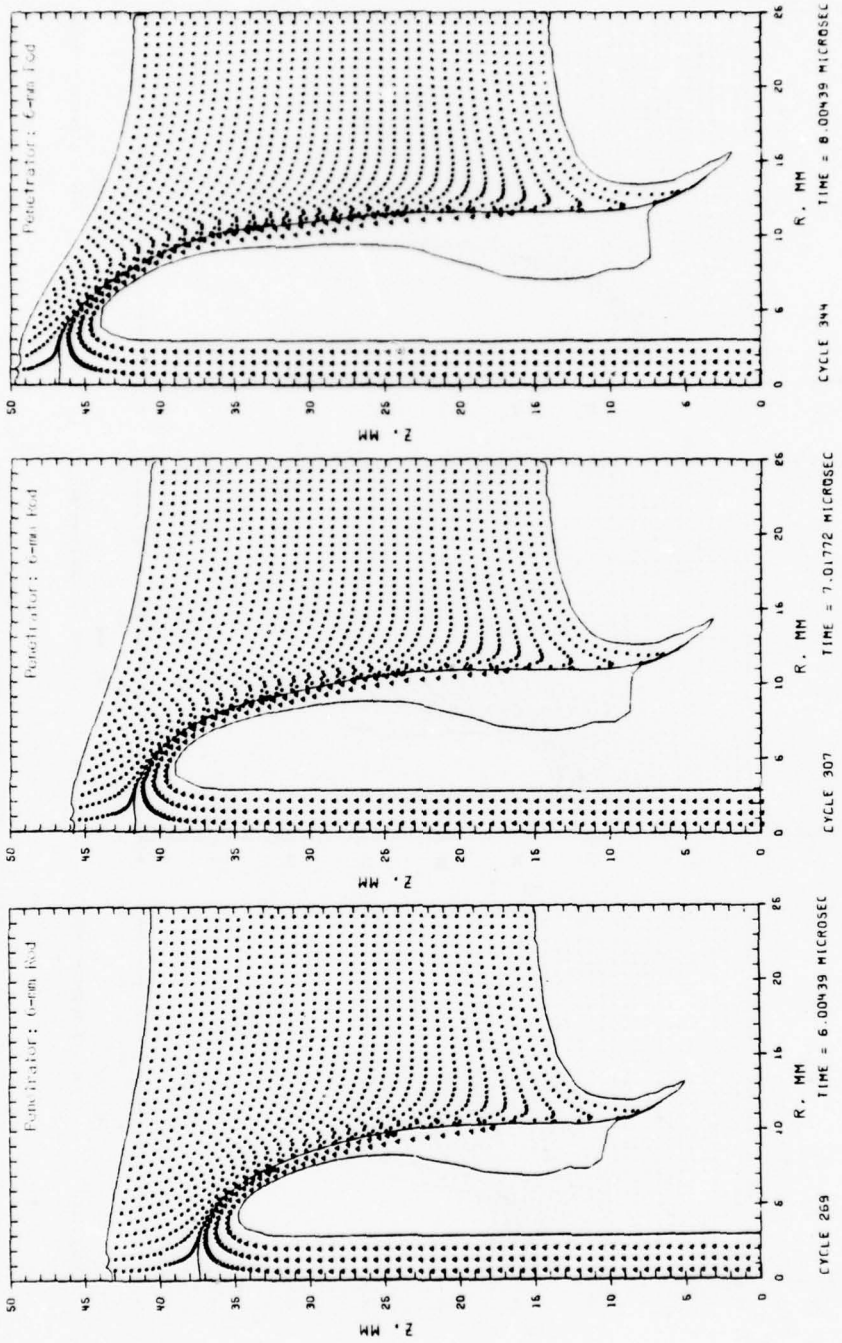

Figure 18. Rod-Target Deformation

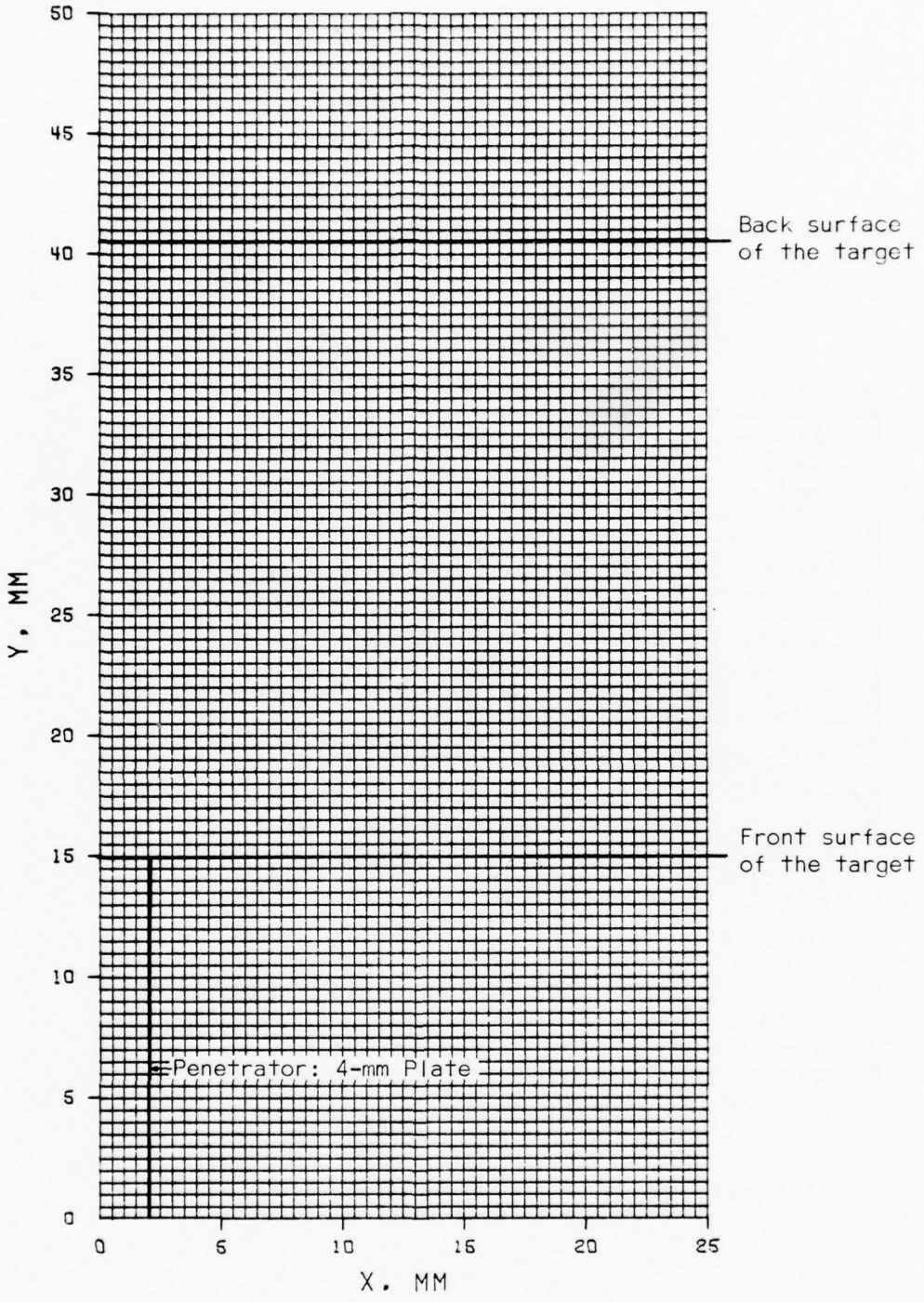

Figure 19. Two-Dimensional Computational Grid for Slab Geometry

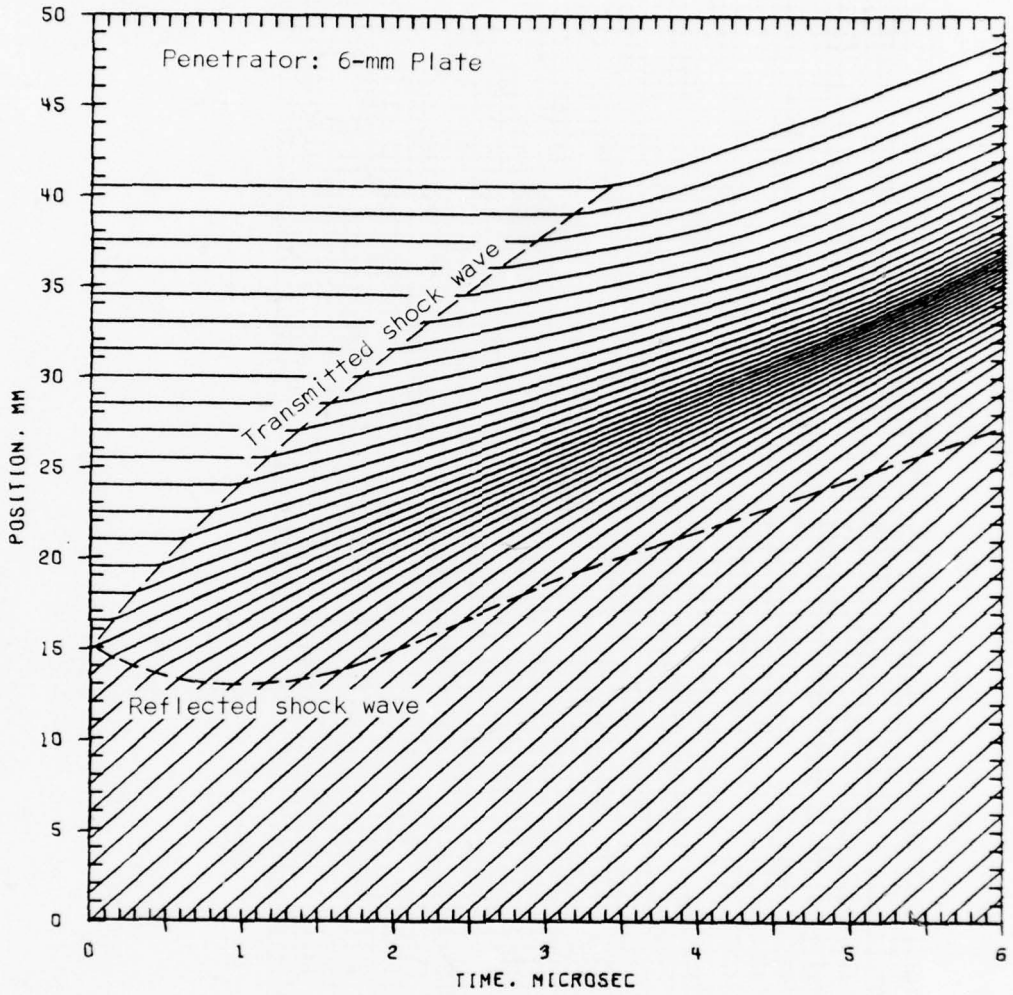

Figure 20. Motion of Tracer Particles along the Y-Axis for the 6-mm Penetrator Plate

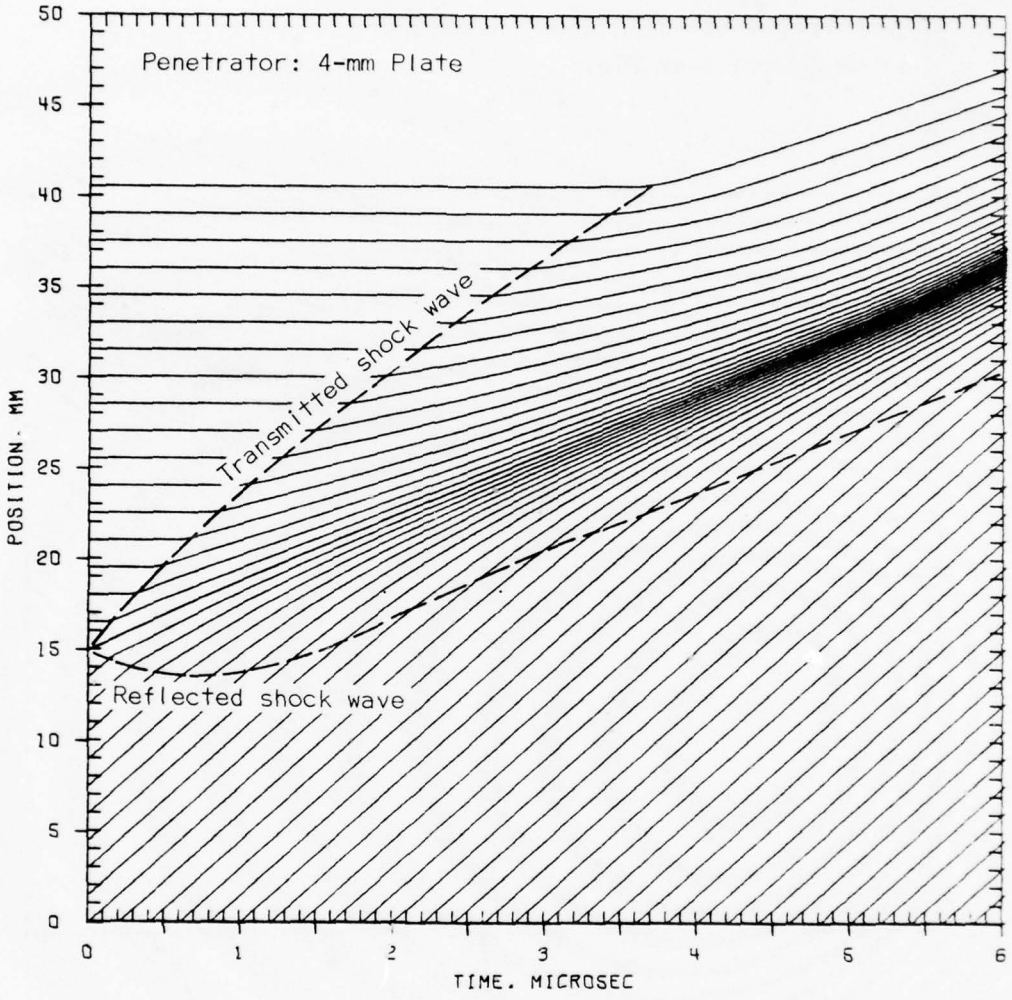

Figure 21. Motion of Tracer Particles along the Y-Axis for the 4-mm Penetrator Plate

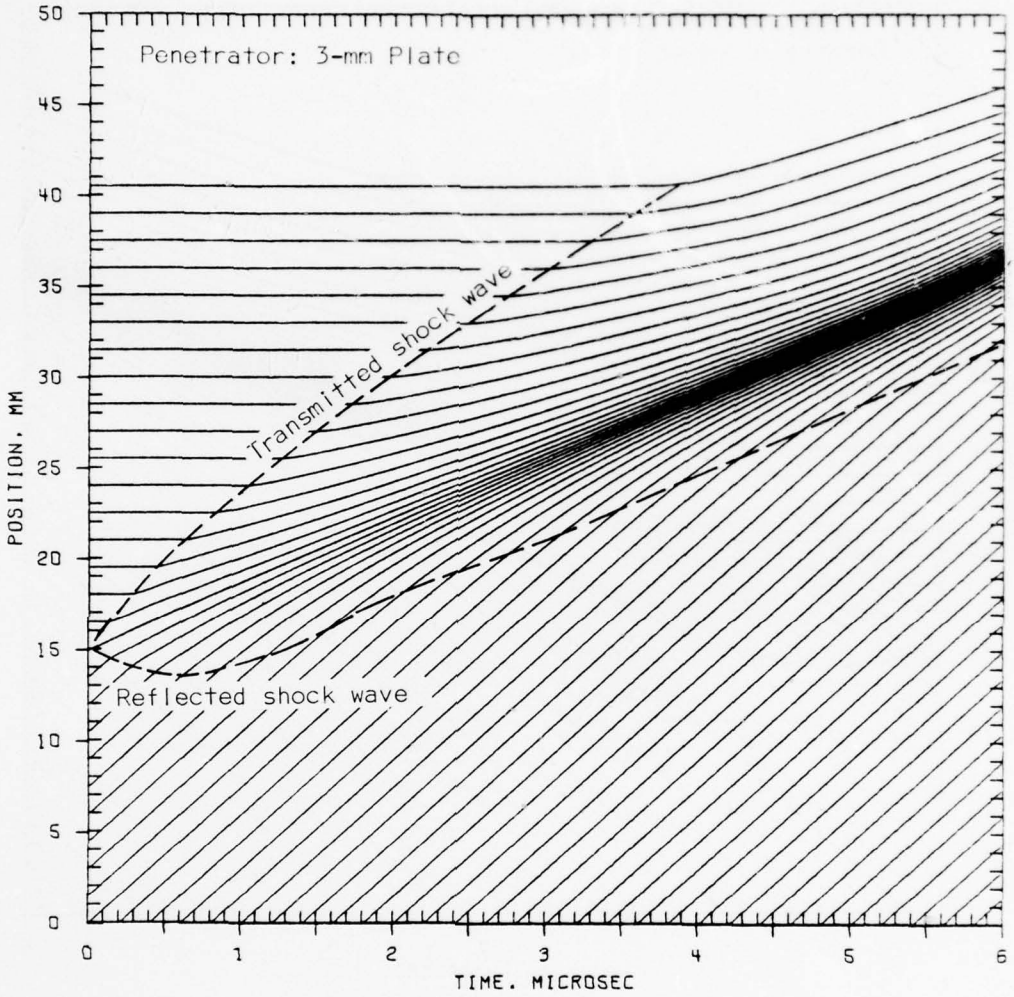

Figure 22. Motion of Tracer Particles along the Y-Axis for the 3-mm Penetrator Plate

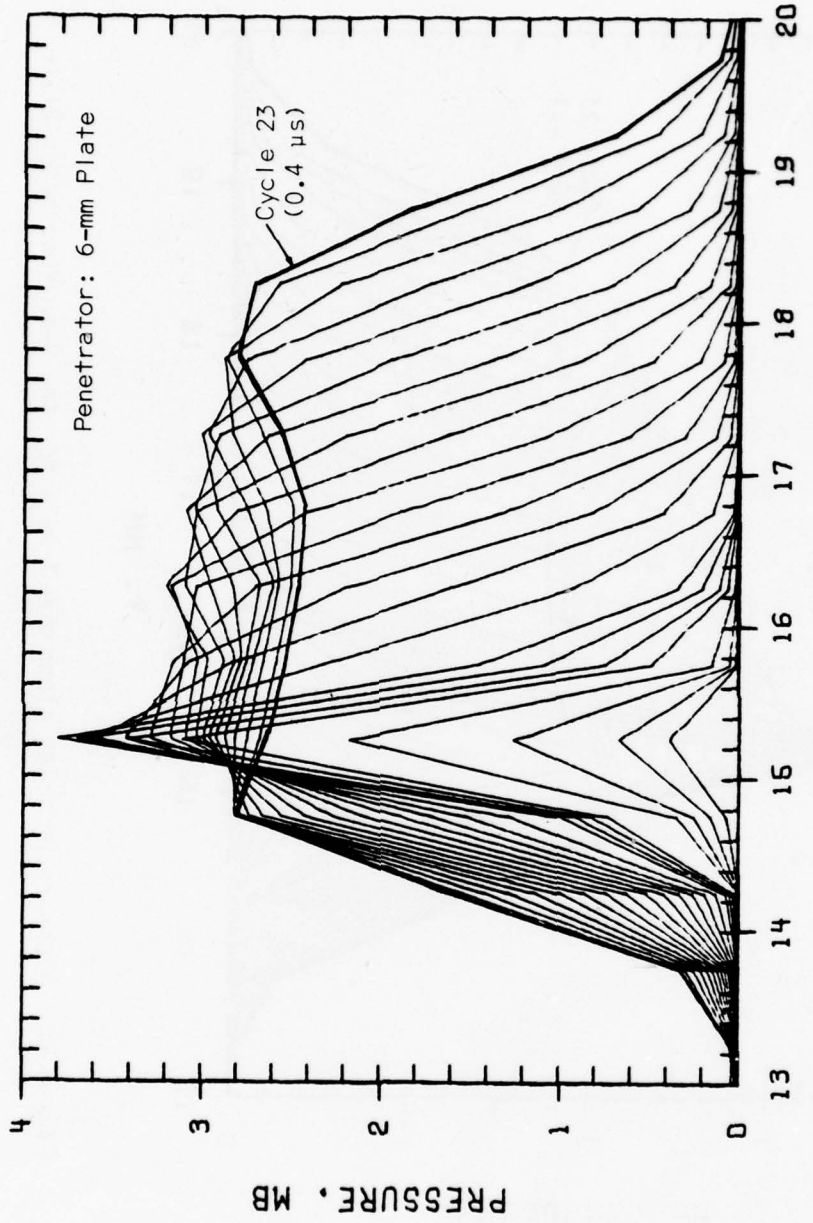

Figure 23. Pressure Profiles along the Y-Axis for the 6-mm Penetrator Plate

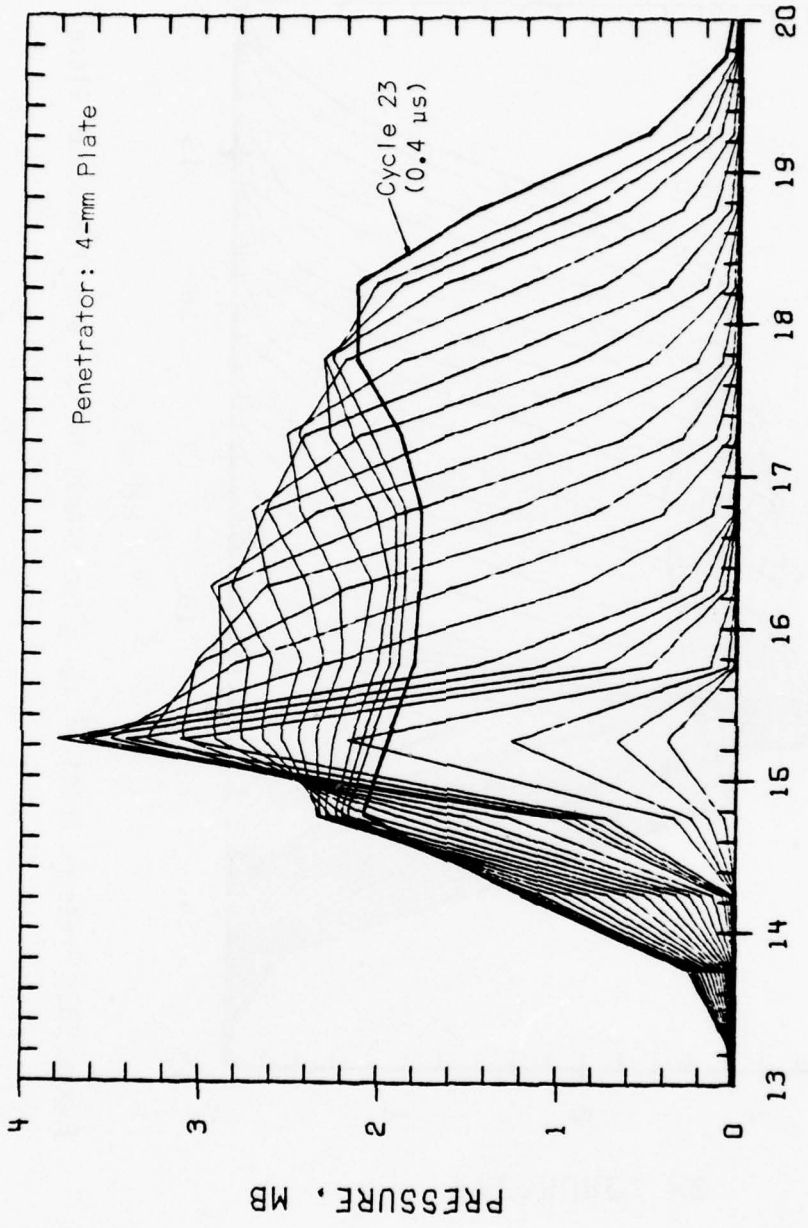

Figure 24. Pressure Profiles along the Y-Axis for the 4-mm Penetrator Plate

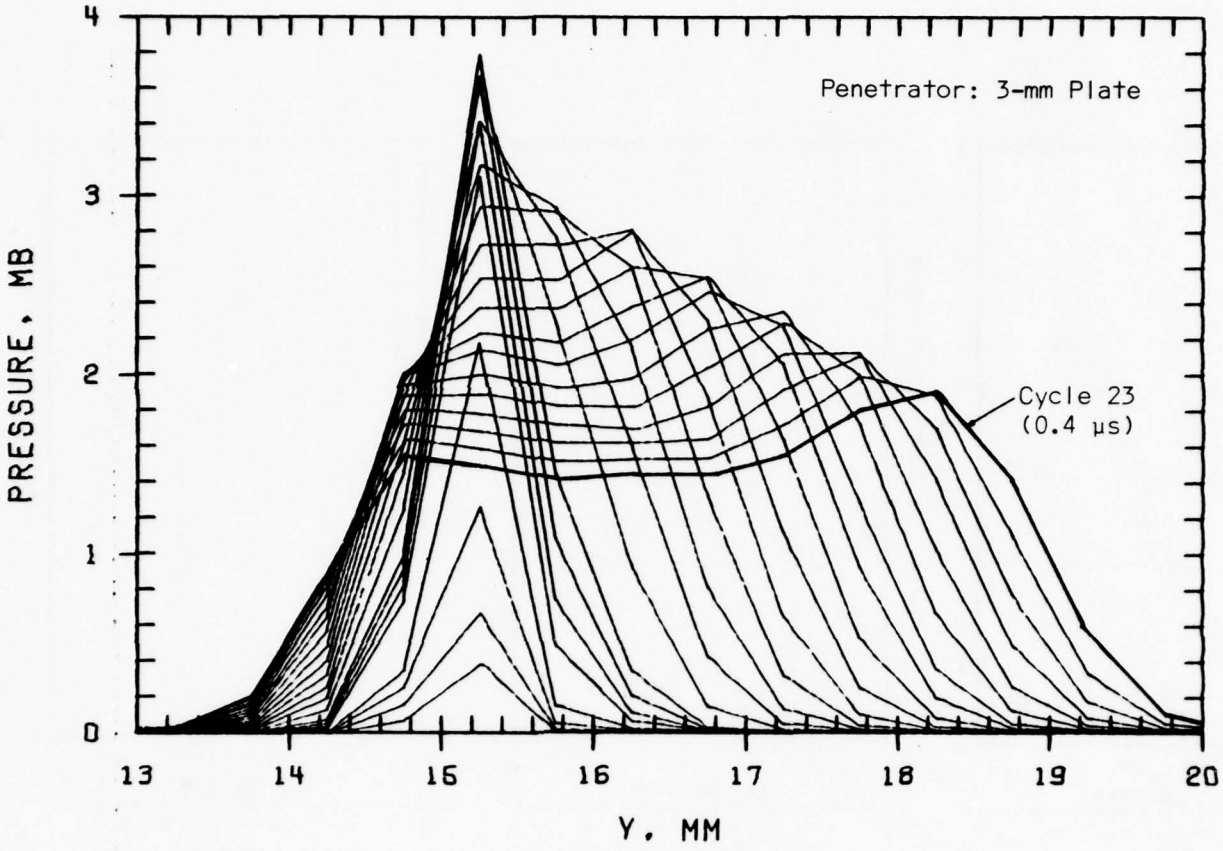

Figure 25. Pressure Profiles along the Y-Axis for the 3-mm Penetrator Plate

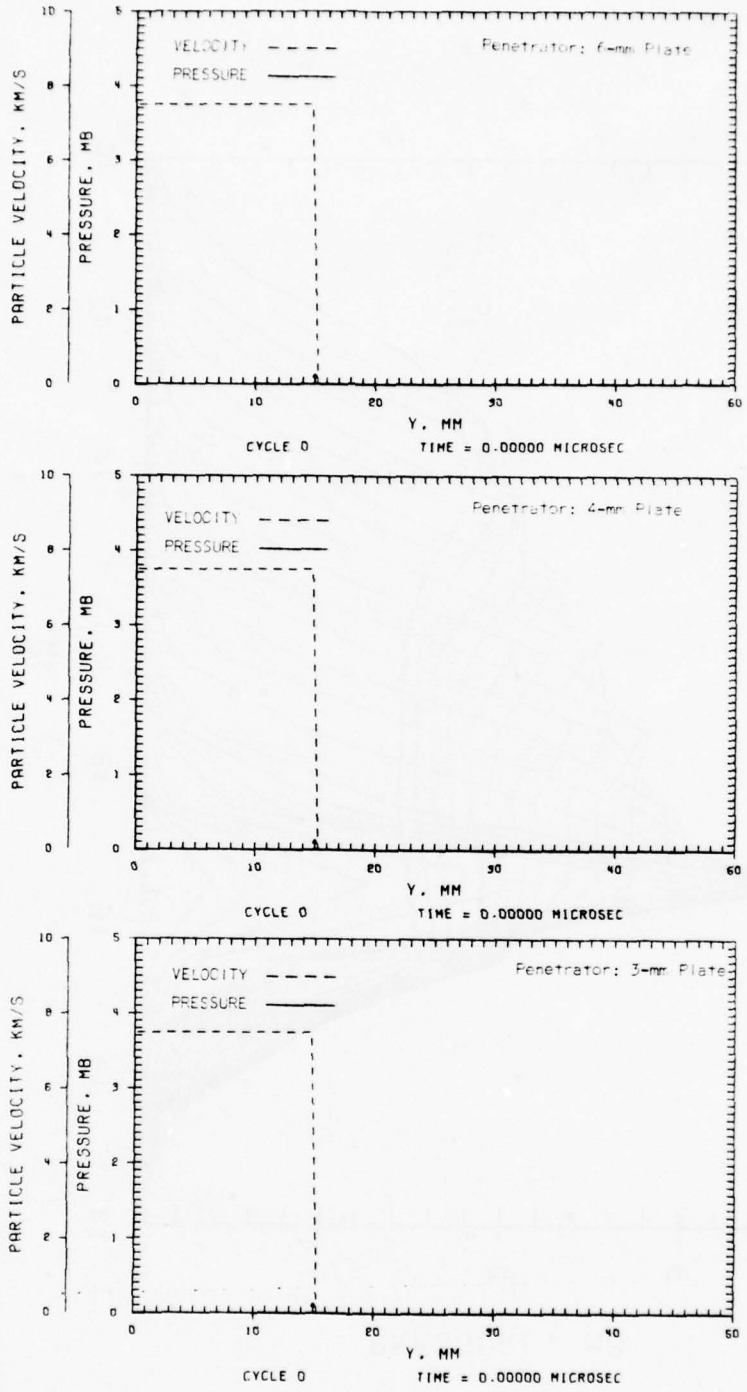

Figure 26. Comparison of Pressure and Particle Velocity Profiles along the Y-Axis

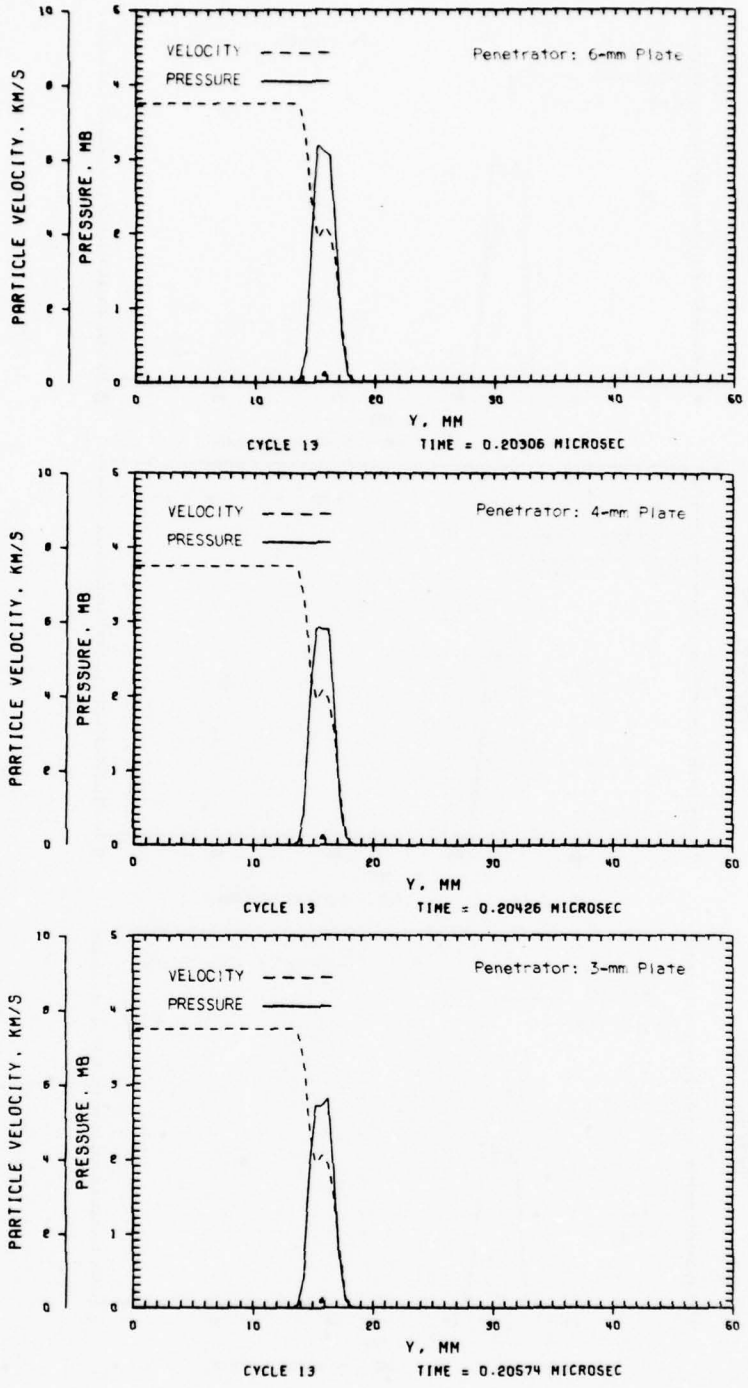

Figure 27. Comparison of Pressure and Particle Velocity Profiles along the Y-Axis

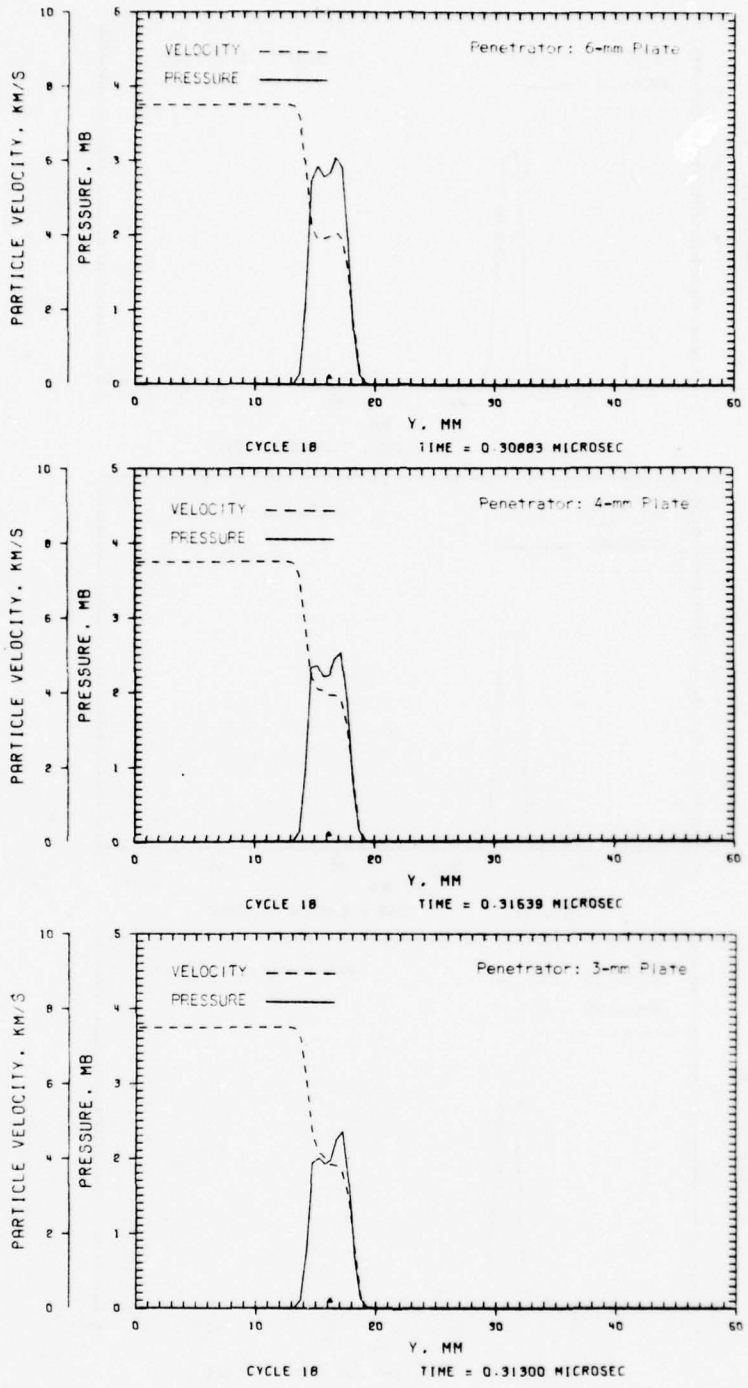

Figure 28. Comparison of Pressure and Particle Velocity Profiles along the Y-Axis

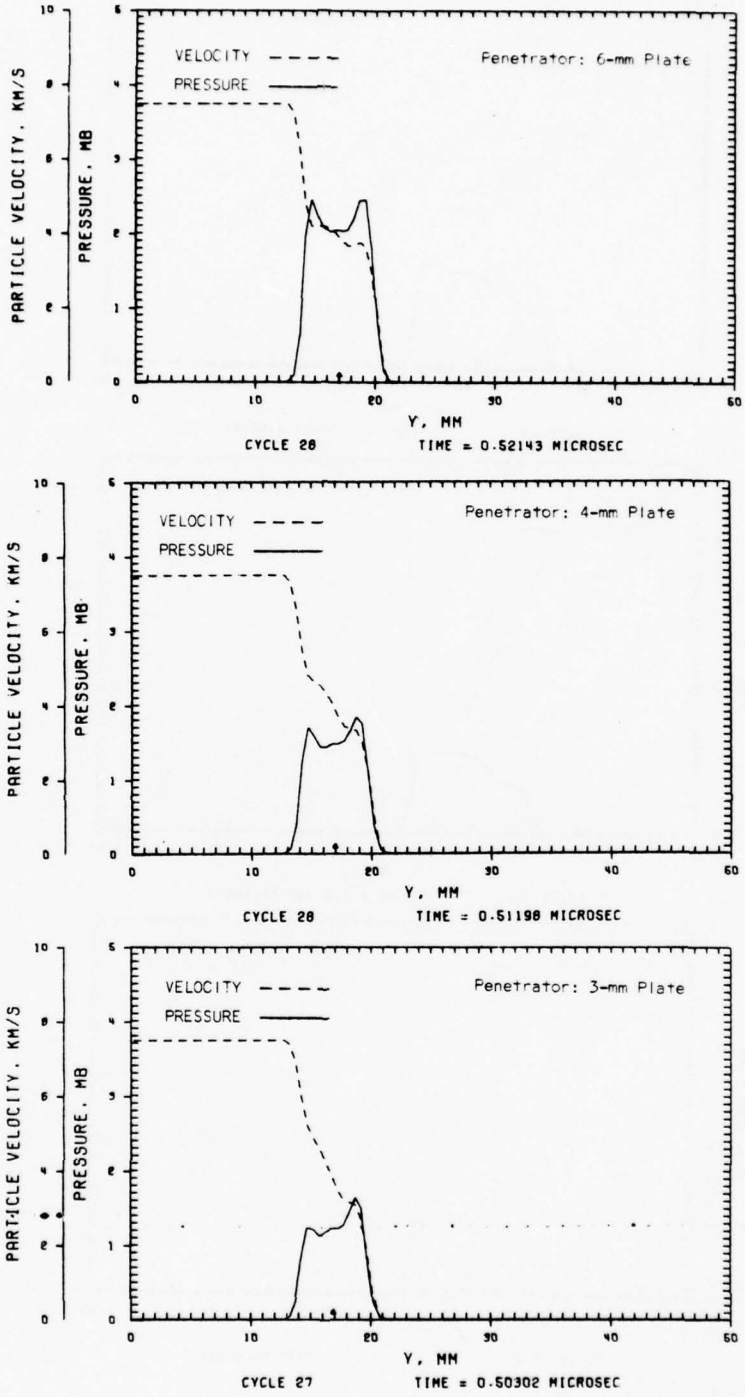

Figure 29. Comparison of Pressure and Particle Velocity Profiles along the Y-Axis

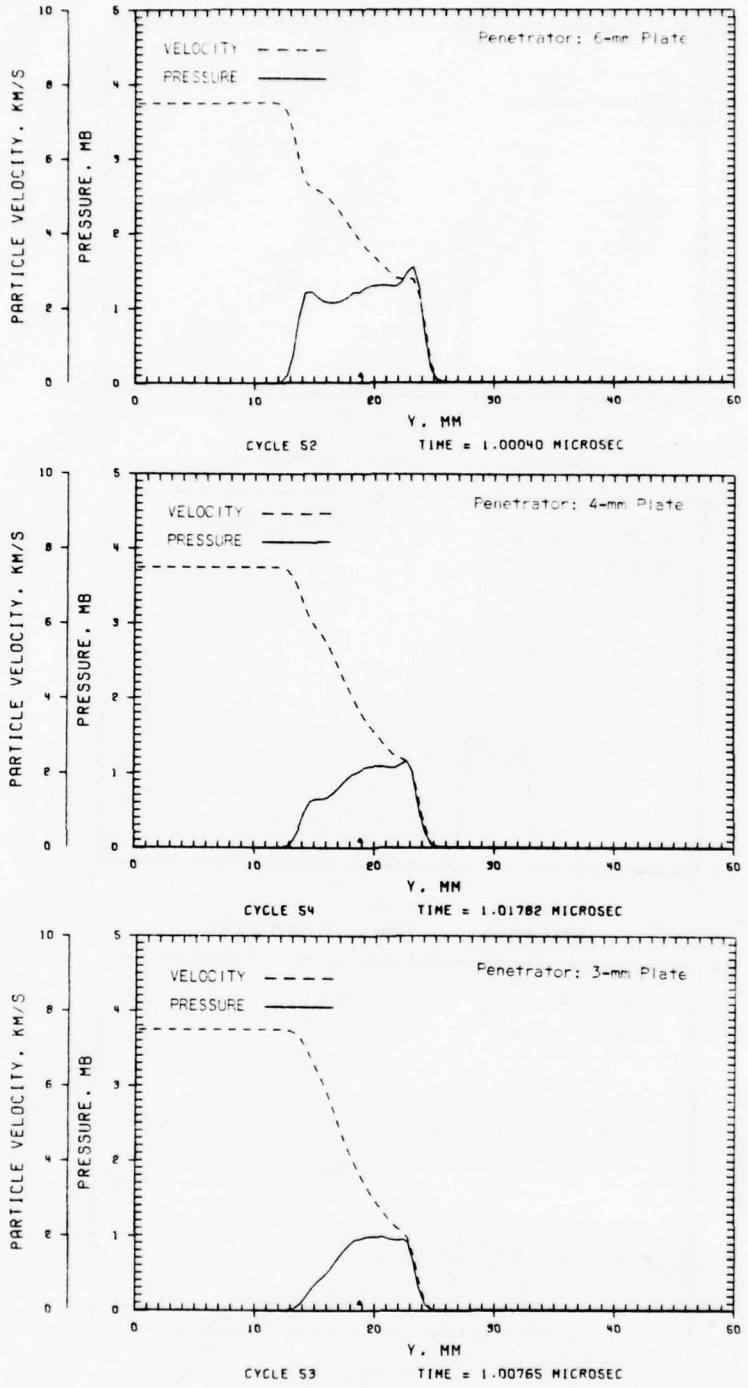

Figure 30. Comparison of Pressure and Particle Velocity Profiles along the Y-Axis

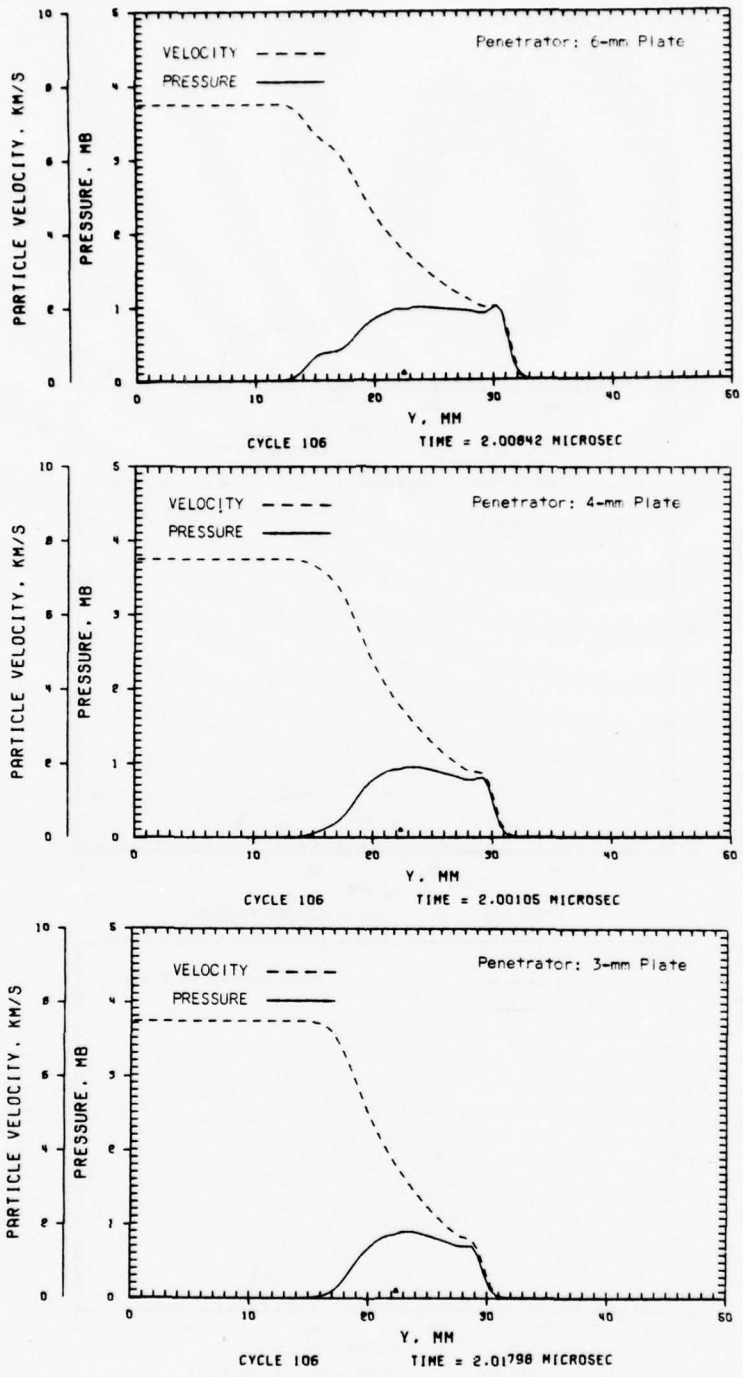

Figure 31. Comparison of Pressure and Particle Velocity Profiles along the Y-Axis

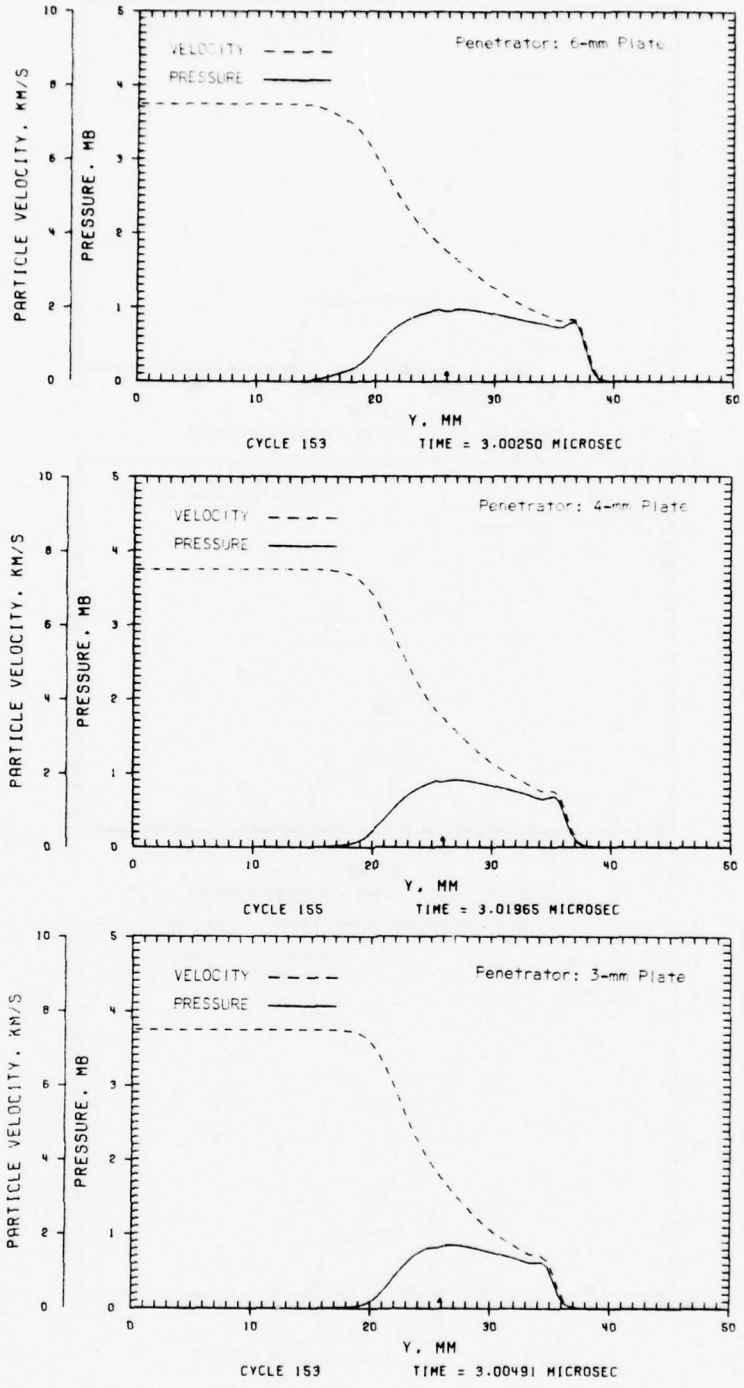

Figure 32. Comparison of Pressure and Particle Velocity Profiles along the Y-Axis

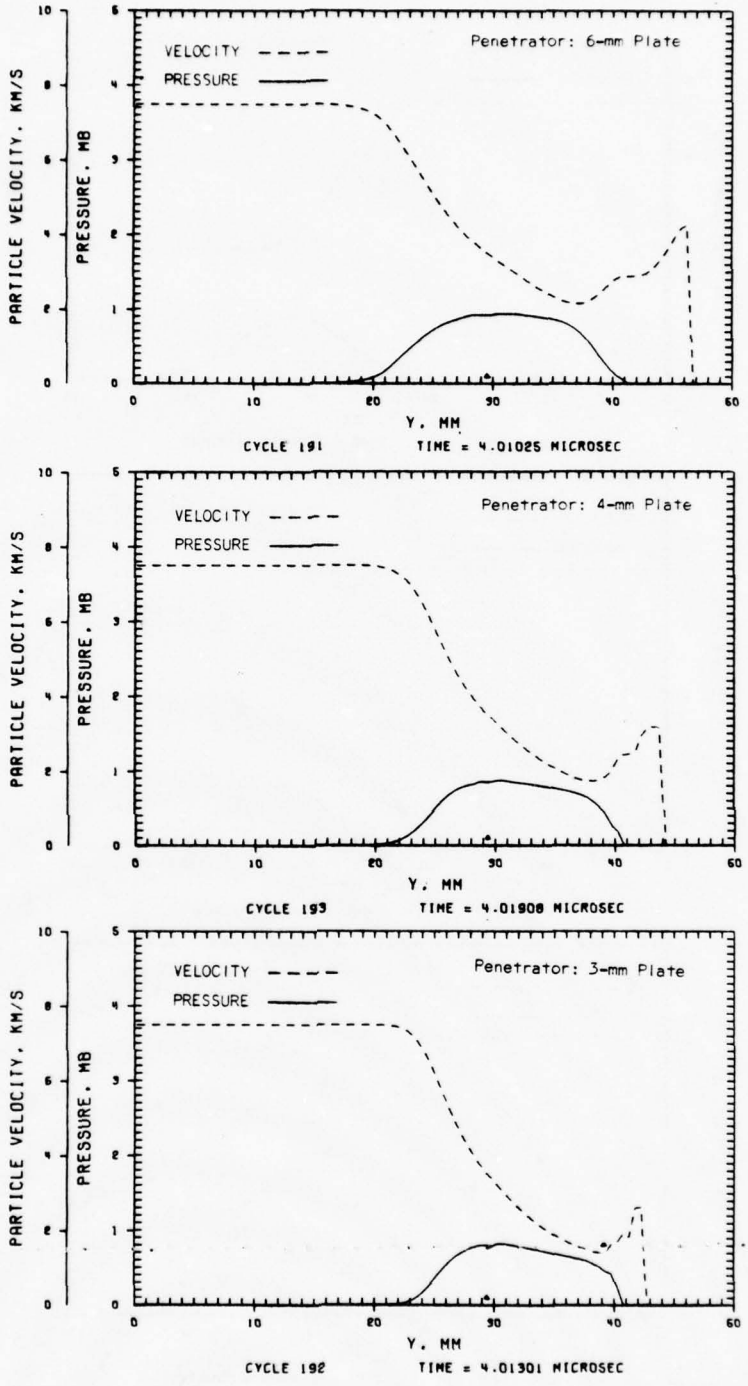

Figure 33. Comparison of Pressure and Particle Velocity Profiles along the Y-Axis

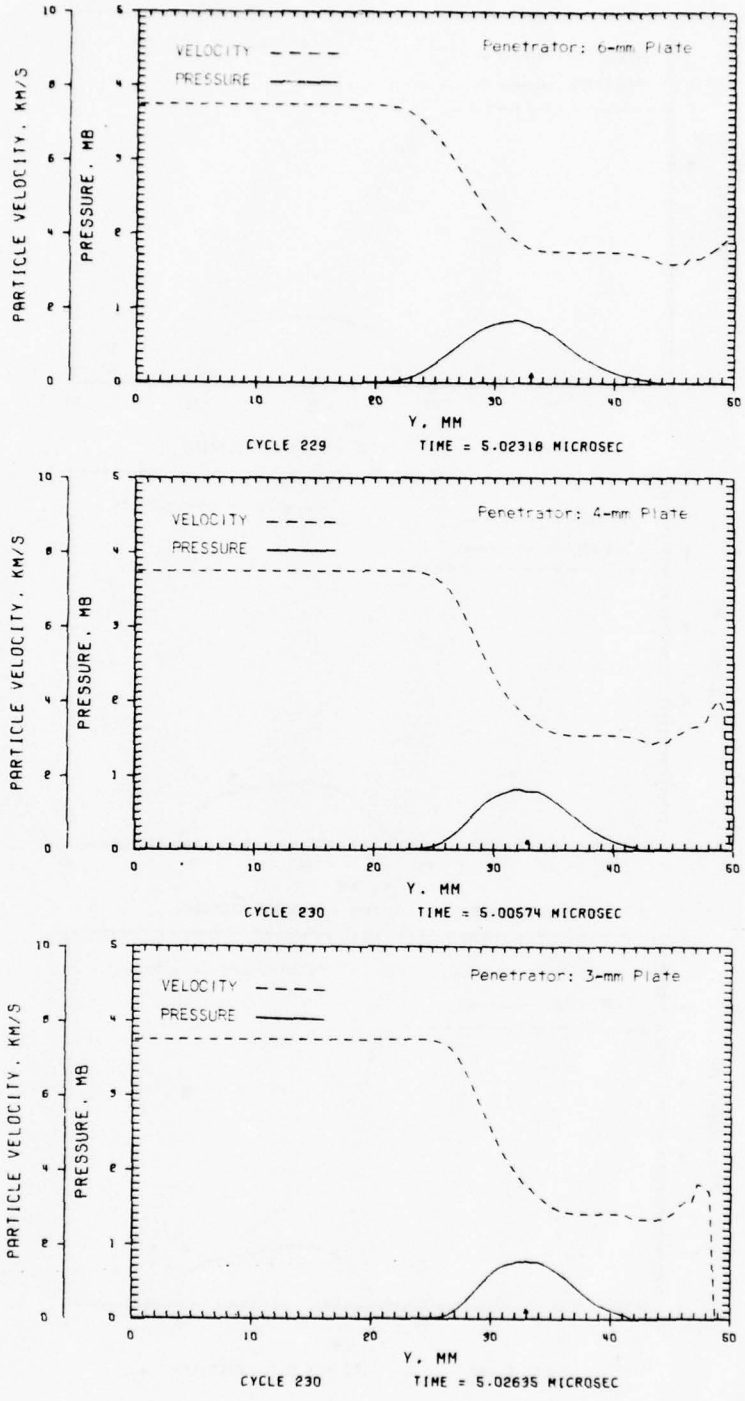

Figure 34. Comparison of Pressure and Particle Velocity Profiles along the Y-Axis

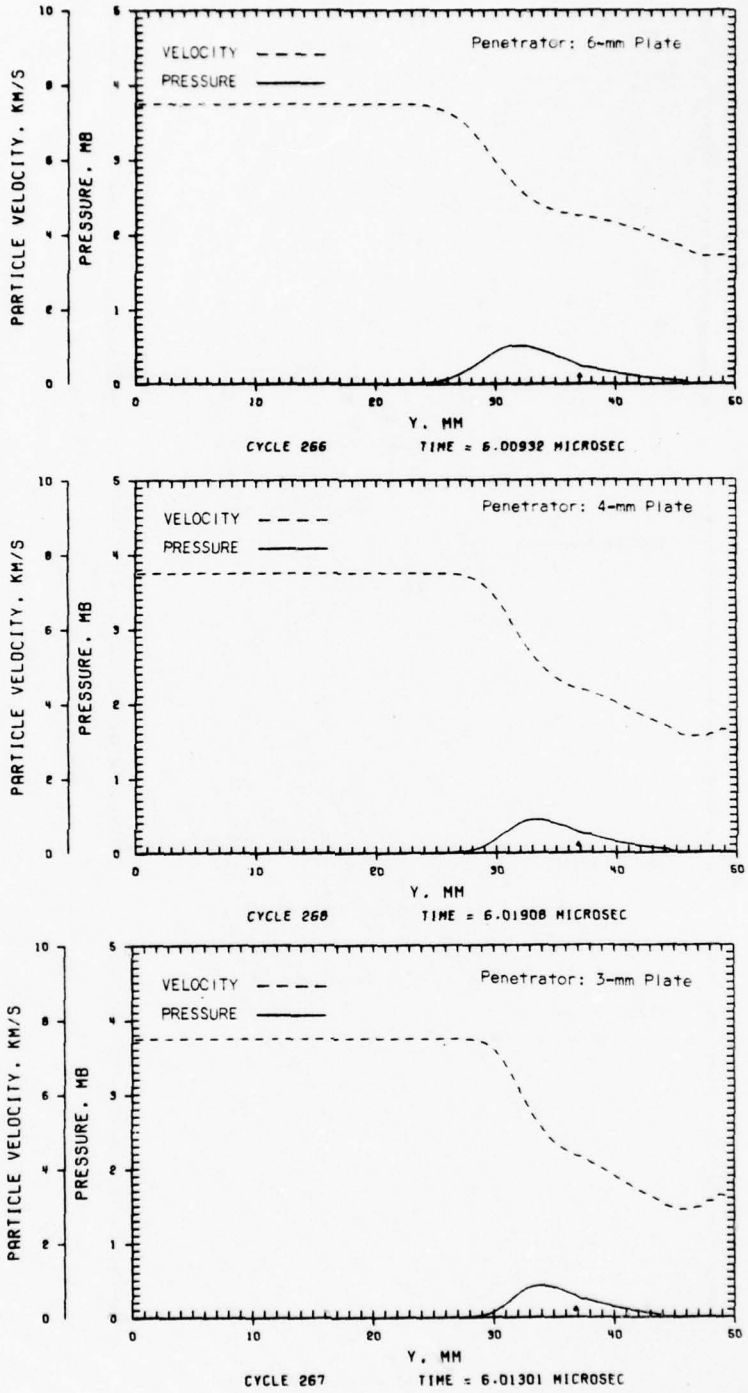

Figure 35. Comparison of Pressure and Particle Velocity Profiles along the Y-Axis

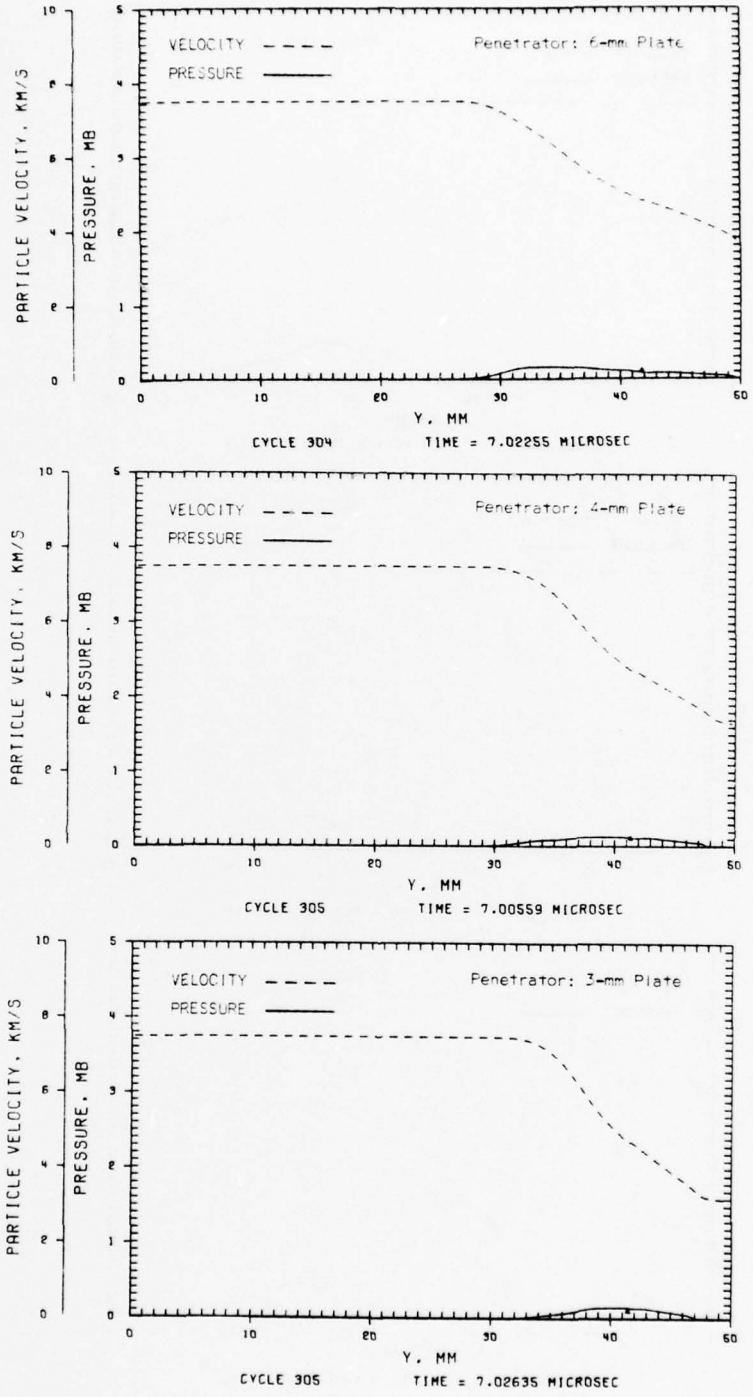

Figure 36. Comparison of Pressure and Particle Velocity Profiles along the Y-Axis

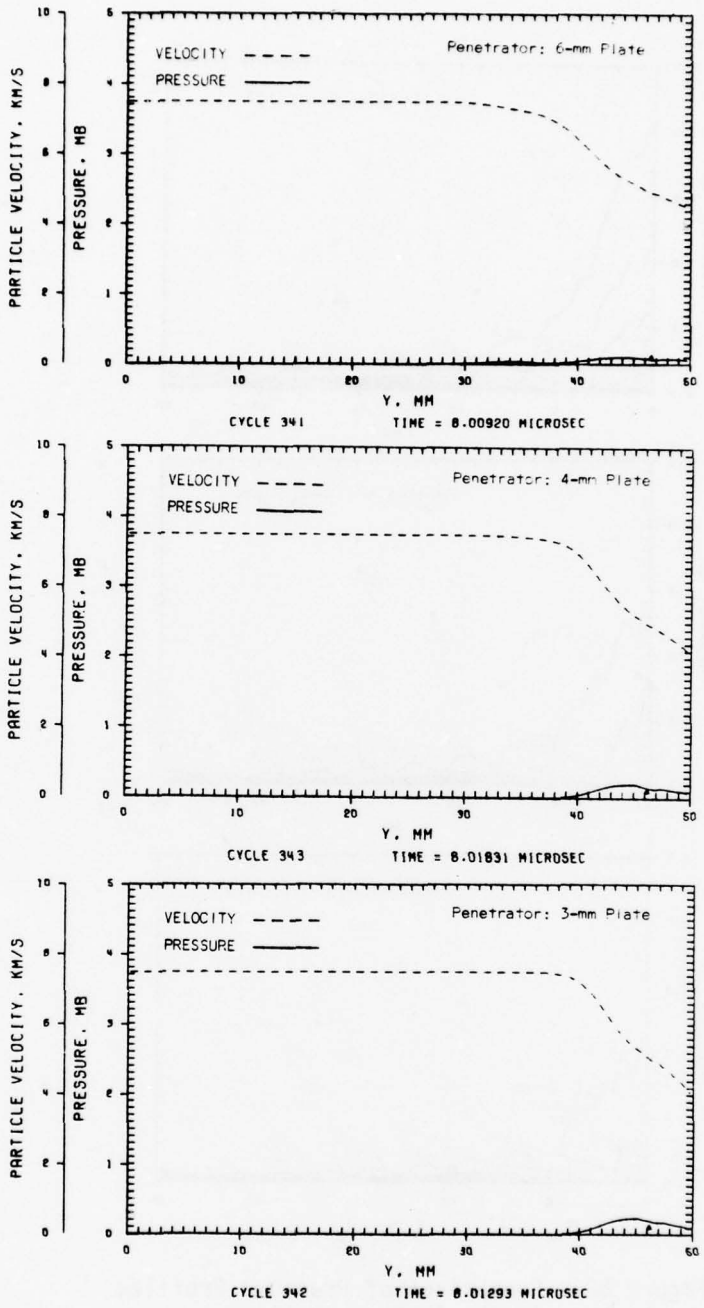

Figure 37. Comparison of Pressure and Particle Velocity Profiles along the Y-Axis

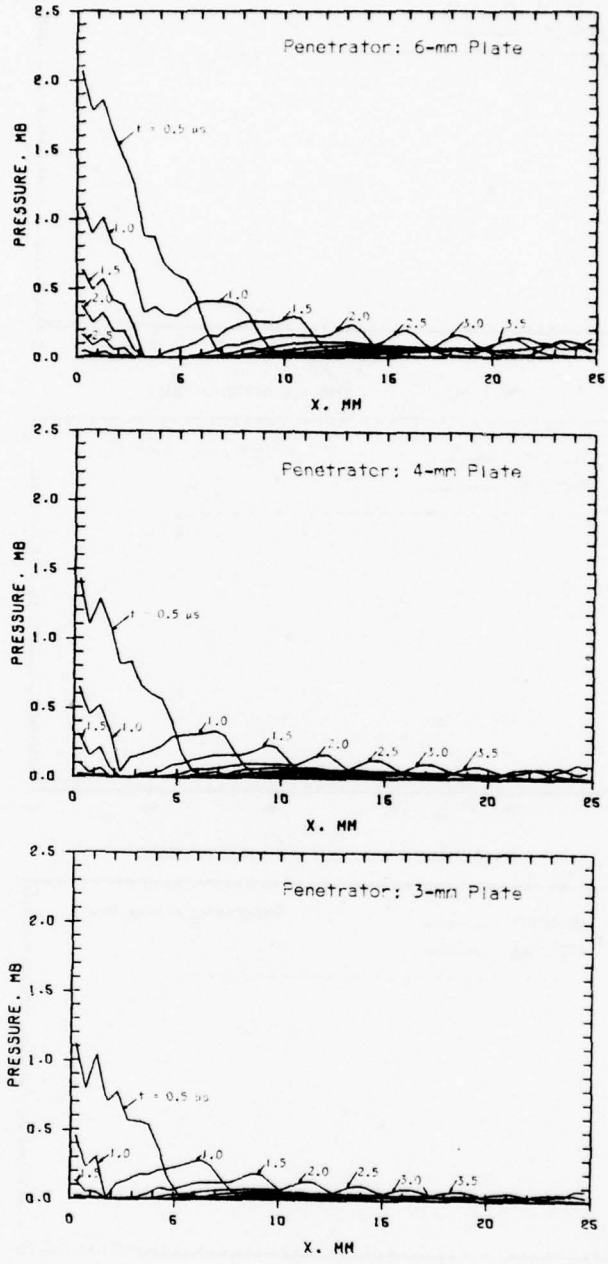

Figure 38. Comparison of Pressure Profiles in the 15.25-mm Y-Plane

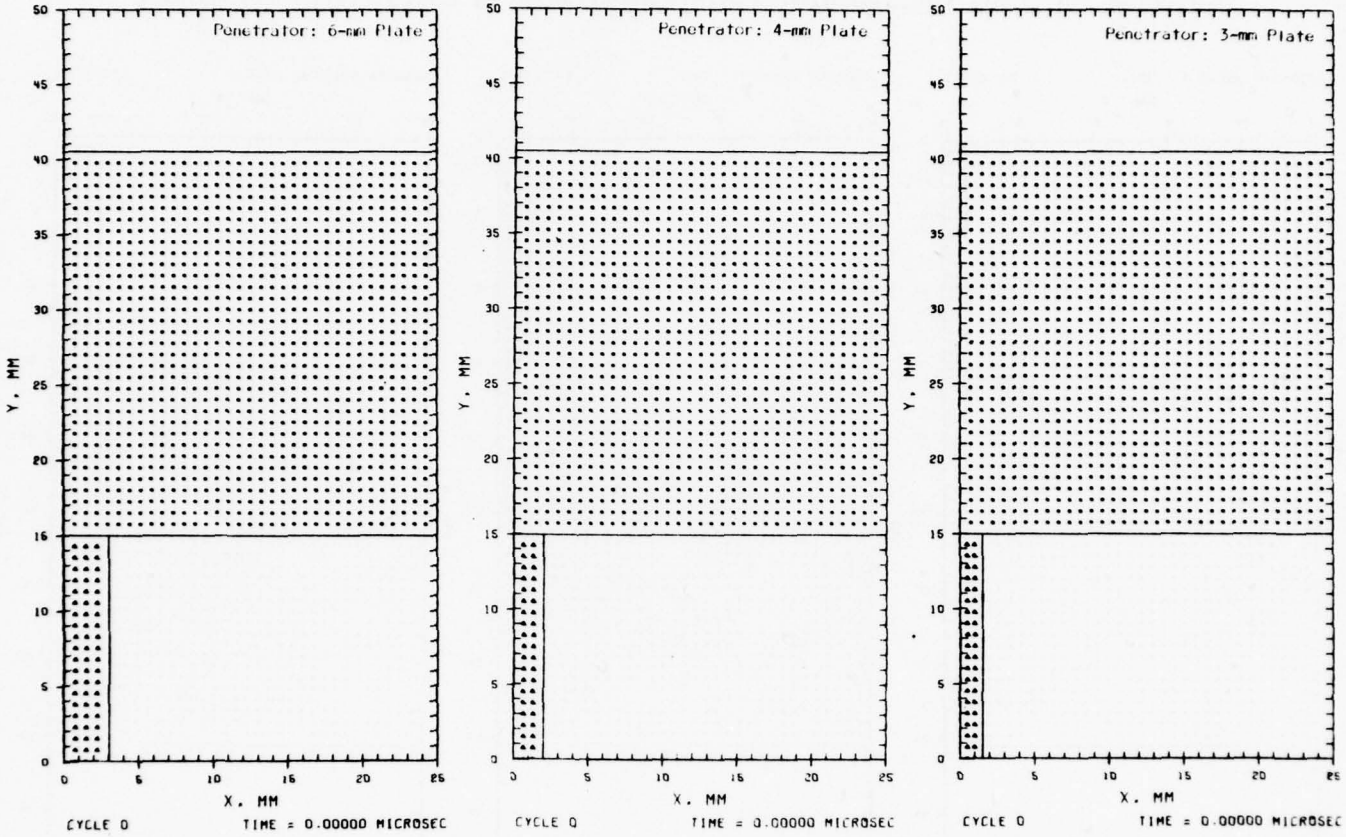

Figure 39. Comparison of Penetrator-Target Deformations for Slab Geometries

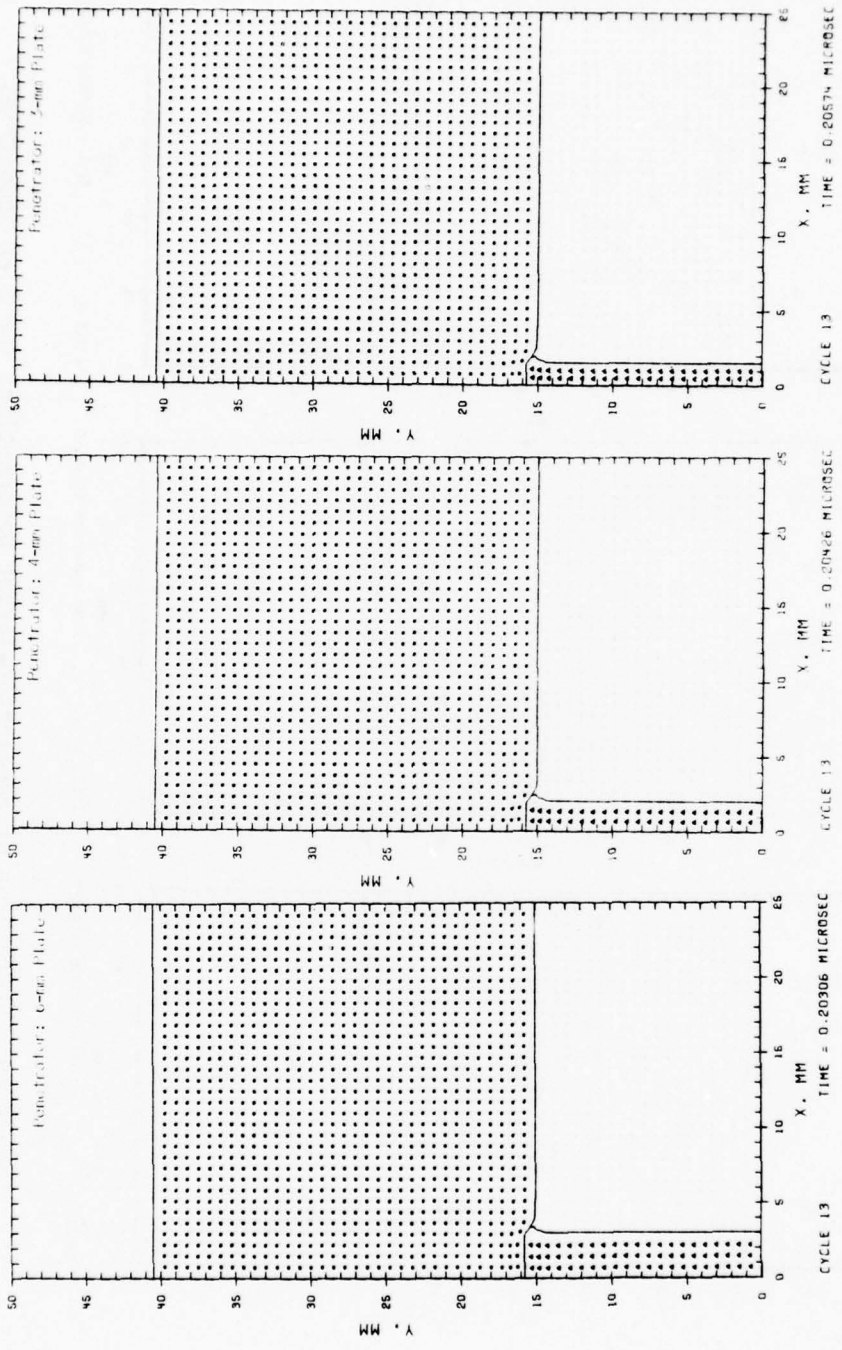

Figure 40. Comparison of Penetrator-Target Deformations for Slab Geometries

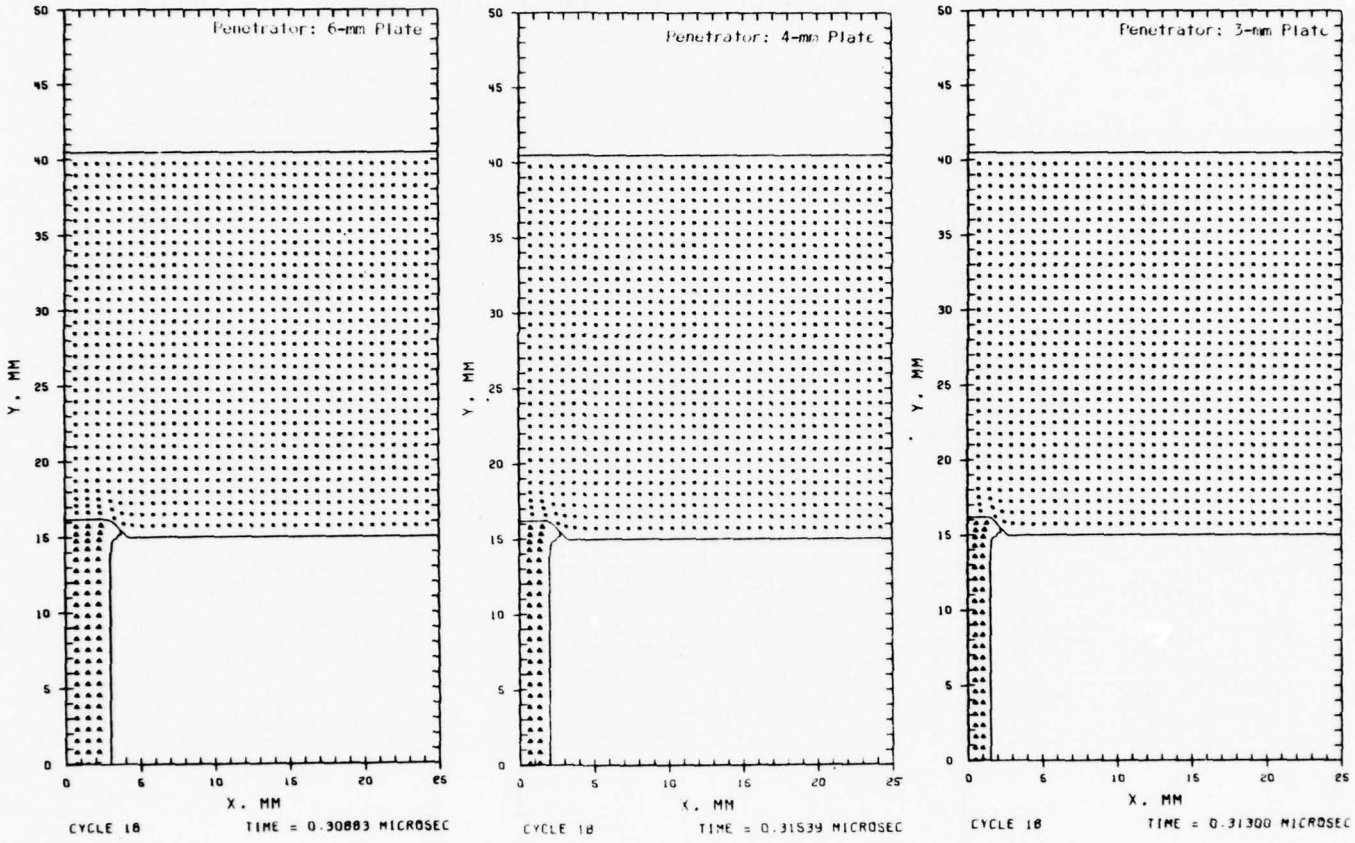

Figure 41. Comparison of Penetrator-Target Deformations for Slab Geometries

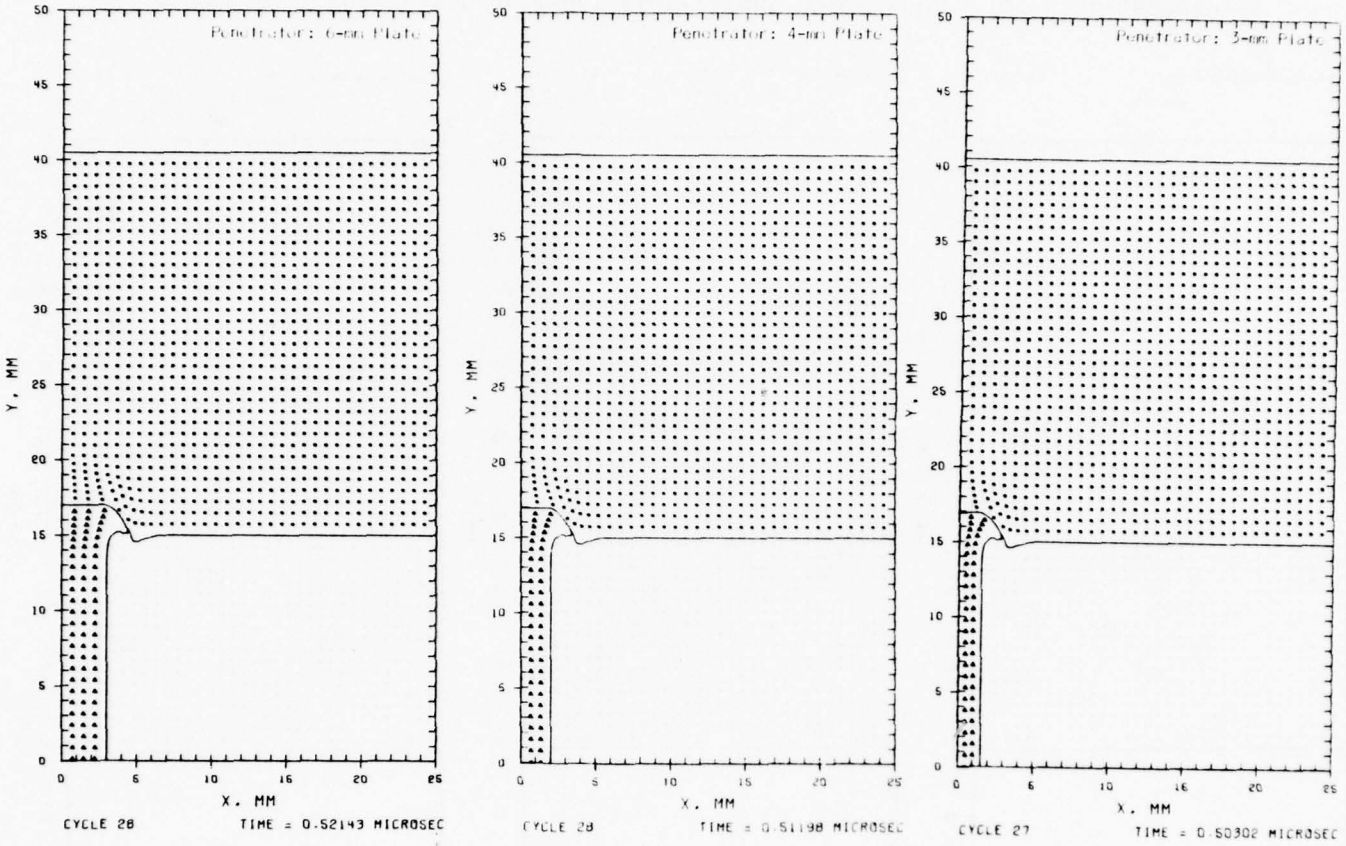

Figure 42. Comparison of Penetrator-Target Deformations for Slab Geometries

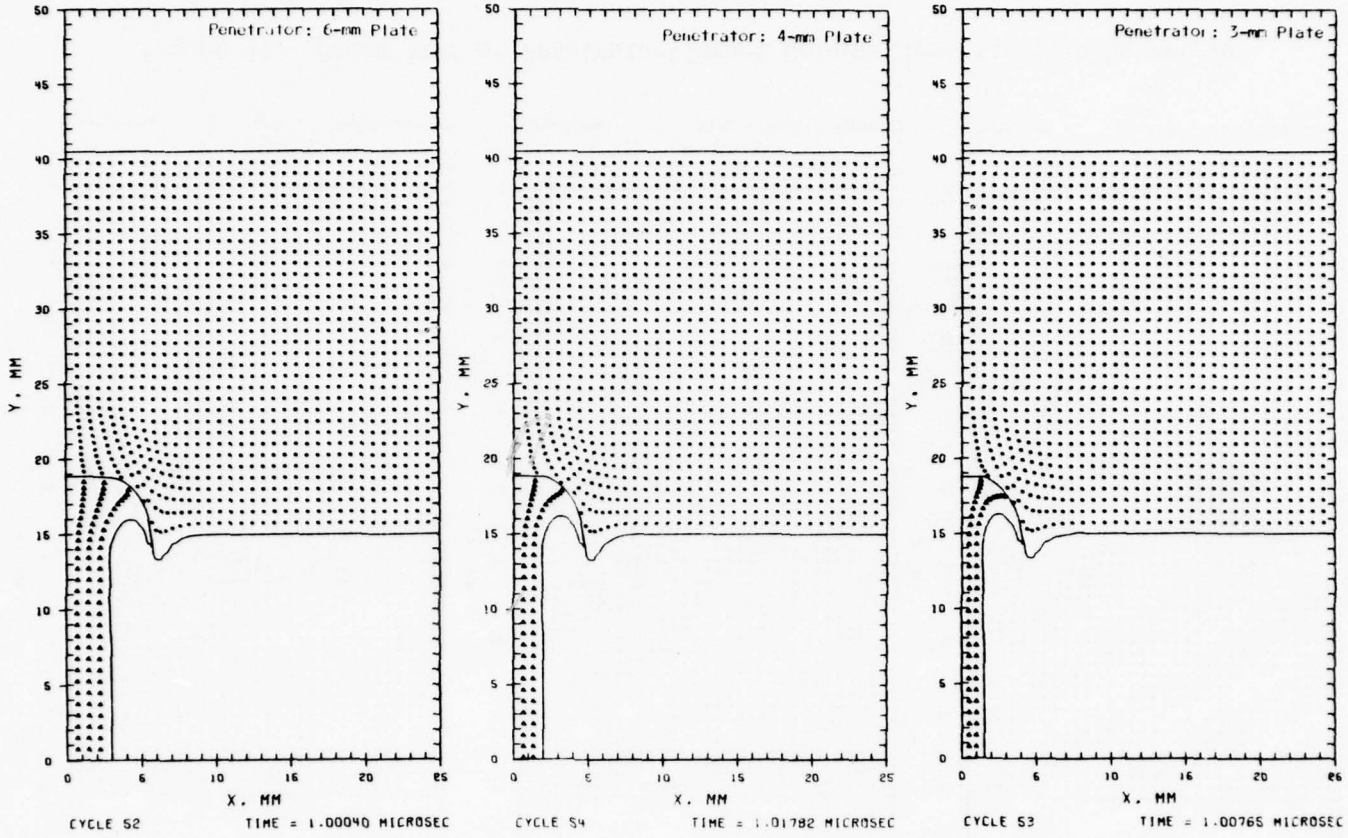

Figure 43. Comparison of Penetrator-Target Deformations for Slab Geometries

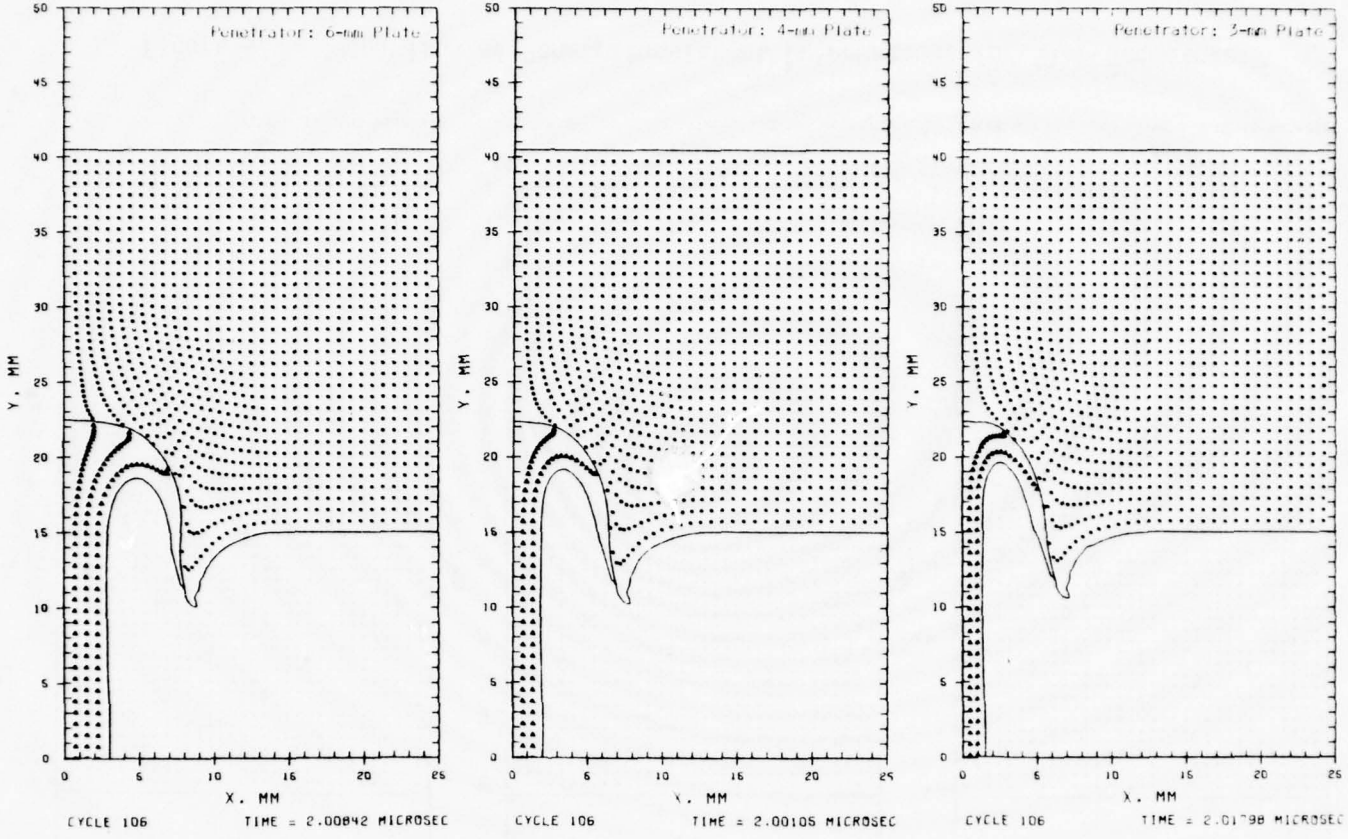

Figure 44. Comparison of Penetrator-Target Deformations for Slab Geometries

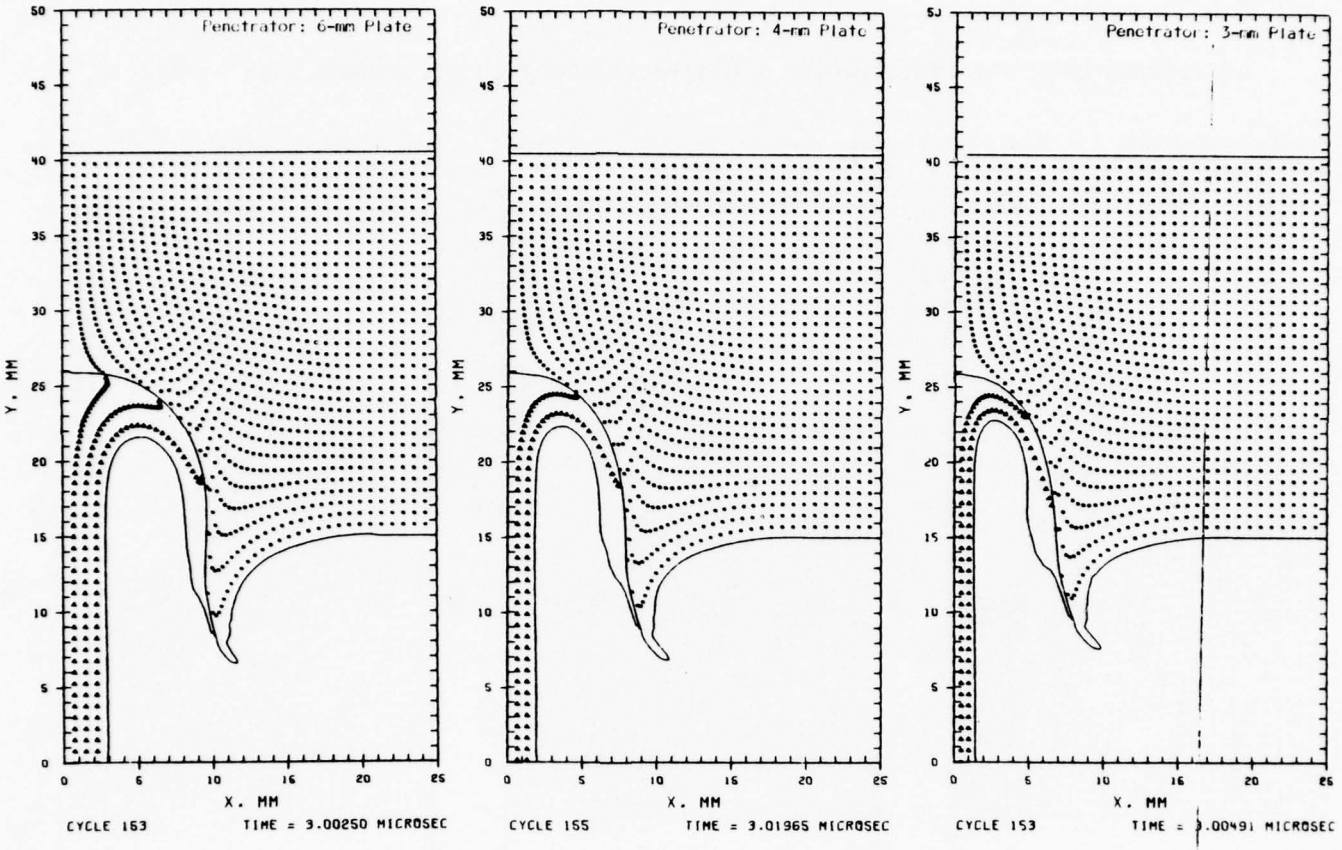

Figure 45. Comparison of Penetrator-Target Deformations for Slab Geometries

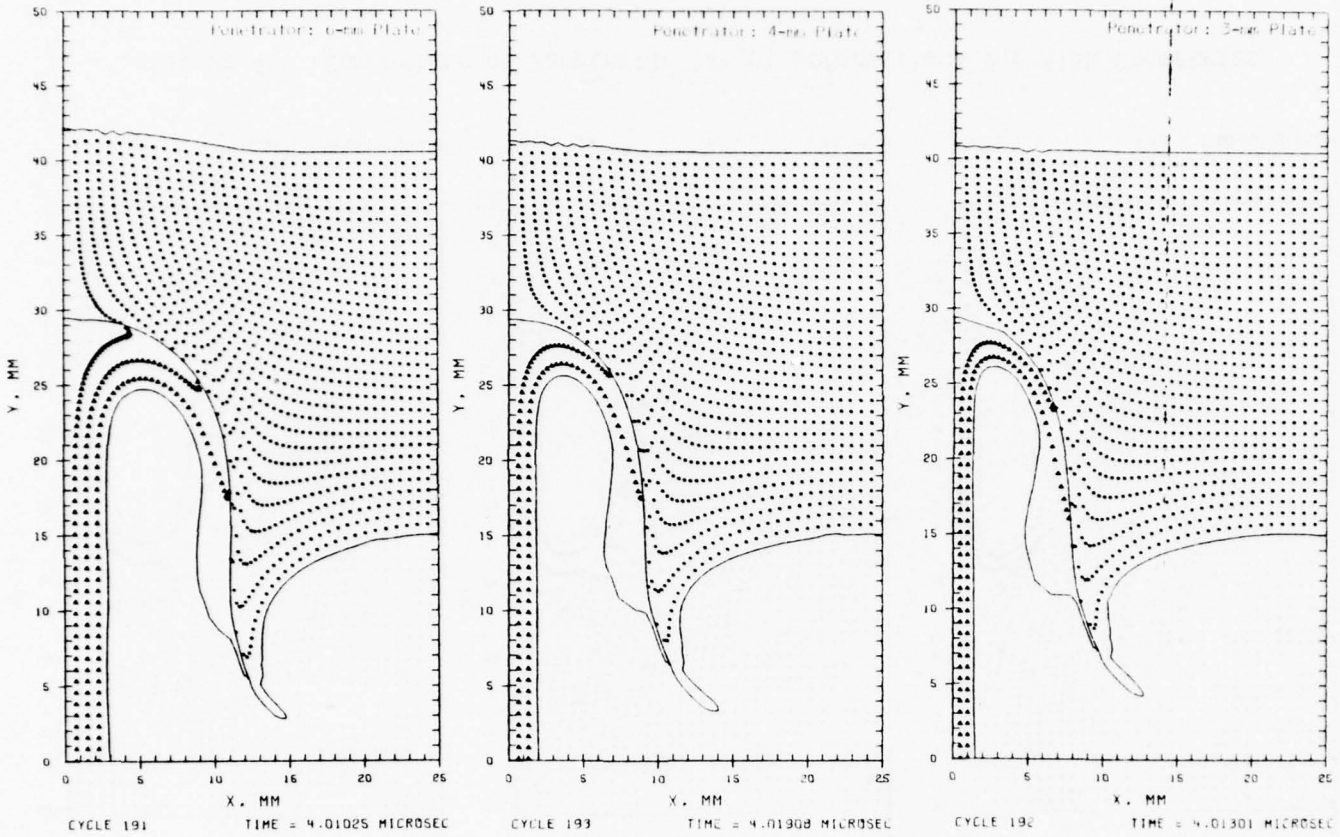

Figure 46. Comparison of Penetrator-Target Deformations for Slab Geometries

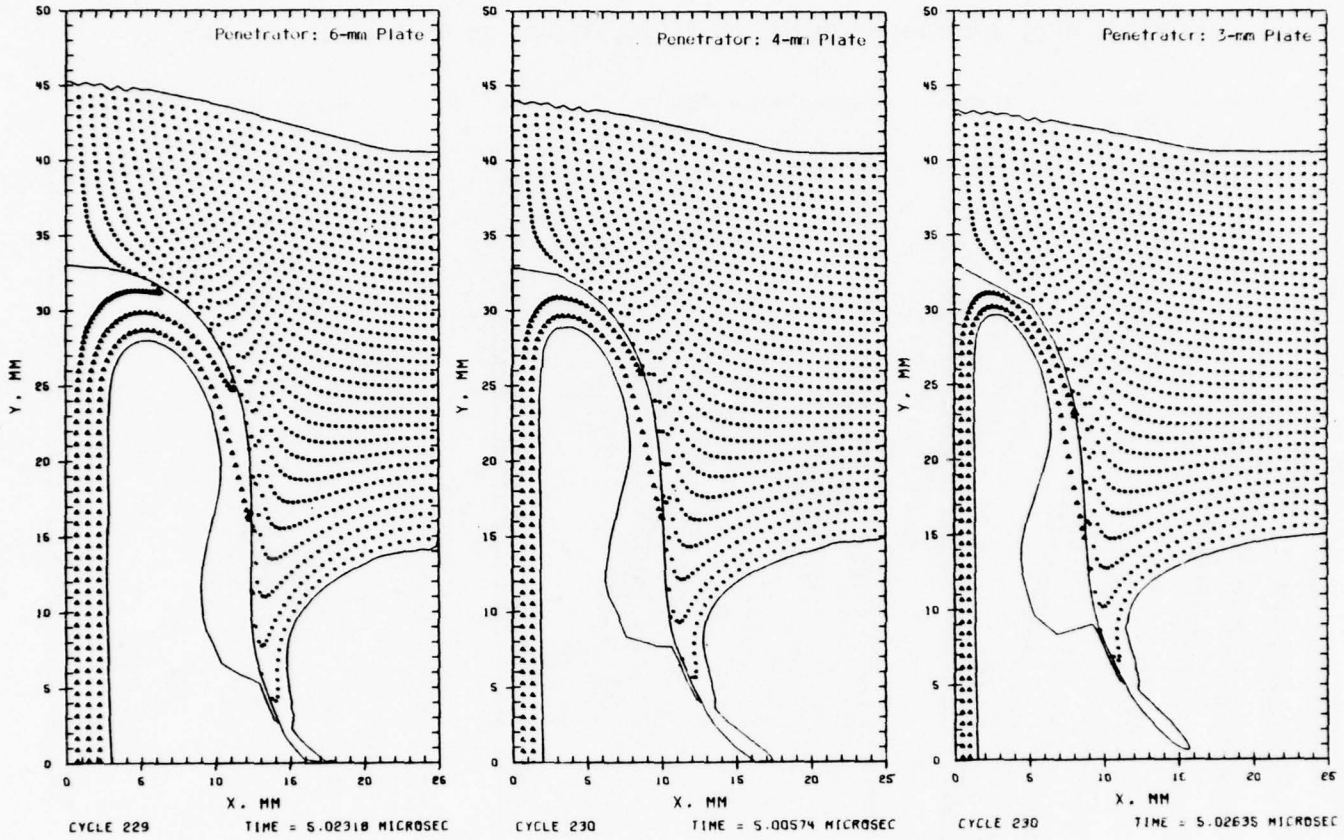

Figure 47. Comparison of Penetrator-Target Deformations for Slab Geometries

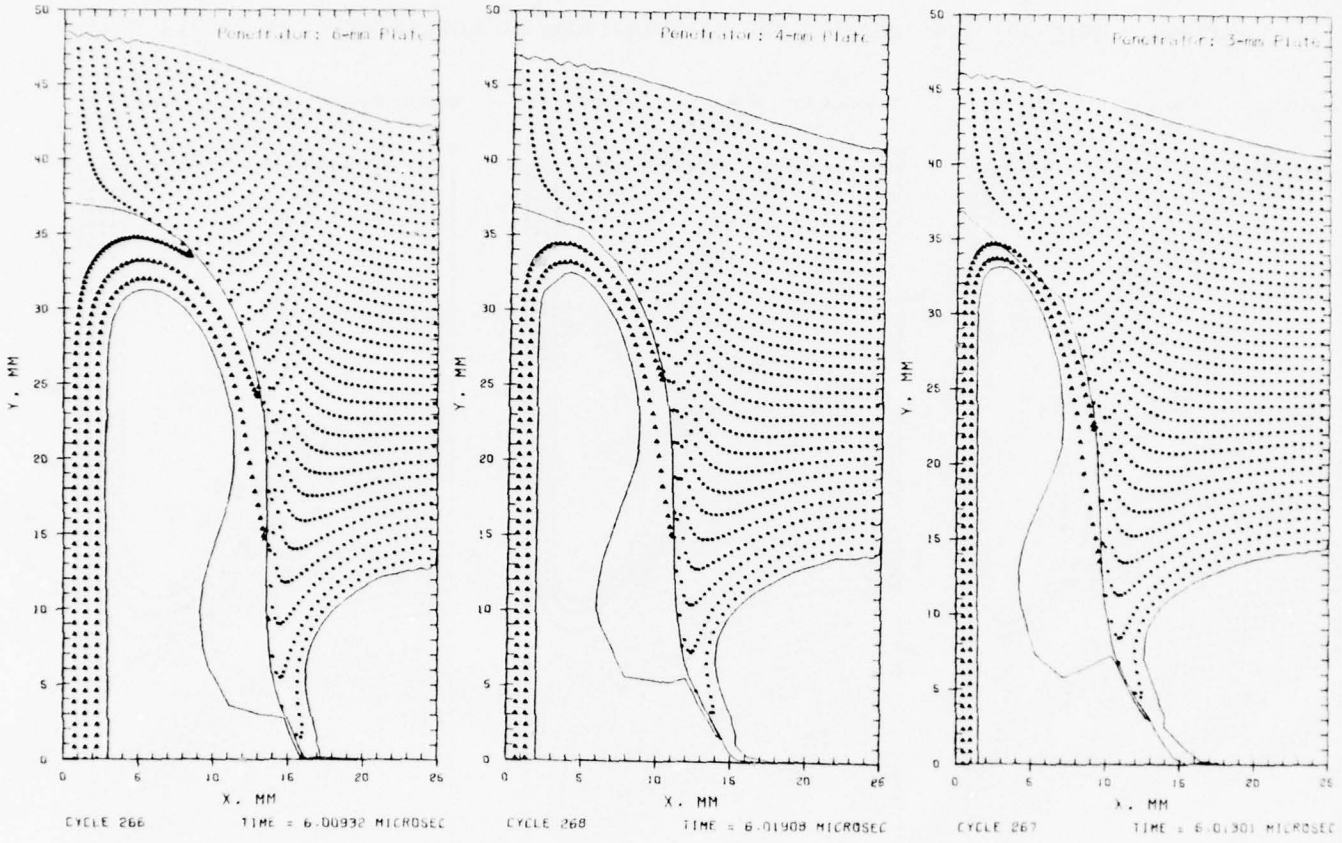

Figure 48. Comparison of Penetrator-Target Deformations for Slab Geometries

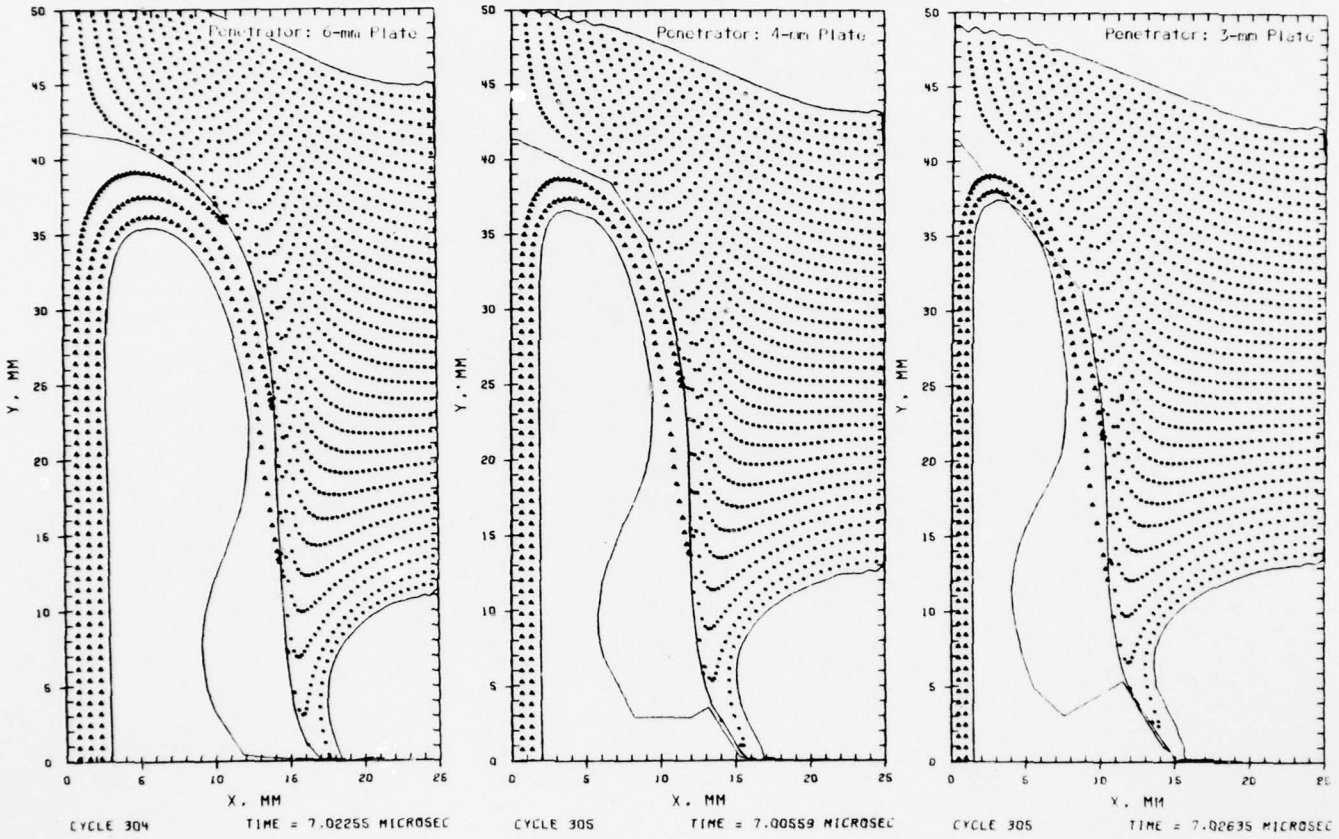

Figure 49. Comparison of Penetrator-Target Deformations for Slab Geometries

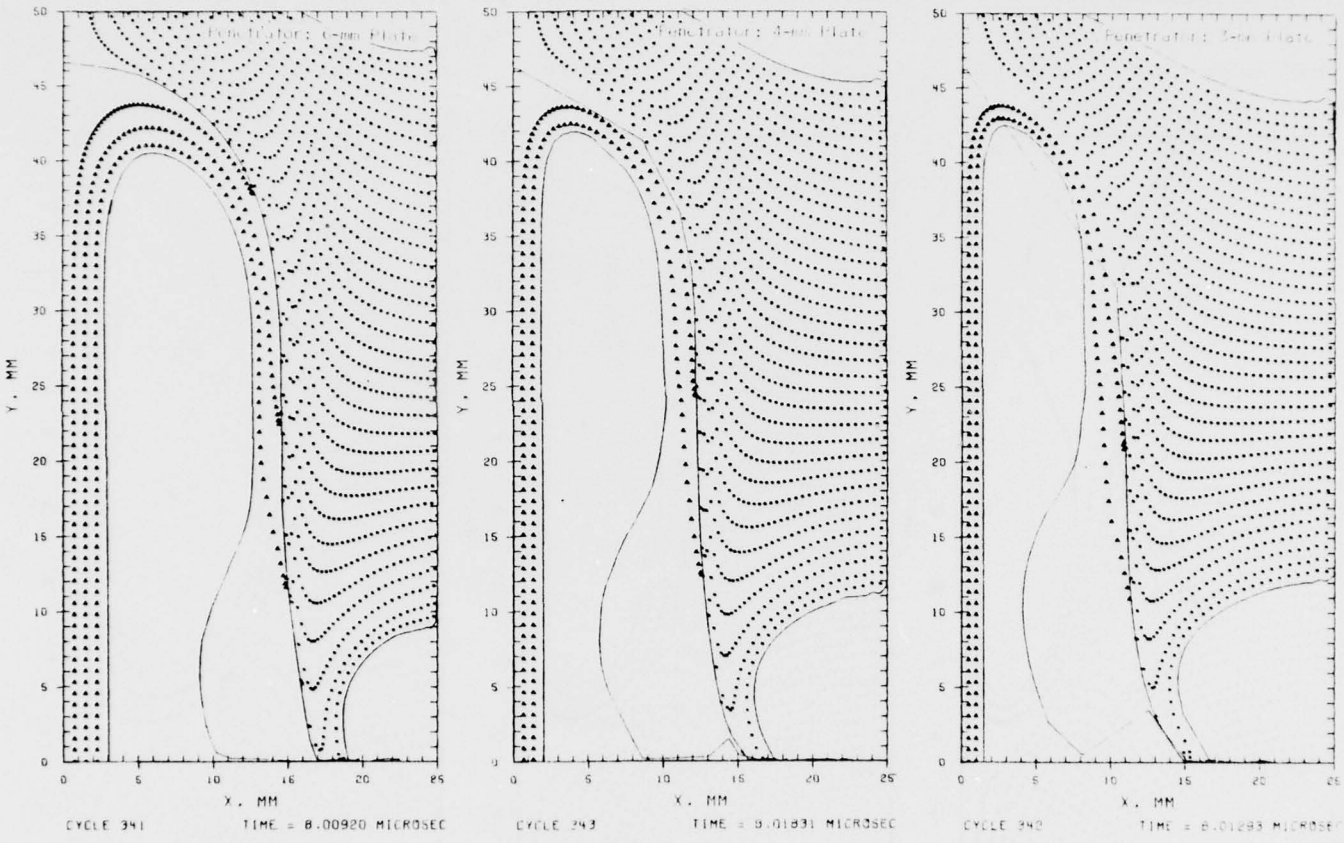

Figure 50. Comparison of Penetrator-Target Deformations for Slab Geometries

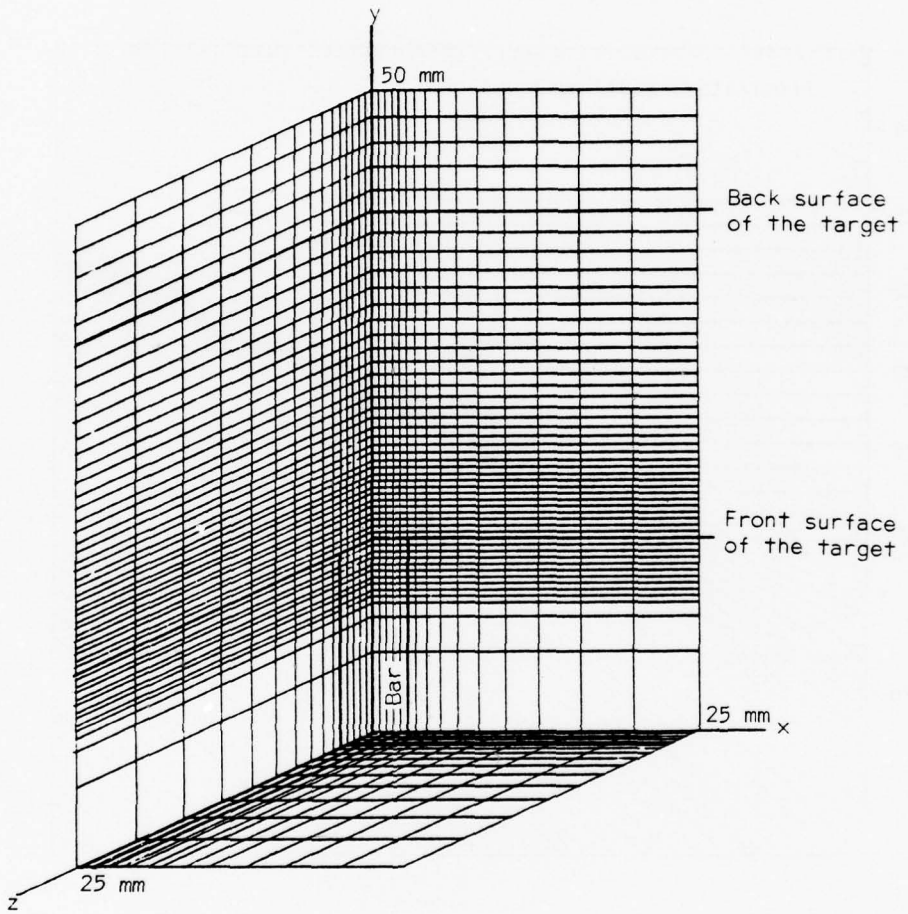

Figure 51. Three-Dimensional Computational Grid

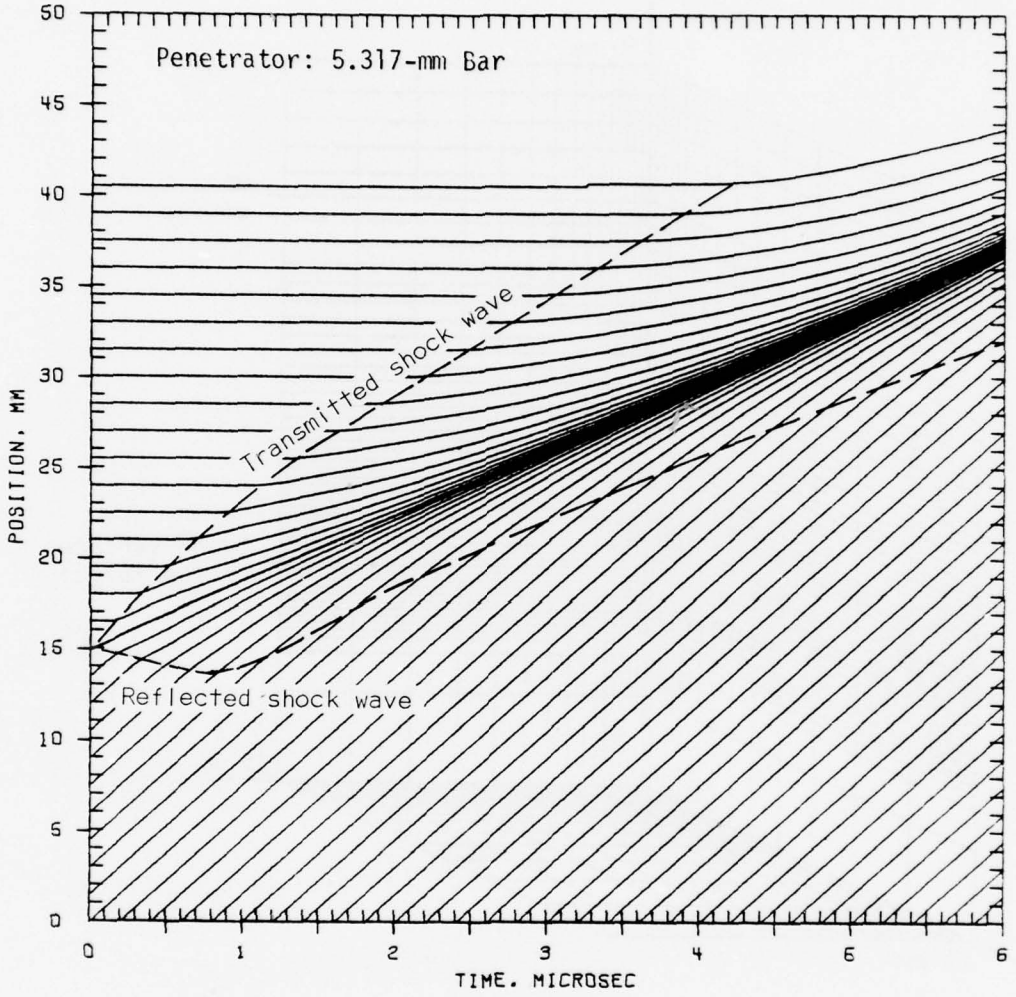

Figure 52. Motion of Tracer Particles along the Y-Axis

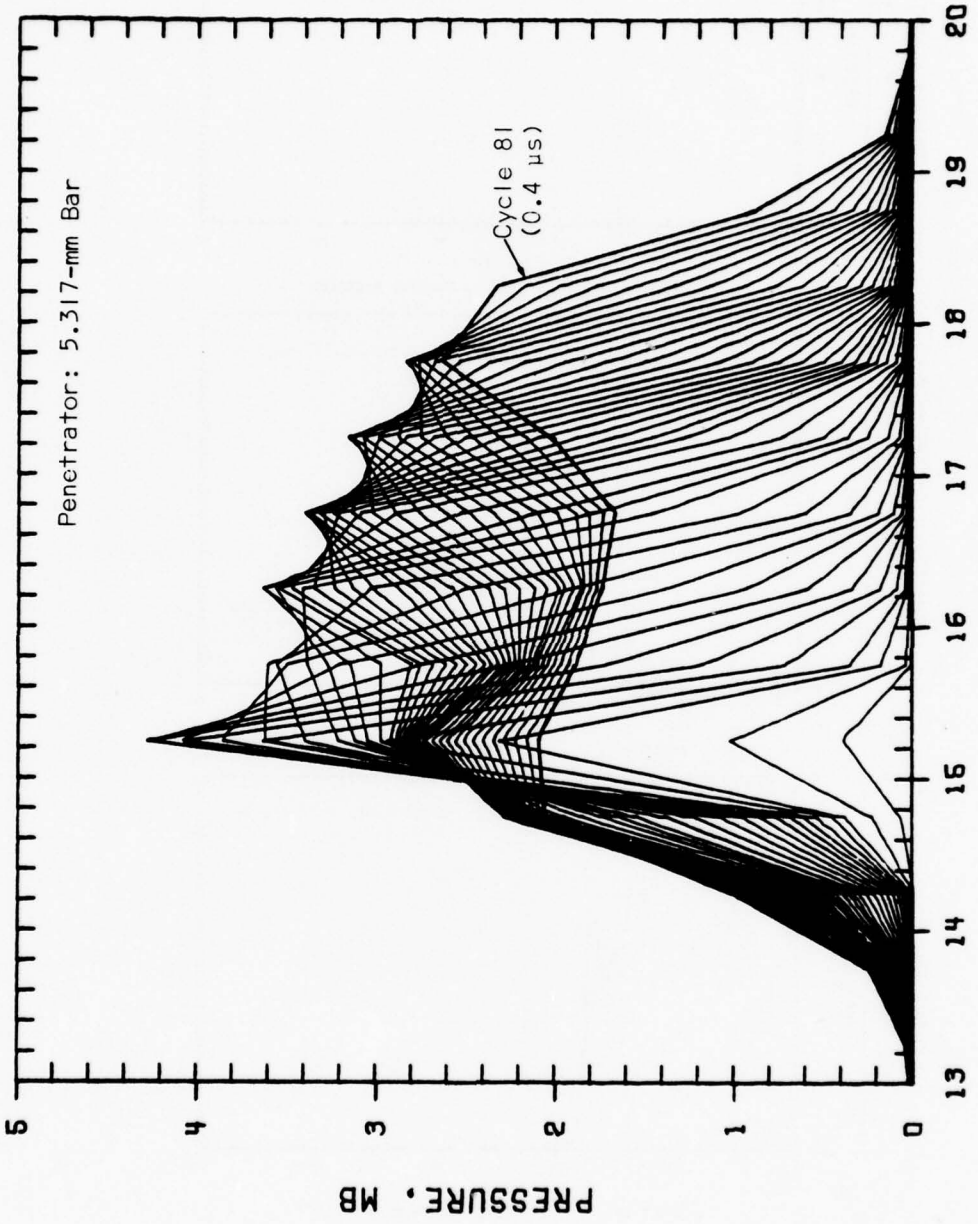

Figure 53. Pressure Profiles along the Y-Axis

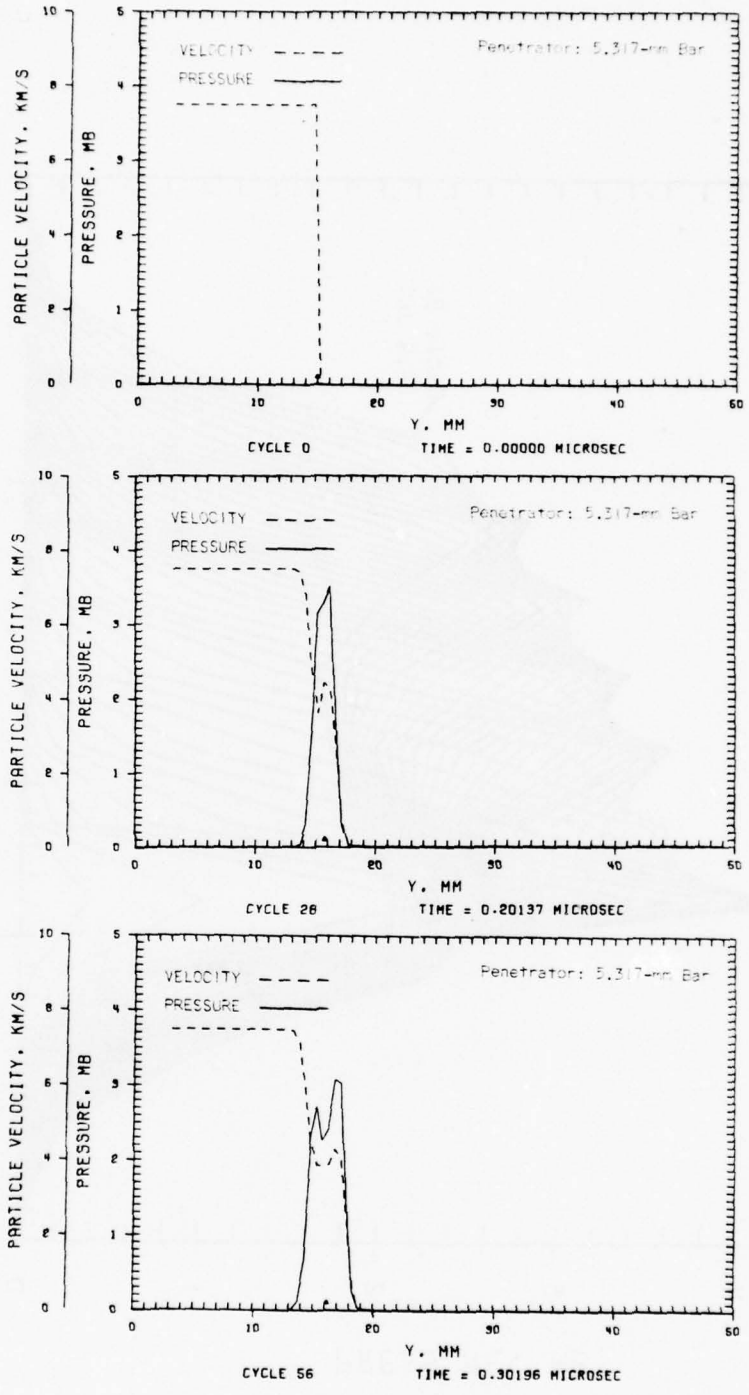

Figure 54. Pressure and Particle Velocity Profiles along the Y-Axis

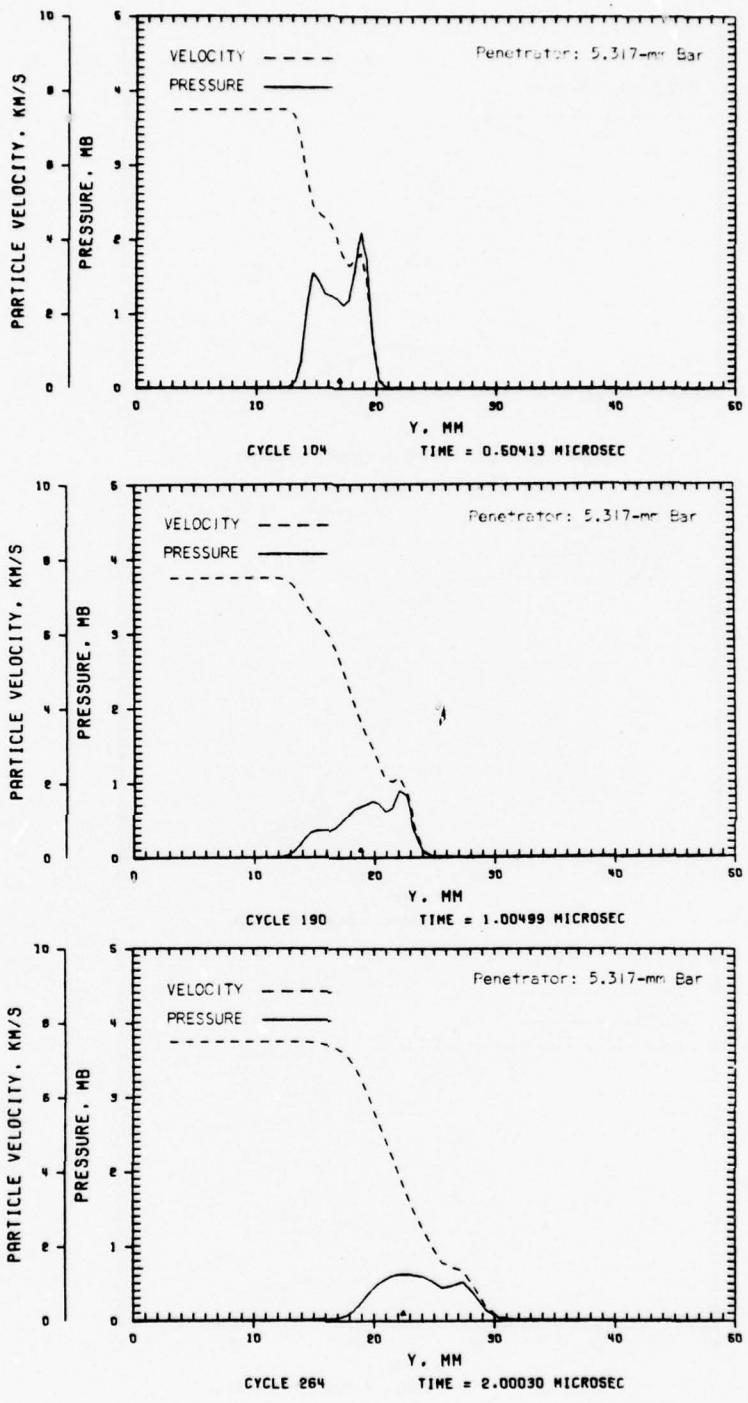

Figure 55. Pressure and Particle Velocity Profiles along the Y-Axis

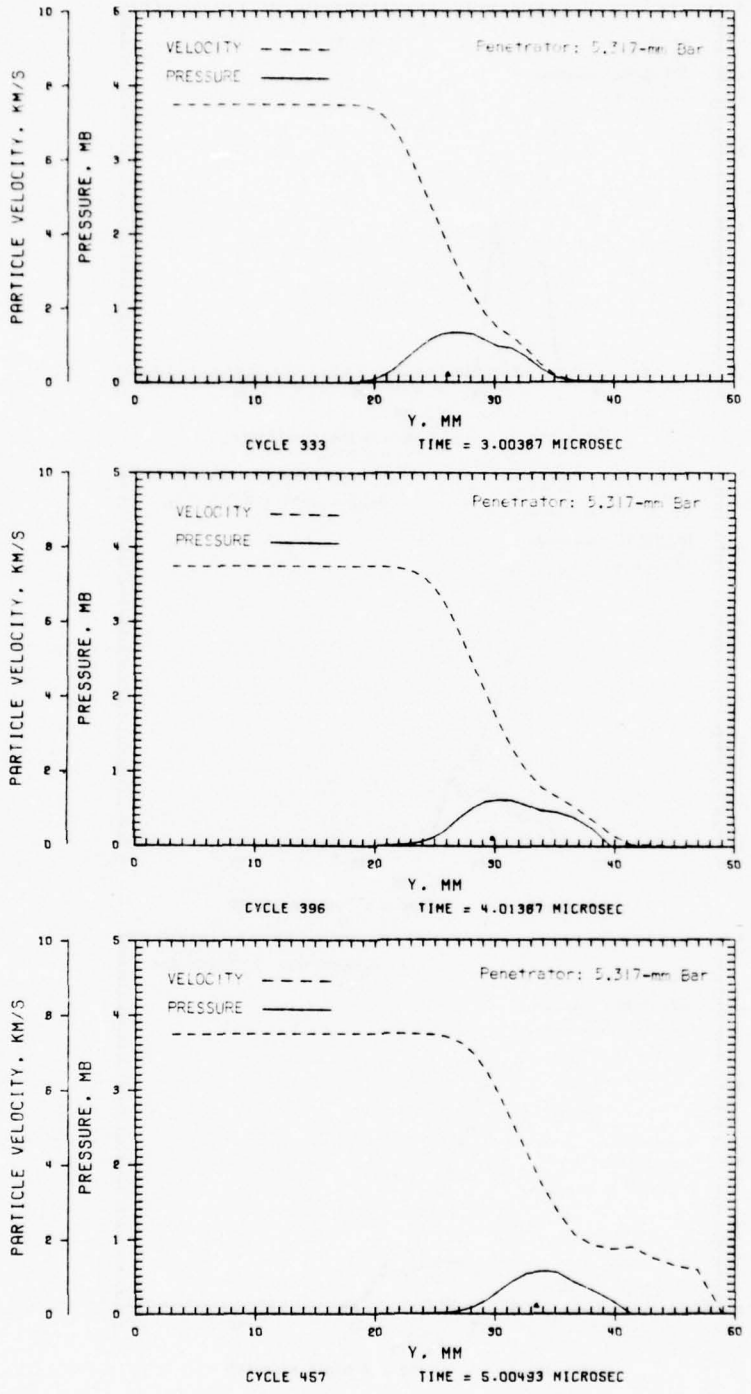

Figure 56. Pressure and Particle Velocity Profiles along the Y-Axis

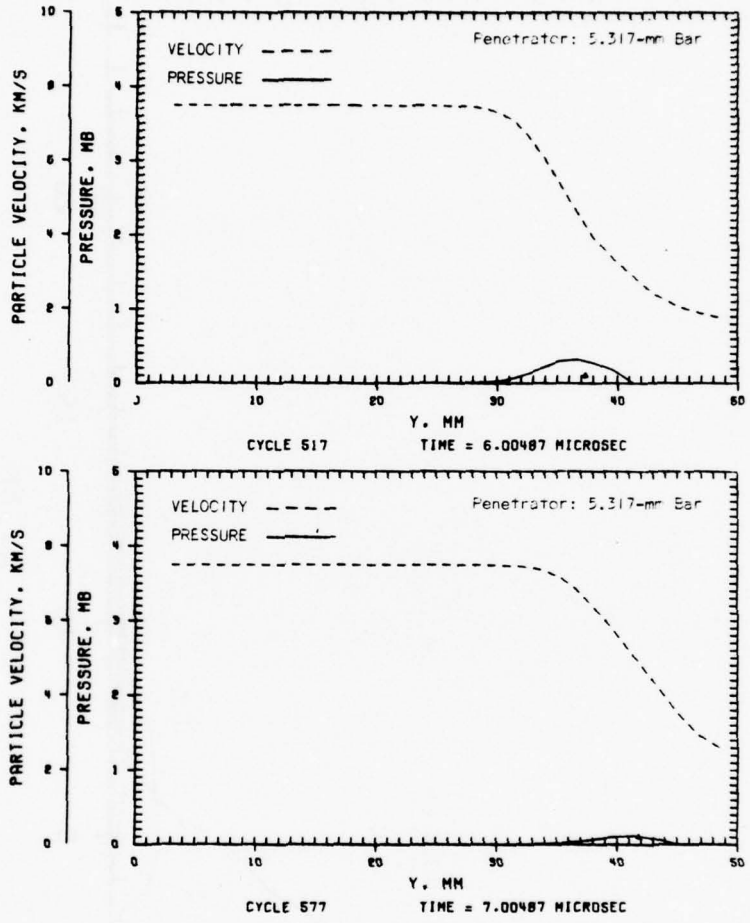

Figure 57. Pressure and Particle Velocity Profiles along the Y-Axis

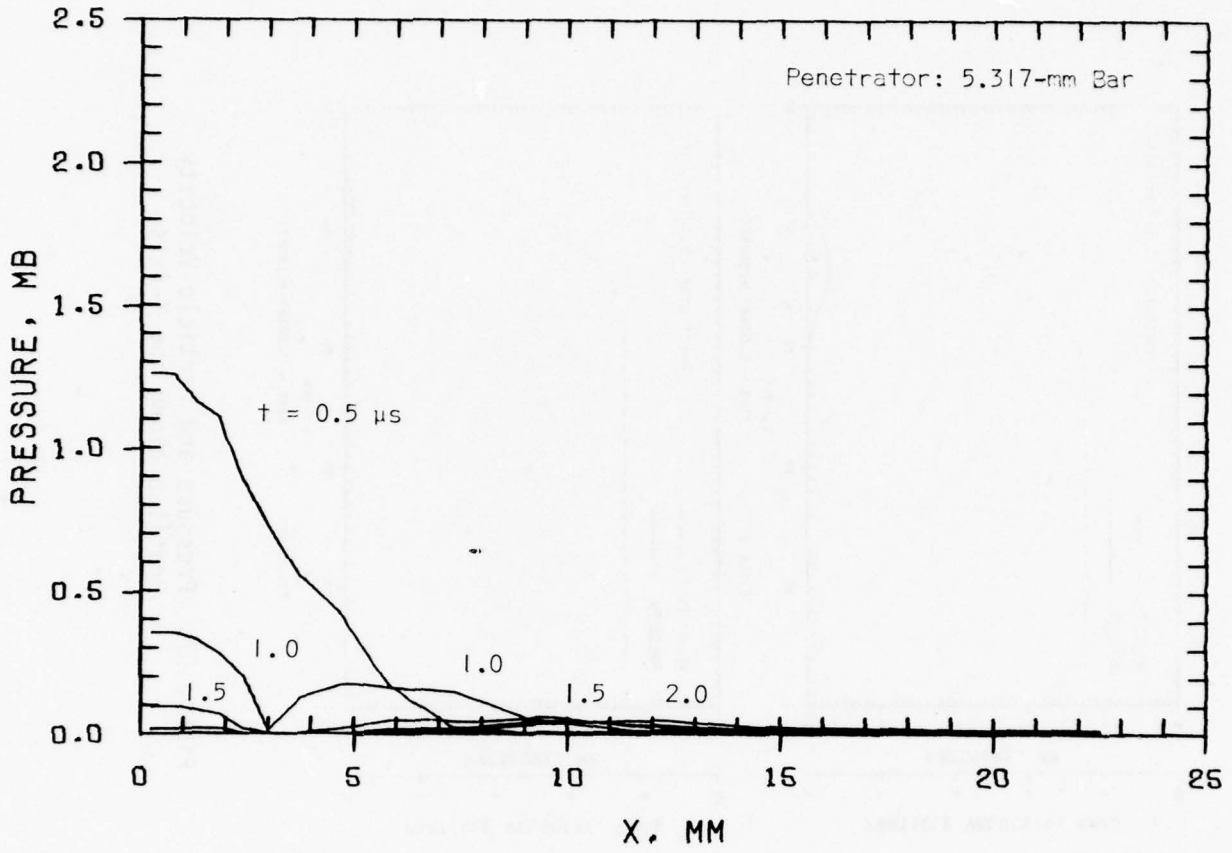

Figure 58. Pressure Profiles in the 15.25-mm Y-Plane and the Z-Coordinate Plane

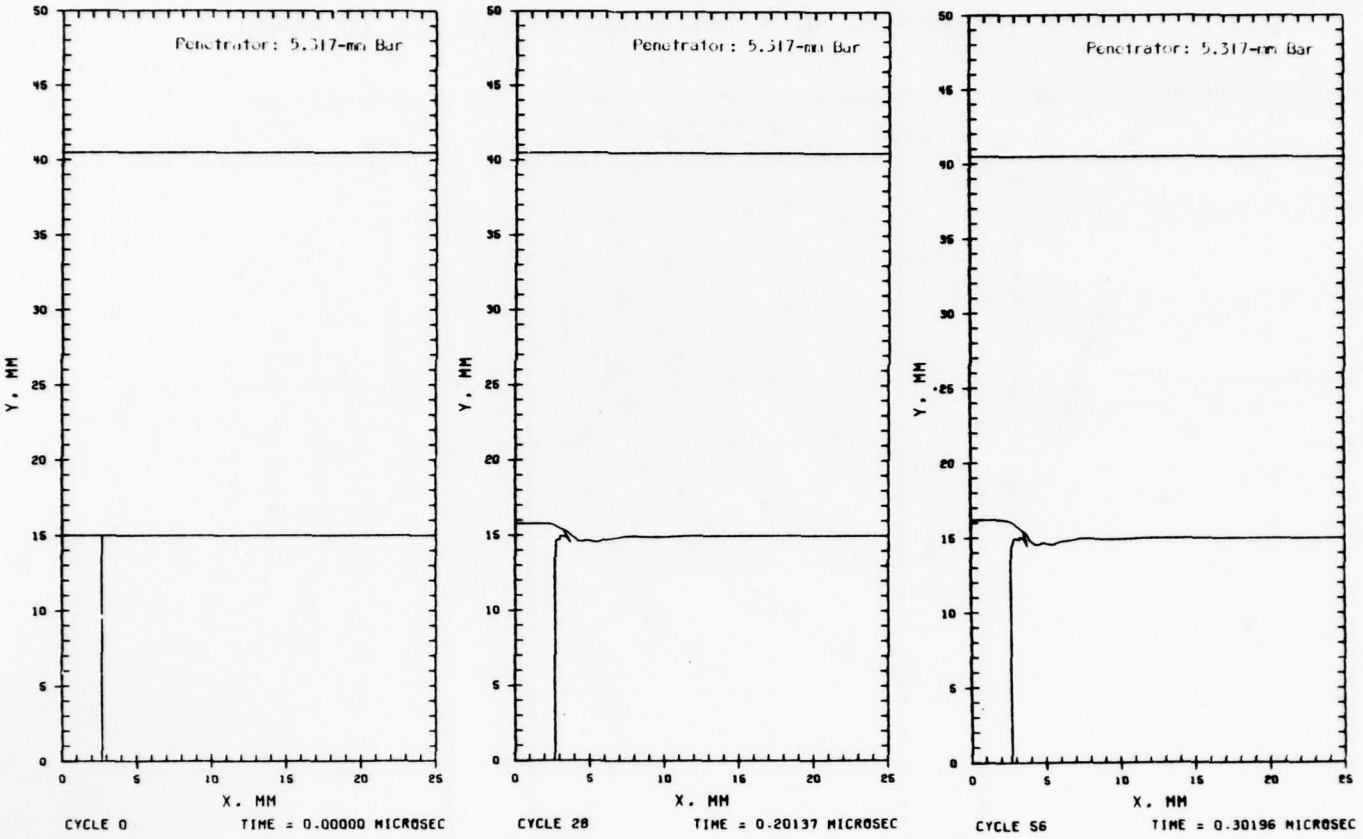

Figure 59. Bar-Target Deformation in the Z-Coordinate Plane

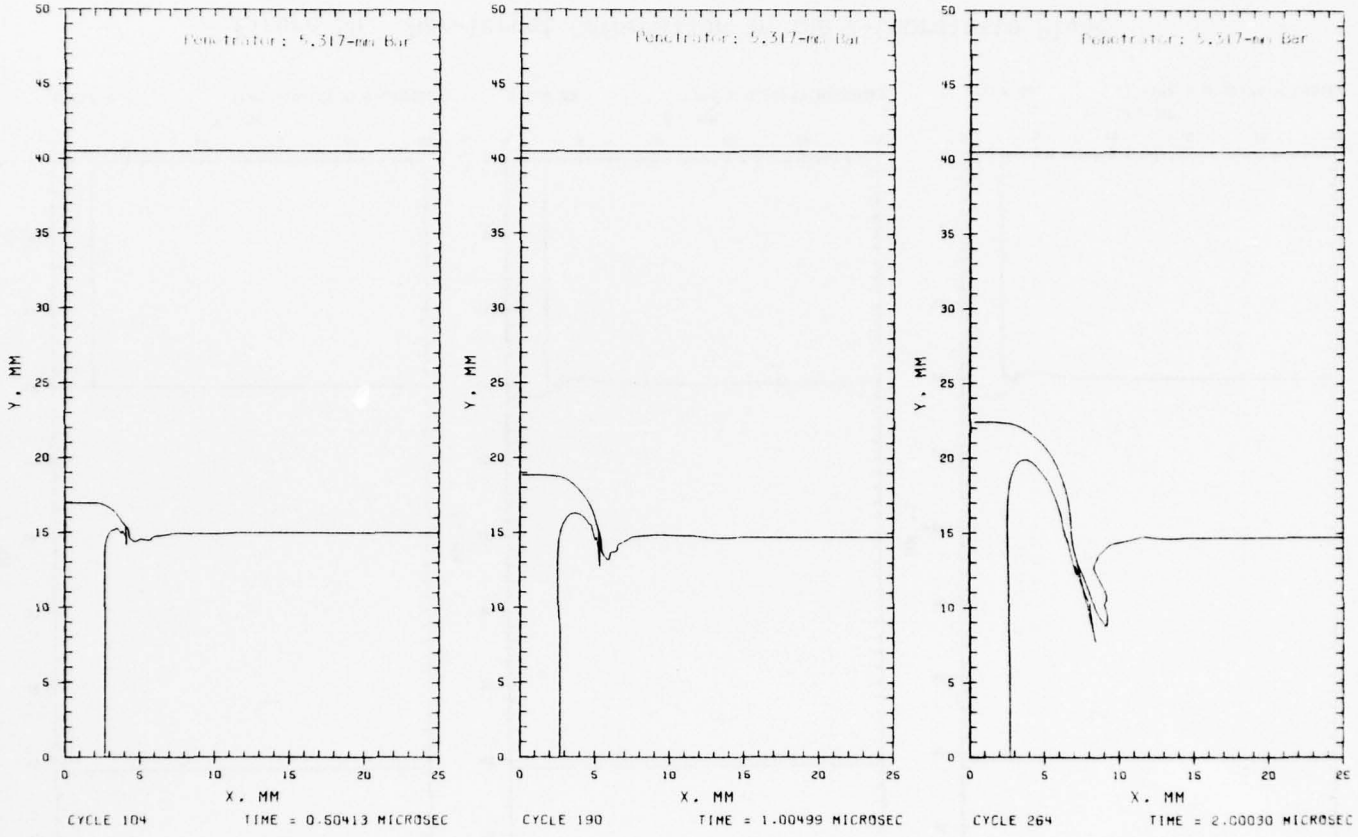

Figure 60. Bar-Target Deformation in the Z-Coordinate Plane

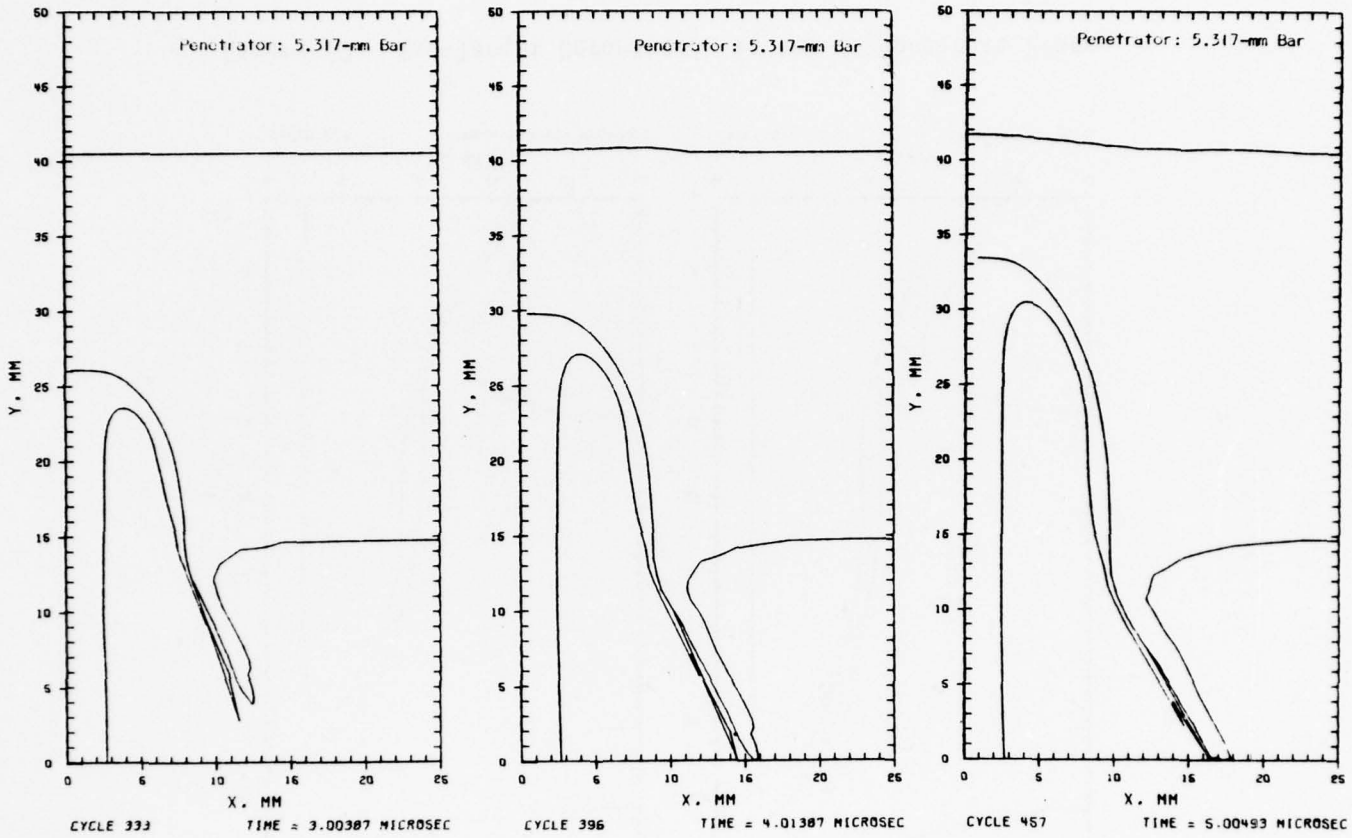

Figure 61. Bar-Target Deformation in the Z-Coordinate Plane

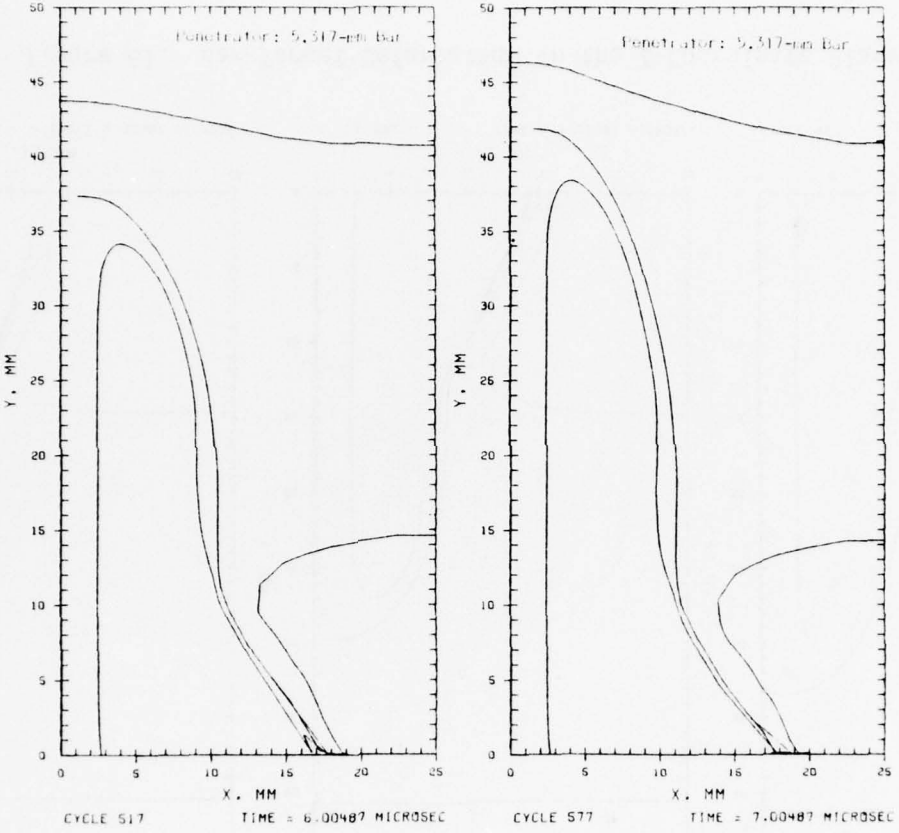

Figure 62. Bar-Target Deformation in the Z-Coordinate Plane

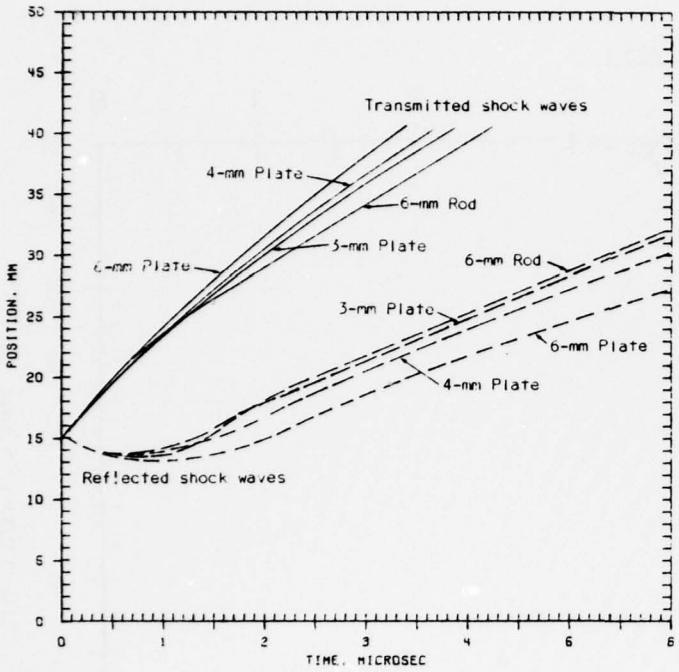

Cylindrical and Slab Geometries

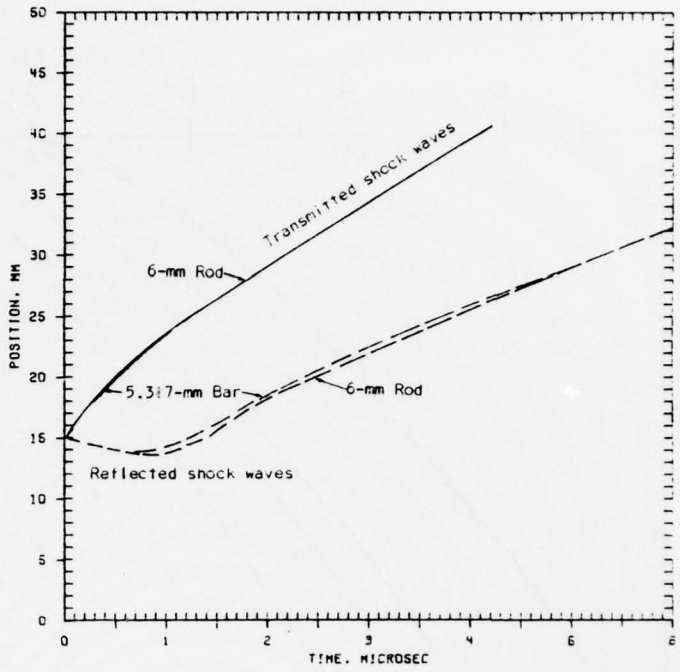

Cylindrical and Rectangular Geometries

Figure 63. Comparison of Transmitted and Reflected Shock-Wave Motion

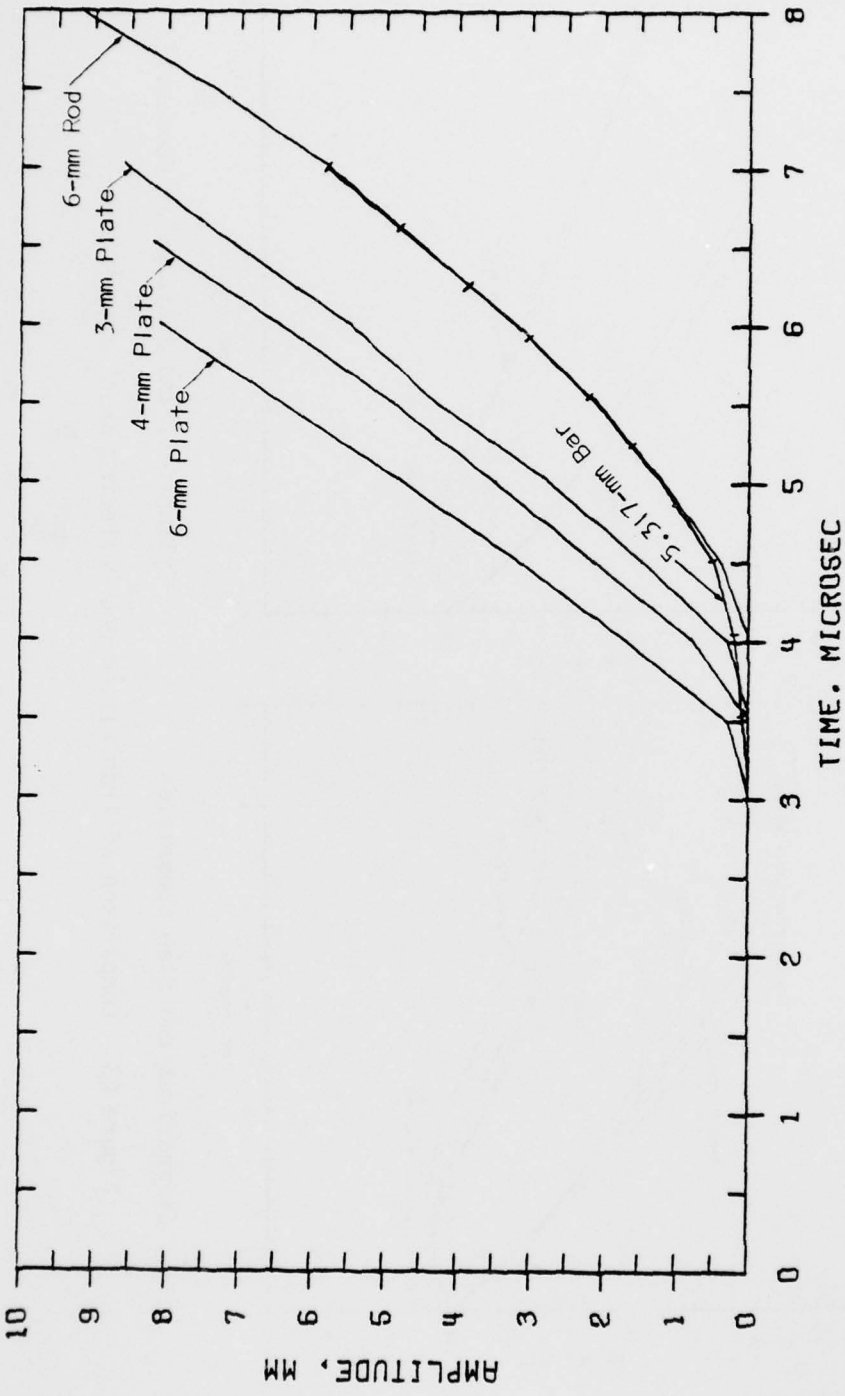

Figure 64. Comparison of the Motion of the Back of the Target

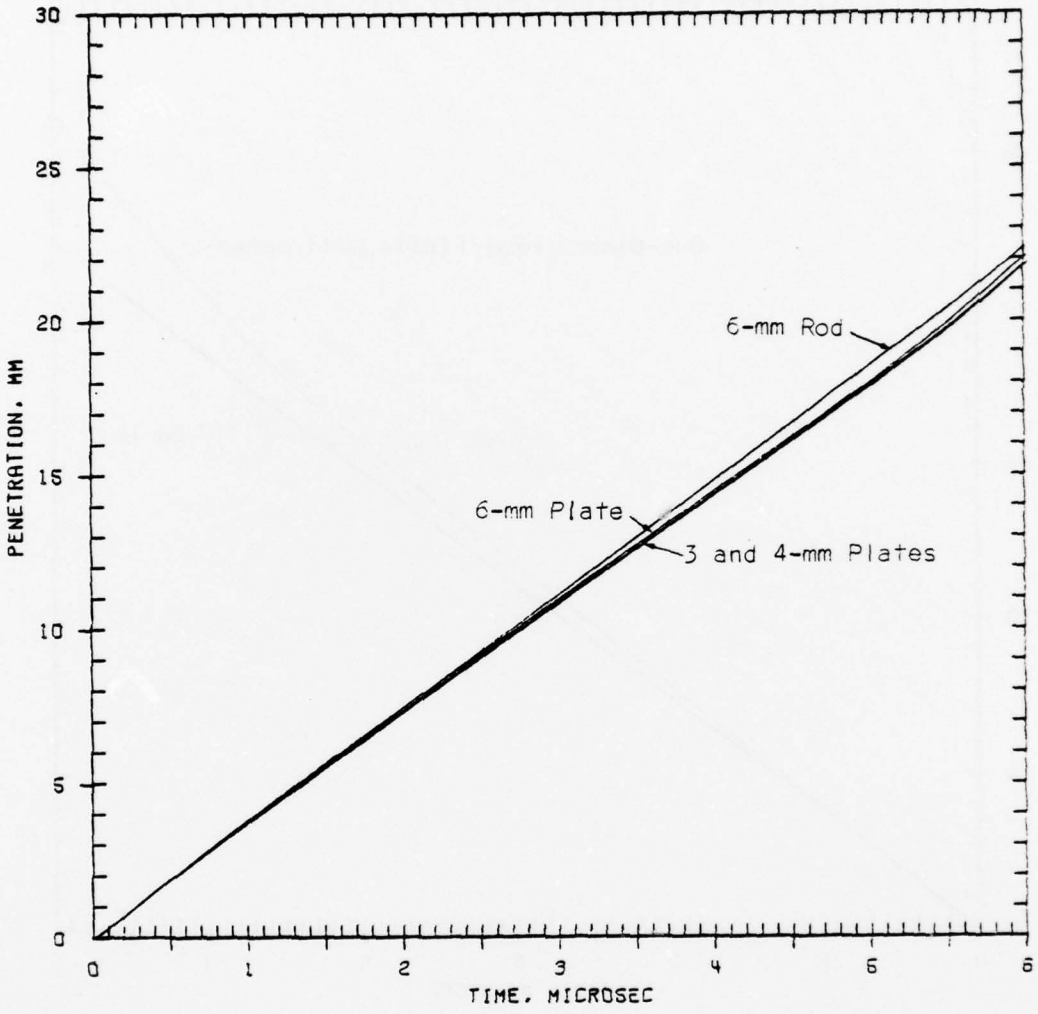

Figure 65. Penetration Histories for Cylindrical and Slab Geometries

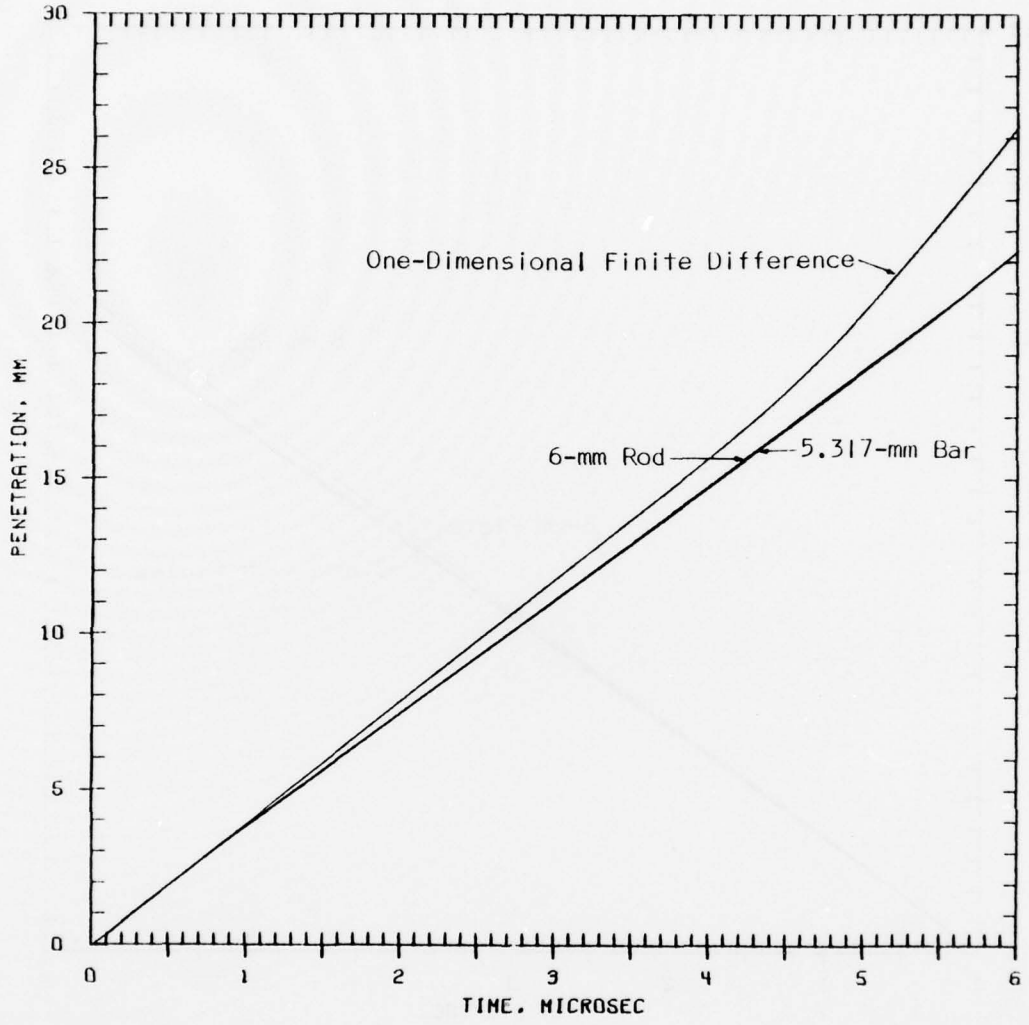

Figure 66. Penetration Histories for Cylindrical and Rectangular Geometries and the One-Dimensional Case

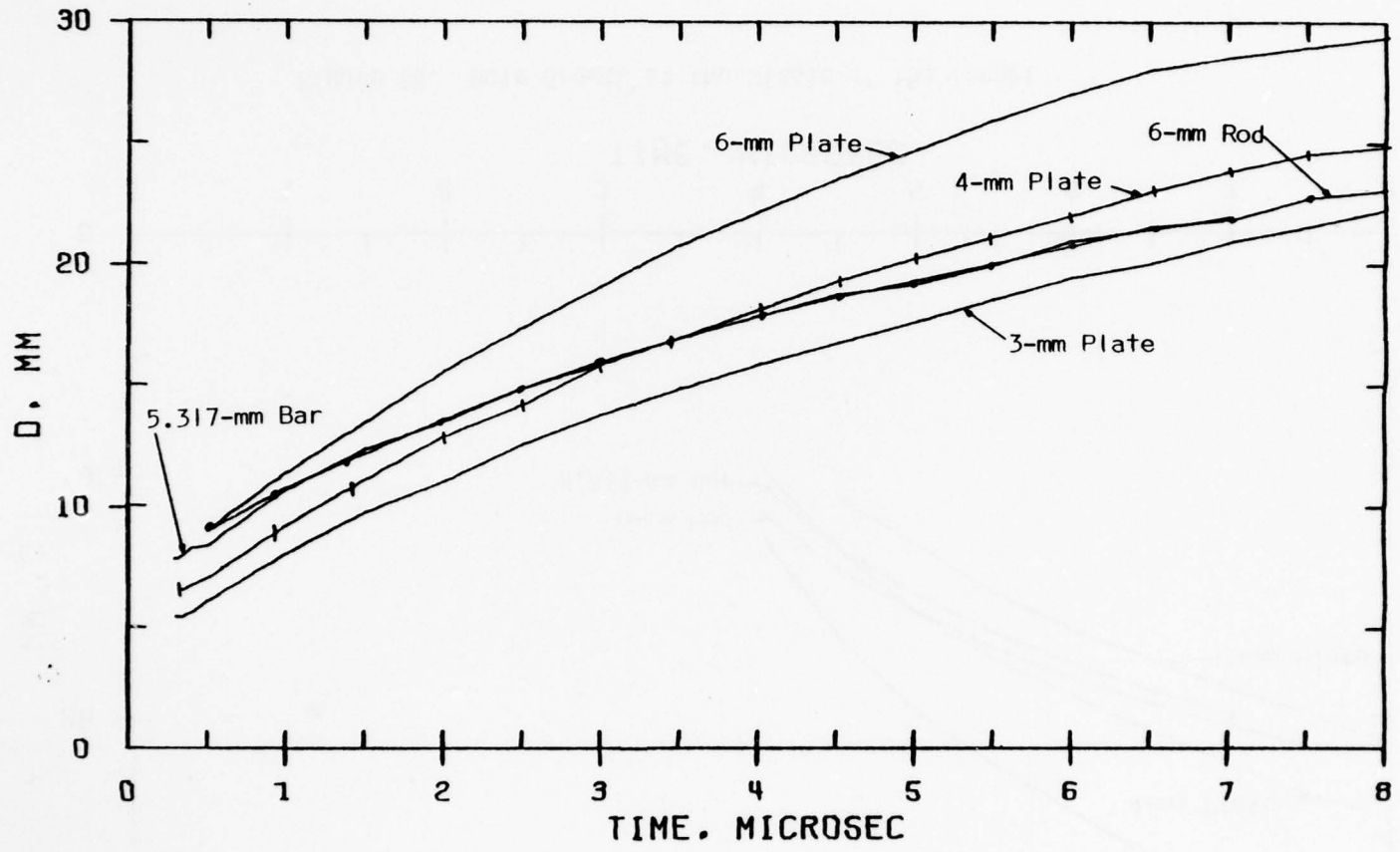

Figure 67. Hole Growth at the Front Surface of the Target

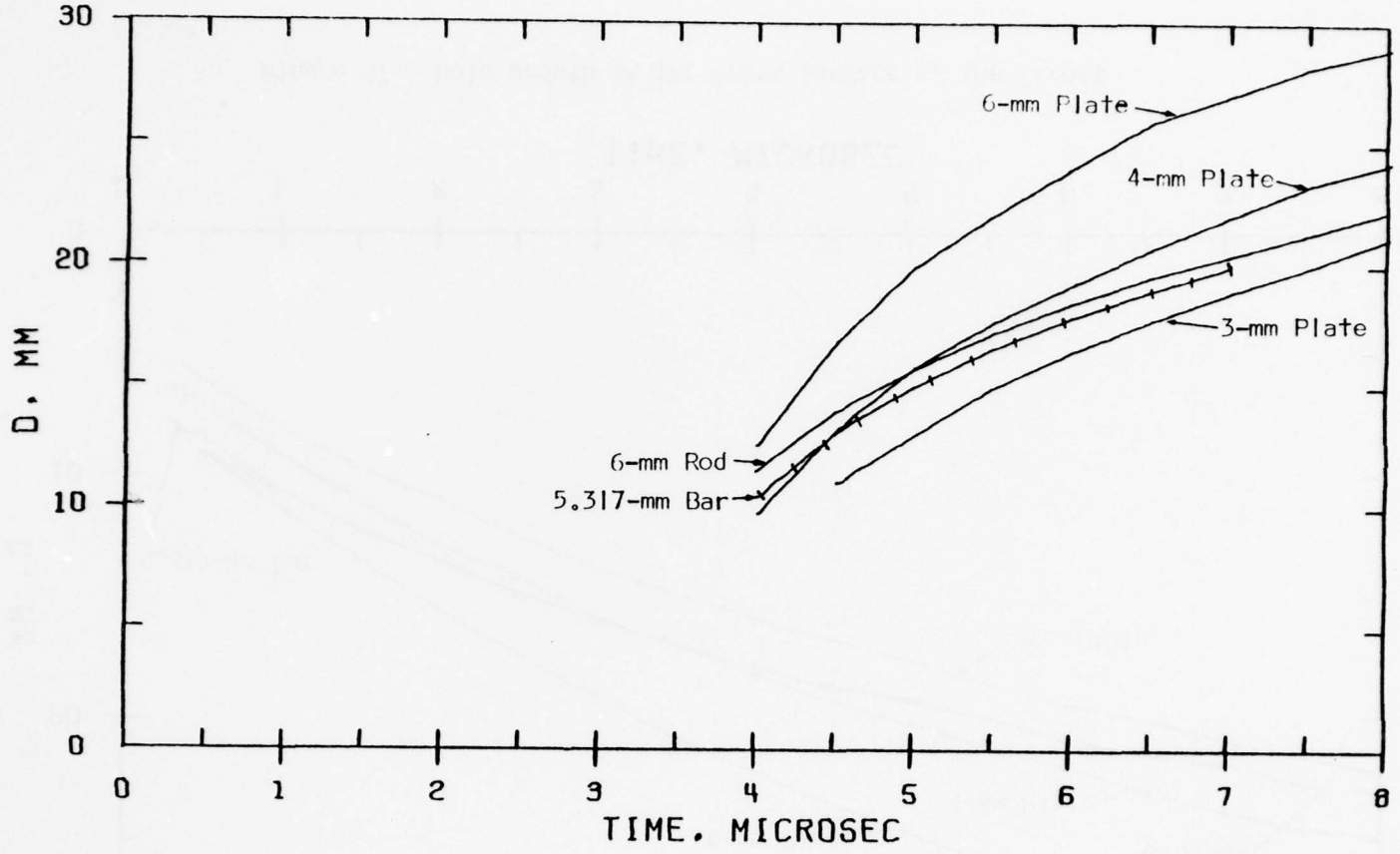

Figure 68. Hole Growth at the Middle of the Target

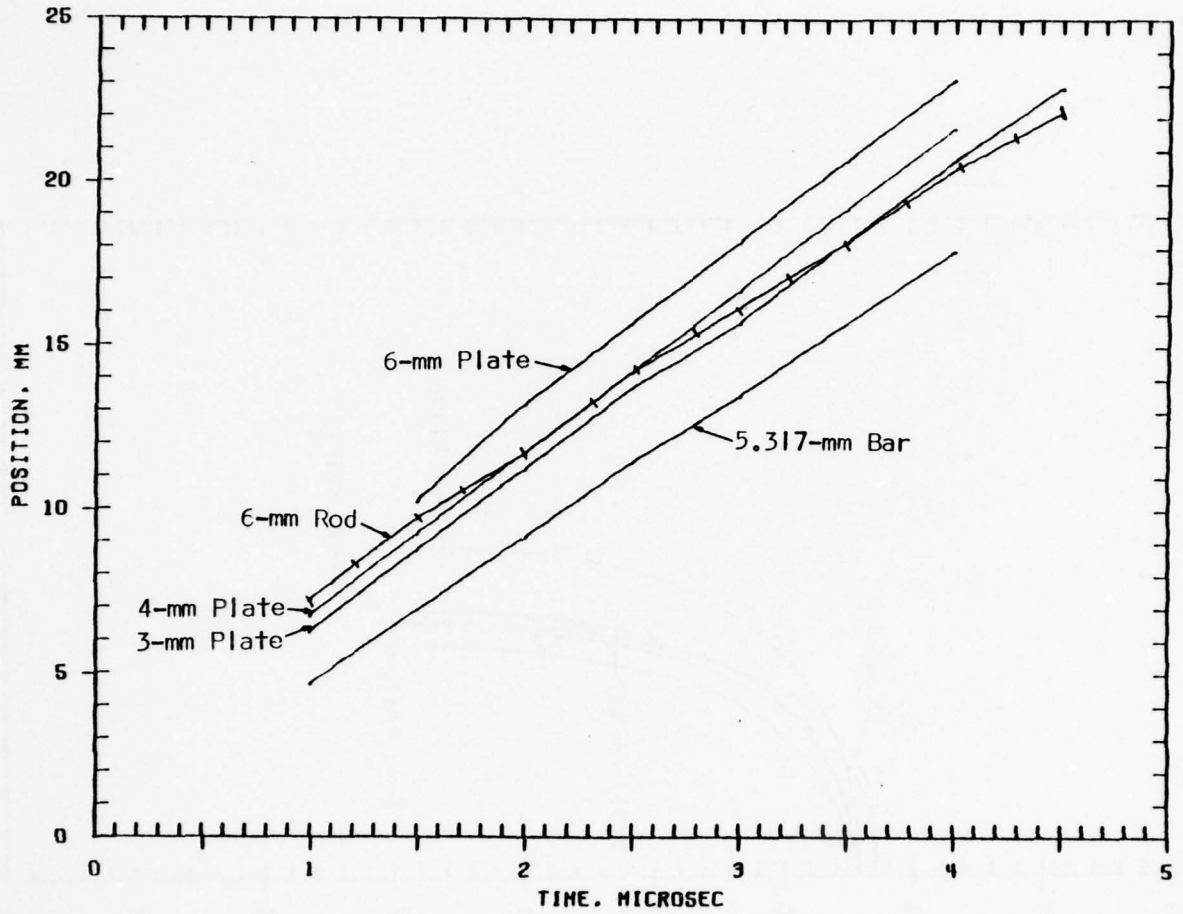

Figure 69. Comparison of the Transverse Pressure Motion

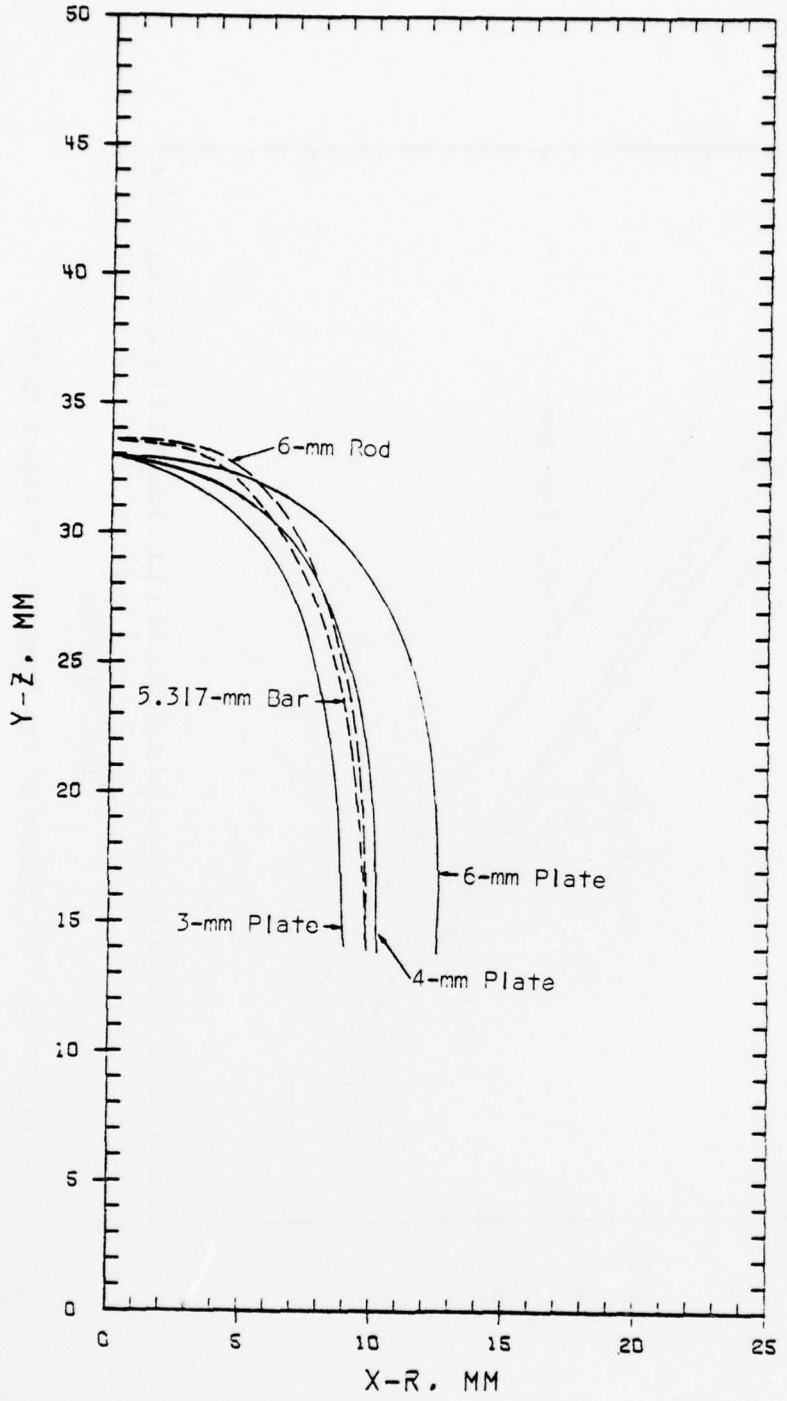

Figure 70. Comparison of Hole Profiles

DISTRIBUTION LIST

No. of Copies	Organization
12	Commander Defense Documentation Center ATTN: DDC-TCA Cameron Station Alexandria, VA 22314
1	Commander US Army Materiel Development and Readiness Command ATTN: DRCDMD-ST 5001 Eisenhower Avenue Alexandria, VA 22333
1	Commander US Army Aviation Research and Development Command ATTN: DRSAV-E 12th and Spruce Streets St. Louis, MO 63166
1	Director US Army Air Mobility Research and Development Laboratory Ames Research Center Moffett Field, CA 94035
1	Commander US Army Electronics Research and Development Command Technical Support Activity ATTN: DELSD-L Fort Monmouth, NJ 07703
1	Commander US Army Communications Rsch and Development Command ATTN: DRDCO-SGS Fort Monmouth, NJ 07703
1	Commander US Army Missile Research and Development Command ATTN: DRDMI-R Redstone Arsenal, AL 35809
1	Commander US Army Missile Materiel Readiness Command ATTN: DRSMI-AOM Redstone Arsenal, AL 35809
1	Commander US Army Tank Automotive Research & Development Cmd ATTN: DRDTA-UL Warren, MI 48090
3	Commander US Army Armament Research and Development Command ATTN: Mr. J. Pearson DRDAR-TSS (2 cys) Dover, NJ 07801
1	Commander US Army Armament Materiel Readiness Command ATTN: DRSAR-LEP-L, Tech Lib Rock Island, IL 61299
1	Commander US Army Materials and Mechanics Research Center ATTN: Tech Lib Watertown, MA 02172
1	Director US Army TRADOC Systems Analysis Activity ATTN: ATAA-SL, Tech Lib White Sands Missile Range NM 88002
1	Assistant Secretary of the Army (R&D) ATTN: Asst for Research Washington, DC 20310

DISTRIBUTION LIST

No. of Copies	Organization
2	Chief of Naval Research Department of the Navy ATTN: Code 427 Code 470 Washington, DC 20325
2	Commander Naval Air Systems Command ATTN: Code AIR-310 Code AIR-350 Washington, DC 20360
1	Commander Naval Ordnance Systems Command ATTN: Code ORD-0332 Washington, DC 20360
1	Commander Naval Surface Weapons Center ATTN: Tech Lib, DX-21 Dahlgren, VA 22448
1	Commander Naval Surface Weapons Center ATTN: Code 730, Lib Silver Spring, MD 20910
1	Commander Naval Weapons Center ATTN: Code 45, Tech Lib China Lake, CA 93555
1	Commander Naval Research Laboratory Washington, DC 20375
1	USAF (AFRDDA) Washington, DC 20330
1	AFSC (SDW) Andrews AFB Washington, DC 20331
1	US Air Force Academy ATTN: Code FJS-RL (NC) Tech Lib Colorado Springs, CO 80940
1	AFWL (SUL) Kirtland AFB, NM 87116
1	AFAL (AVW) Wright-Patterson AFB, OH 45433
1	AFLC (MMWMC) Wright-Patterson AFB, OH 45433
1	Director National Aeronautics and Space Administration Langley Research Center Langley Station Hampton, VA 23365
4	Director Lawrence Livermore Laboratory ATTN: Mr. M. Wilkins Dr. C. Godfrey Dr. G. Goudreau Dr. R. Werne P. O. Box 808 Livermore, CA 94550
1	Computer Code Consultants ATTN: Mr. W. Johnson 1680 Camino Redondo Los Alamos, NM 87544
1	Physics International Corp ATTN: Mr. L. Behrmann 2700 Merced Street San Leandro, CA 94577
1	Sandia Laboratories ATTN: Dr. L. Bertholf Albuquerque, NM 87115

DISTRIBUTION LIST

No. of Copies	Organization
1	Shock Hydrodynamics ATTN: Dr. L. Zernow 4710 Vineland Avenue North Hollywood, CA 91602
1	Systems, Science & Software ATTN: Dr. R. Sedgwick P. O. Box 1620 La Jolla, CA 92037
1	Drexel Institute of Technology Wave Propagation Rsch Center ATTN: Prof. P. Chou 32nd & Chestnut Streets Philadelphia, PA 19104
1	Southwest Research Institute Dept of Mechanical Sciences ATTN: Mr. A. Wenzel 8500 Culebra Road San Antonio, TX 78228
2	University of California Los Alamos Scientific Lab ATTN: Dr. J. M. Walsh Tech Lib P. O. Box 1663 Los Alamos, NM 87545
	Aberdeen Proving Ground
	Dir, USAMSAA Cdr, USATECOM ATTN: DRSTE-SG-H